INCORPORATION OF PROTEASE-SENSITIVE BIOMATERIAL DEGRADATION AND TENSILE STRAIN FOR APPLICATIONS IN LIGAMENT-BONE INTERFACE TISSUE ENGINEERING

A Dissertation
Presented to
The Academic Faculty

by

Peter J. Yang

In Partial Fulfillment
of the Requirements for the Degree
Doctor of Philosophy in the
Program of Bioengineering

Georgia Institute of Technology
December 2011

INCORPORATION OF PROTEASE-SENSITIVE BIOMATERIAL DEGRADATION AND TENSILE STRAIN FOR APPLICATIONS IN LIGAMENT-BONE INTERFACE TISSUE ENGINEERING

Approved by:

Dr. Johnna S. Temenoff, Advisor
School of Biomedical Engineering
Georgia Institute of Technology

Dr. Robert E. Guldberg
School of Mechanical Engineering
Georgia Institute of Technology

Dr. Thomas H. Barker
School of Biomedical Engineering
Georgia Institute of Technology

Dr. Marc E. Levenston
Department of Mechanical Engineering
Stanford University

Dr. Andrés J. García
School of Mechanical Engineering
Georgia Institute of Technology

Date Approved: October 18, 2011

Dedicated to Monica, my wife and best friend.

ACKNOWLEDGEMENTS

I want to start by thanking all the professors who gave me help and advice throughout my BME career. Thanks to my thesis committee: Dr. Tom Barker, Dr. Andrés García, Dr. Robert Guldberg, and Dr. Marc Levenston. Completing this thesis was an arduous task, and I struggled all along the way. At times I found it difficult to continue on this road. Talking with each of you about my work, I understood your continual support, and I walked away with renewed confidence and drive to keep running towards the finish line. At the same time, providing your perspectives on my work and giving me useful feedback have greatly challenged me and helped me to grow as a scientist, and I am thankful to have your high standards as something to aspire to as I continue my career. Dr. Brani Vidakovic in BME gave me significant help with statistical analysis, Dr. Alex Peister at Morehouse gave me help regarding our MSCs. I'd also like to acknowledge Dr. Jennifer West at Rice University, who helped me get started in biomaterials research working as an undergrad with Dr. Elizabeth Lipke and Dr. Lakeshia Taite. Their mentorship, and Jennifer's support, was instrumental in my decision to come to Atlanta for graduate study at Tech. Rice Bioengineering will always be a special place to me; remembering the days of HPN/senior design with Dr. Oden and classes with Dr. Saterbak are wonderful memories that I'll never forget.

I'd like to thank those in the department who helped me with my work. My brief personal interactions with people like Shannon Sullivan, Sally Gerrish, and Penelope Pollard helped make the department feel like a family. It was also my great joy to work with Shannon and Sally to jump start the BME Graduate Student Advisory Board. During

my time here, I appreciated the endlessly entertaining sequence of New Yantes. Steven Marzec, who I have frequently referred to as “a god among men,” should be commended for putting up with my n00bishness about computers. Thanks should also go to Aqua Asberry, who made our histology protocol flawless victory; Ashley, Casey and Noah for their help with flow cytometry; and Mark McJunkin for help with fabrication as well. Thanks also to all the BME and BIOE students in my year and later years who helped me to feel a sense of camaraderie and connection in my time at Tech.

My labmates made the journey worthwhile. Derek gave everything he had to get the lab started, and I am thankful for his friendship and sacrifice. He was a true Gryffindor and I hope our bond continues as he lives the life worth living. Kelly gave me a reason to smile every day, and I pray she continues to enjoy life but watch fewer musicals. Jeremy was, is and will be a better man than I ever could be, and always helped me laugh and to see the brighter side of things. It is truly inappropriate for me to have graduated before you. I’m thankful for your steadfast friendship and support through the years. T, I’m glad to have known you and am thankful for your friendship and your sense of humor, as well as your personal and technical insight. I’ve always appreciated your thoughtfulness and discernment. Thank you for being my foil and my friend. Song, thank you for your quiet and gentle spirit, for giving me perspective, and for laughing at my jokes even if they weren’t funny. There’s something I really like about you, but I can’t put my finger on what it is. And Jen, thanks for your simple joy and making me quietly happy to be around you, and helping me to know the lab is in capable hands. Thanks to Hieu for being a capable undergrad – continue to persevere and life can only get better and better. And finally, thanks also to Rahul, who showed me the meaning of safety.

Thanks to my friends and family outside of Tech. To Ed and Eric, thank you for these last few years. Your prayers and thoughts have helped me to grow and move forward and I am thankful for our regularly meeting together. To those from CCF and HCC, thanks for helping me to mature and grow in my faith, and for being my good friends throughout the years. My heart is still in Houston. Thanks to my parents, who have given me everything they've had. You raised me, taught me how to live, taught me what was most valuable in life, and I am forever grateful for you and everything you've done for me. I only hope I can begin to properly honor your commitment to me in the ways that I serve you and others in my life. Ultimately, my heart goes to Monica. You've always been there for me and helped me to see things as they truly are. You've always known how to take my jumble of thoughts and fuse them into something that makes sense. You know me better than I know myself. Thank you for being a light in my life, and for sacrificing and supporting me through this time. With you, every year I'm with you has been the best year I've ever had.

Finally, I should acknowledge Dr. Johnna Temenoff, my advisor. My five and a half years in Atlanta is wholly defined by my time as your student, and I will forever remain grateful for your criticism, guidance, encouragement and friendship over the years. I would not have been where I am today without your commitment to me as an advisor and friend; indeed, another thesis could be written on what your mentorship has meant to me and how I will struggle to repay a debt that can never be repaid. Thank you for everything.

TABLE OF CONTENTS

LIST OF TABLES

LIST OF FIGURES

LIST OF SYMBOLS AND ABBREVIATIONS

ACL	Anterior cruciate ligament
AcCl	Acryloyl chloride
bFGF	Basic fibroblast growth factor
BMP-2	Bone morphogenetic protein-2
ANOVA	Analysis of variance
Acrl-PEG-SVA	Acrylate-PEG-succinimidyl valerate
APS	Ammonium persulfate
CaH_2	Calcium hydride
Da	Daltons
DAB	Diaminobenzidine
DNA	Deoxyribonucleic acid
ddH_2O	Distilled, deionized water
ECM	Extracellular matrix
FBS	Fetal bovine serum
FuCl	Fumaryl chloride
GAPDH	Glyceraldehyde phosphate dehydrogenase
GPC	Gel permeation chromatography
GRGDS	Glycine-arginine-glycine-aspartate-serine
hMSCs	Human mesenchymal stem cells
IGF-1	insulin growth factor-1
kDa	Kilodaltons
MCL	Medial collateral ligament
MeCl	Methylene chloride

MMP	Matrix metalloproteinase
M_n	Number molecular weight
mRNA	Messenger ribonucleic acid
MSC	Mesenchymal stem cell/marrow stromal cell
MW	Molecular weight
MyoD	Myogenic differentiation protein
OCT	Optimal cutting temperature compound
OPF	Oligo(poly(ethylene glycol) fumarate
OPF 10K	OPF with a 10 kDa PEG chain
PBS	Phosphate buffered saline
PDGF	Platelet-derived growth factor
PEG	Poly(ethylene glycol)
PEG-DA	Poly(ethylene glycol)-diacrylate
PI	Polydispersity index
PLGA	Poly(lactic-co-glycolic acid)
PGA	Polyglycolic acid
PLLA	Poly-L-lactic acid
RGD	Arginine-glycine-aspartate
RT-PCR	Reverse transcriptase polymerase chain reaction
TEA	Triethylamine
TEMED	N,N,N',N'-tetramethylethylenediamine
TGF-β	Transforming growth factor-beta
TNF-α	Tumor necrosis factor-alpha
W_d	Weight of the hydrogel after vacuum-drying
W_w	Weight of the hydrogel after culture and before drying

SUMMARY

The interface between tendon/ligament and bone tissue is a complex transition of biochemical, cellular, and mechanical properties. Investigating computational and tissue engineering models that imitate aspects of this interface may supply critical design parameters for designing future tissue replacements to promote increased biochemical and mechanical integration between tendon/ligament and bone. Strategies for modeling this tissue have typically focused on the development of heterogeneous structures to create gradients or multiphasic materials that mimic aspects of the transition. However, further work is required to elucidate the role of specific mechanical and material stimuli in recapitulating features of the tendon/ligament-bone insertion. In particular, in constructs that exhibit variation in both mechanical and biochemical properties, the interplay of mechanical, material, and chemical signals can complicate understanding of the particular factors at work in interface formation. Thus, the overall goal of this dissertation was to provide insight into the role of mechanical strain and scaffold degradability on cell behavior within heterogeneous biomaterials.

Specifically, a method for determining cell vertical position within a degradable gel through a laminated interface was developed. A computational model was created to examine possible variation in local mechanical strain due to heterogeneity in mechanical properties and different interface geometries. Finally, the influence of biomaterial degradability on changes in encapsulated human mesenchymal stem cell (MSC) morphology under response to cyclic mechanical strain was explored. Together, these studies provide insight into mechanical and material design considerations when devising tissue engineering strategies to regenerate the tendon/ligament-bone interface.

CHAPTER 1

INTRODUCTION

1.1 Motivation

Ligaments and tendons restrict joint motion and provide load transfer between other components of the musculoskeletal system (1). Thousands of people are treated each year for injuries to tendon and ligament tissue (2). Upon acute injury due to physical activity or degenerative tendinopathy, replacement tissues are physically secured via mechanical interference (3). However, general agreement exists that reproduction of the biochemical and cellular heterogeneity of the natural interface between tendon/ligament and bone would improve tissue integration (4). Many tissue engineering approaches have been employed to investigate the development of this interface, using heterogeneous constructs to model the transition (4). In such constructs, the inherent complexity in the design may limit understanding of the particular contributions of individual design elements, such as cell type or scaffold geometry (5). Thus, some recent studies have focused on using just one type of cell, such as fibroblasts or marrow stromal cells/mesenchymal stem cells (MSCs), to create heterogeneous tissues (6-8). In particular, MSCs are employed due to their relative ease of harvest and their ability to differentiate toward a tendon/ligament fibroblast phenotype through the use of mechanical strain (9). However, applying mechanical strain to a construct with differences in geometry and mechanical properties may introduce subsequent variability in local strain environments. Furthermore, the use of biomaterial scaffolds that offer additional biofunctionality, including cell adhesion and enzyme-sensitive degradation, can facilitate additional cell behaviors such as cell migration (10). However, the interplay between biomaterial

degradation and mechanical strain on cell behavior are not well understood. Therefore, controlled experiments that elucidate the effects of various material and mechanical considerations in construct design can provide fundamental insight into the rational design of future approaches for engineering the interface between tendon/ligament and bone.

1.2 Research Objectives

In order to build a model system of the ligament bone-interface, multi-layered constructs composed of enzyme-sensitive hydrogels were fabricated. However, in order to understand the system's capabilities and limitations, it was first necessary to characterize the effect of enzyme degradability on encapsulated cell migration and response to strain. Therefore, the objective of the research presented in this dissertation was to improve understanding of the roles of tensile strain and scaffold degradability on MSC behavior after encapsulation in these hydrogels. Specifically, enzymatically-degradable biomaterials were used to facilitate determination of cell position within a multi-layer construct. A finite element model was developed to investigate the effects of stiffness mismatch and material geometry on local strain environments within a biomaterial. In addition, a model biomaterial with adjustable sensitivity to enzymatic degradation was utilized to explore the role of degradability in enabling changes in human MSC (hMSC) shape and its subsequent effects on hMSC response to cyclic tensile strain. The goal of these studies was to provide additional understanding of the role of mechanics and material degradability on the behavior of cells encapsulated in a homogeneous material for future applications in model systems featuring heterogeneous

materials. The **central hypothesis** was that culture of hMSCs in an enzymatically-sensitive biomaterial scaffold would allow significant changes in cell morphology, thus enabling cell migration in three dimensions as well as enhancing response to tensile loading. This hypothesis was explored through two specific hypotheses and research aims.

Hypothesis I: Culture of cells in a biomaterial environment rendered susceptible to enzymatic degradation will enable large-scale directed cell migration across a laminated interface.

Specific Aim I: Evaluate the effect of including a protease-sensitive peptide sequence into the polymer backbone of PEG-based hydrogels on changes in bovine MSC and HT-1080 fibrosarcoma cell migration through a laminated hydrogel at 7 days.

Cell migration has been previously implicated in the invasion and remodeling of damaged tissues and has been proposed as a useful tool for regenerating tissue interfaces. To explore migration in synthetic biomaterial models for tissue engineering, migration has been enabled by incorporating peptide sequences into the material backbone to facilitate cell adhesion and cell-directed degradation. Laminated synthetic hydrogels provide an opportunity to model the heterogeneity of interface tissues, but the nature and extent of cell migration across a laminate interface is unknown. Thus, a biomaterial and image analysis system was established to evaluate the effect of hydrogel degradability on possible cell migration in a multilayer hydrogel. Bovine MSCs and HT-1080 fibrosarcoma cells were encapsulated in hydrogels either sensitive or insensitive to protease degradation, and then laminated to a second gel section. Cell positions within each multilayer hydrogel were evaluated at 7 days. As a first pass at evaluating

chemotactically induced migration, HT-1080s were also encapsulated in either non-degradable or slow-degrading gels and laminated to a hydrogel layer originally polymerized in FBS. Cell positions were similarly evaluated at 7 days.

Hypothesis II: PEG-based biomaterials with increased susceptibility to enzyme degradation will enable increased cell spreading in encapsulated MSCs, enhancing the effect of a uniform distribution of cyclic tensile strain on MSC upregulation of gene expression and ECM deposition.

Hypothesis IIA: Applied cyclic tensile strain in a PEG-based hydrogel will result in uniform local strain fields across the hydrogel. In constructs with mechanical heterogeneity, local strain distribution can be modified through adjustments in interface geometry.

Specific Aim IIA: Develop a finite element model to characterize the effects of interface geometry and disparities in material stiffness on local strain distributions throughout a PEG-based hydrogel.

Tensile strain has previously been used, in our laboratory and others, to encourage differentiation of MSCs towards a tendon/ligament fibroblast phenotype when encapsulated in hydrogel materials. However, macroscopically applied strain may result in a distribution of local strains within a hydrogel depending on the point of applied load, material geometry, and variations in stiffness in individual portions of the hydrogel. A finite element model was developed to simulate the effects of 10% strain on local principal strain distributions within a representative hydrogel cultured in a tensile culture

bioreactor. Additionally, the effect of interface geometry and mismatches in modulus on local strain distributions were evaluated. Testing of OPF/PEG-DA hydrogels at different strain rates was performed as a first pass at validating assumptions made in creating the model.

Hypothesis IIB: PEG-based hydrogels with greater sensitivity to enzymatic degradation will encourage spreading as well as greater tendon/ligament fibroblast-related gene expression and matrix deposition in response to tensile culture strain by embedded human MSCs.

Specific Aim IIB: Characterize changes in encapsulated MSC morphology due to incorporation of differentially protease-sensitive peptides into the backbone of PEG hydrogels, as well as subsequent MSC response to cyclic tensile strain over 14 days.

Tensile strain has been used to differentiate MSCs towards a tendon/ligament fibroblast phenotype and may be useful in guiding the formation of the tendon/ligament portion within a tendon/ligament-bone interface. Interestingly, in 2D, cell shape has been implicated in directing MSC differentiation based on changes in actin contractility. Two peptide sequences with differences in sensitivity to protease degradation were incorporated in synthetic PEG hydrogels to investigate whether increased matrix degradability would encourage changes in MSC shape. It was hypothesized that differences in degradability would also be significant when encapsulated MSCs were exposed to cyclic tensile strain. Changes in MSC morphology in PEG-based hydrogels were compared between the incorporation of slow-cleaving and fast-cleaving protease-sensitive peptides into the PEG polymer backbone. Next, hMSCs were encapsulated in

slow- or fast-degrading PEG hydrogels and subjected to either static or cyclic strain (10%, 1 Hz, 3h on, 3h off) through 14 days. Cell circularity and angle were calculated to quantify changes in cell shape and alignment, respectively. Gene expression levels and ECM production between all four groups (slow- and fast-cleaving gels, dynamically strained and statically cultured) were measured. These were used to determine whether stretched MSCs were affected by increased sensitivity to biomaterial degradation.

1.3 Significance and Scientific Contributions

The studies in this dissertation provide critical insight into multiple aspects of modeling regeneration of the ligament-bone interface. The use of a synthetic biomaterial environment for these studies allowed adhesion sites and protease-sensitive degradation sites to be presented in a precise manner, permitting the explicit control of certain behaviors such as cell spreading. Developing techniques for characterizing 3D cell position in a laminated hydrogel enables monitoring of mass cell migration in the remodeling of degradable, multi-layer tissue engineering constructs. Finite element modeling provided specific information regarding the theoretical extent and distribution of differences in local strain within hydrogel materials used in experimental studies, as well as crucial insight into the distribution of strain in future designs of heterogeneous scaffolds with variations in geometry and stiffness. The coupling of gel degradation and changes in MSC morphology with cyclic tensile strain provided additional understanding regarding aspects of the biomaterial interface that are necessary for encouraging tendon/ligament differentiation. These results provide useful information on future parameters for the design of tissue engineering strategies for regenerating the interface

between tendon/ligament and bone.

The exploration of degradable synthetic biomaterials has applications that extend to other aspects of tendon/ligament tissue engineering and tissue engineering in general. From a technical perspective, in addition to enabling changes in cell morphology within synthetic scaffolds, employing enzymatically-degradable PEG-based hydrogels as cell carriers permits complete degradation and recovery of cells after encapsulation, enabling subsequent analysis or other use. Experiments studying cell migration can utilize differentially enzyme-sensitive biomaterials in complex configurations to examine how biomaterials and tissues are infiltrated and remodeled by cells over time. In a different paradigm for tissue repair, biomaterials can be used as cell carriers for imparting a variety of stimuli to cells, to 'prime' cells towards a desired phenotype prior to recovery and *in vivo* therapeutic use. As such, results from this thesis increase understanding of the effects of biomaterial degradation on cell behavior. These findings may have significant impact not just on design parameters for interface tissue engineering, but on new paradigms for strategies to repair damaged tissues.

CHAPTER 2

BACKGROUND AND LITERATURE REVIEW[1]

2.1 Tendon/Ligament and Its Insertion Into Bone

2.1.1 Tendon/Ligament Function, Structure and Composition

Tendons and ligaments are responsible for linking the musculoskeletal system; tendons transfer mechanical loads between muscles and bones, while ligaments bind bone to bone to restrict their motion (1). In the knee, ligaments play a particularly important role; being an inherently unstable joint, the knee relies on ligaments such as the anterior cruciate ligament (ACL) and the medial collateral ligament (MCL) to restrict tibiofemoral motion and maintain joint stability (1, 11). Tendons and ligaments function primarily in tension and exhibit similar cellular and biological composition (1, 12).

Tendon and ligament are approximately 60% water and 40% cells and matrix-related macromolecules (11, 13). The dominant cell type in tendon and ligament is the fibroblast; they are spindle-shaped and aligned longitudinally with the tissue (11). Biochemically, the main components of tendon and ligament tissue include collagens type I (90-95% of total collagen) and III (5-10%), with elastin (2%), glycoproteins and various proteoglycans (1-3%) composing the remaining dry weight (1, 11, 14). The aligned organization of collagen fibers gives tendon and ligament its characteristic hierarchical structure. Electron microscopy has shown that collagen fibers in tendon and ligament display a wavy crimp structure without load (1, 11). Collagen molecules assemble to form microfibrils (4 nm diameter), which further aggregate to form subfibrils (20 nm) and fibrils (50-500 nm). Collagen fibrils are organized along with fibroblasts to

[1] Portions of this chapter were adapted from Yang PJ, Temenoff JS. Engineering orthopedic tissue interfaces. Tissue Eng Part B Rev. 2009 Jun;15(2):127–141.

form fascicles. Finally, multiple fascicles form a whole tendon or ligament. (1, 11, 14). Mechanically, the crimp structure of collagen fibers in tendon and ligament permits small deformations without actual tissue tension and can be seen in the stress-strain curve of tendon/ligament tissue, which displays a toe region at low deformations (13). When under deformation, the alignment of individual collagen fibers gives tendons/ligament its extremely high tensile strength (1).

The most dominant proteoglycan is decorin, thought to facilitate tendon fibril deformation by ensuring consistent fibril formation (14), but other proteoglycans can be found in minute amounts, including biglycan, fibromodulin, lumican, aggrecan, and versican (1, 15). Glycoproteins in tendon and ligament include tenascin-C; tenascin-C has been speculated to be an anti-adhesive or "inhibitory for spreading" molecule that allows cells to modify adhesion contacts to avoid overspreading during tissue mechanical strain (16). Tenascin-C is found to a greater degree in tendon and ligament than in other orthopaedic tissues and is frequently used as a marker of tendon tissues (17).

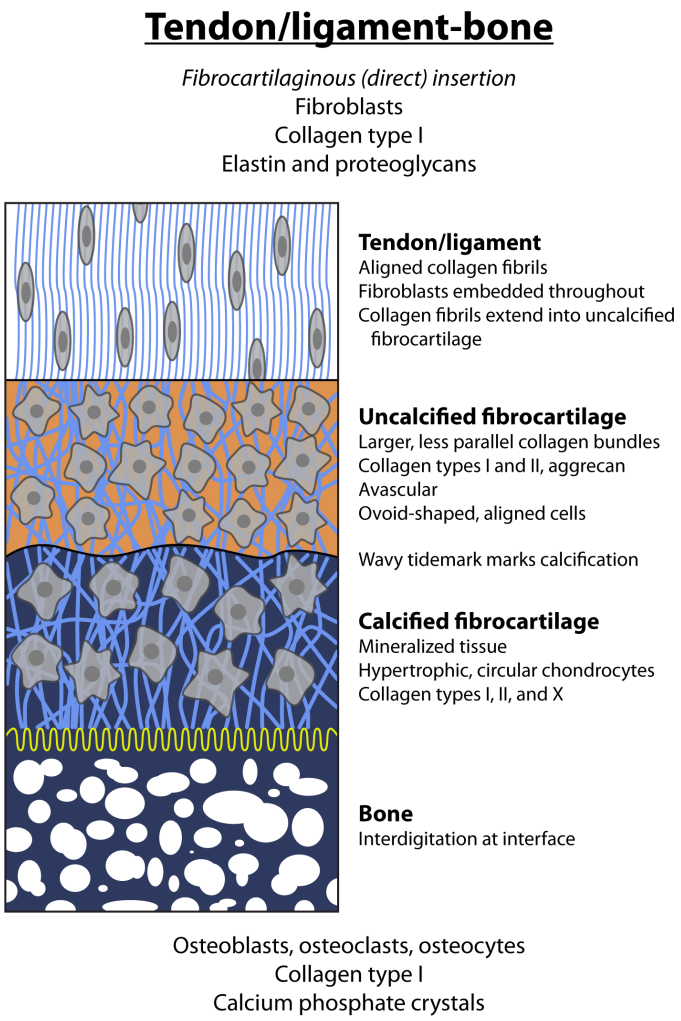

Figure 2.1. Diagram of direct insertion of tendon/ligament tissue into bone, depicting the four main areas of the transition (18).

2.1.2 Insertion of Tendon/Ligament Into Bone

At the interface, insertions of tendon or ligament into bone can be characterized as either direct or indirect (19). These types of insertions are also known as fibrous or fibrocartilaginous entheses (20). One example of a fibrous (indirect) insertion is the tibial insertion of the MCL (21). In fibrous insertions, a tendon or ligament attaches at acute angles to the bone through Sharpey's fibers, collagen fibers that extend directly through to the bone. On the other hand, fibrocartilaginous entheses, or direct insertions, are also

found; one example is the femoral insertion of the MCL (21). Generally, this type of tendon/ligament-bone insertion is characterized by a transition zone of four general types of tissue. The first zone is fibrous connective tissue, generally similar to normal tendon/ligament. This tissue contains aligned collagen fibrils with fibroblasts embedded throughout the collagen matrix. The next zone is uncalcified fibrocartilage, in which collagen fibril bundles are larger and less parallel than in the first region. Type II collagen and aggrecan are found in this matrix. This zone is relatively avascular, with ovoid-shaped, aligned cells. A flat tidemark has been found separating this zone and the next zone of calcified fibrocartilage (20). Calcified fibrocartilage contains hypertrophic, highly circular chondrocytes, with collagen X found only in this region (3). Between the calcified fibrocartilage and the fourth zone, bone, there is an interlocking region of tissue interdigitation, providing secure attachment between tissues (3, 20). Briefly, bone tissue contains osteoblasts, osteoclasts and osteocytes, with hydroxyapatite-mineralized collagen I fibers (1). Collagen type II is not present in bone (3).

The mechanics of the interface involve two materials of vastly different mechanical properties; tendons and ligaments are very strong in tension, while bone is optimized for compressive loading (1, 14). Without a gradual transition in mechanical properties, as in indirect/fibrous insertions, stress concentrations may form at regions where two materials of significantly different mechanical properties are joined (3). However, in fibrocartilaginous (direct) insertions, uncalcified and calcified fibrocartilage tissues at the interface are superior in transferring compressive load, and the insertion site shows an increase in Young's modulus across the transition (3, 22). Thus, fibrocartilaginous insertions provide the transitional zones of tissue to bridge the gap

between the mechanical properties of ligament and bone (23).

2.1.3 Tendinopathy, Pathology and Healing

It is estimated that at least 200,000 people in the United States receive treatment for injuries to tendon or ligament tissue each year (2). Injuries to tendon/ligament tissue either arise from acute trauma or chronic disorders, with some interplay between intrinsic (tissue alignment and defects in biomechanics) and extrinsic (physical exercise) factors (24). While acute injuries can result in a large rupture or tearing of the tendon or ligament, chronic injury results in small microtrauma that, over time, can result in an acute rupture or tear (25, 26). These injuries are usually the product of excessive loading, leading to inflammation over time, or variable microstresses within the tissue, which can induce individual fiber damage (27). Even without tearing, however, chronically excessive loading can still result in inflammation (25). Because tendon and ligament are poorly vascularized and largely acellular tissues (11, 17), the result of an injury is typically an active but poor healing response, with granulation tissue, collagen fiber degeneration, increased cell concentration, and generally widespread inflammation (14, 25, 27). Repeated injury over time leads to chronic pain and further modulates cell activity due to cytokine release (28).

Tendon and ligament repair in acute injuries can typically be described as three stages: the initial inflammatory response, increased cellularity and extracellular matrix deposition, followed by tissue remodeling (11, 25). In inflammation, serous fluid enters both damaged and surrounding tissues, and a hematoma is formed around the injury (26, 29). Inflammatory cells are recruited to the area and begin breaking down and

phagocytosing the clot and other debris (25, 26). Following the inflammatory response, fibroblasts are recruited to the area and begin producing a provisional matrix to bridge the injury (21). This matrix consists of a higher ratio of collagen III to collagen I, and typically contains higher levels of glycosaminoglycans, DNA, water and fibronectin (11, 21, 26). This provisional matrix is then remodeled by fibroblasts within the tissue, sometimes over years. This process is marked by both the conversion of collagen III to collagen I and a decrease in vascularity (19, 26, 27).

2.1.4 Developments in Clinical Intervention for Acute Injuries to Tendon/Ligament

The insertion of tendon/ligament tissue into bone is of particular concern in injuries; most tears occur not within the midsection of the tissue, but at its ends (11, 25). With regards to the anterior cruciate ligament (ACL) in the knee, its presence within an area of limited blood supply can affect the healing response (11). Most repairs of damaged ACL tissue involve the use of a ligament graft, in which the central third of the patellar ligament or the gracilis and semitendinosus (hamstring) tendons are used, with fairly similar outcomes regardless of the tissue used (18, 30-33). To perform the surgery, a bone tunnel is created and the tendon is affixed inside the tunnel with a metal fastener or degradable poly-L-lactic acid (PLLA) screw, the type of which can greatly affect graft success rates (34, 35). Depending on the patient, bone-ligament-bone transplants have also been performed (36).

Results within the bone tunnel have largely been positive, with Sharpey's fibers typically noted at the ligament-bone interface (37, 38). Clinical research strongly indicates, however, that restoration of a zonal insertion site, with regions of uncalcified

and calcified fibrocartilage, is the optimal outcome (39, 40). Multiple studies have emphasized the importance of good mechanical fixation; in early tests, reconstructed ACL grafts were found to fail at the fixation site upon mechanical testing (41, 42). This may be due to the lack of an insertion tissue region similar to what is found in normal tendon/ligament (43). With hamstring tendon grafts are used for ACL repair, poor bone tunnel integration has been shown to contribute to clinical outcomes that are less than ideal (44). Furthermore, when interference screws are used, the particular system used can contribute to graft laceration and early failure (45, 46). The limitations associated with graft fixation with poor bone integration can thus lead to increased graft failure and suboptimal clinical outcomes (3, 47).

Thus, recent studies have begun to explore methods for recapitulating the interface in an *in vivo* setting. One study used recombinant bone morphogenetic protein-2 (BMP-2) to induce ectopic bone formation in tendons, then transferred this structure to the surface of a bone to induce the formation of tendon-bone structures (48). A series of experiments from one laboratory have focused on various aspects of improving tendon-bone healing; recent strategies include, for example, through blocking of TNF-α (49), a combination of calcium phosphate scaffolds and TGF-β3 to guide fibrocartilage formation (50), short-duration cyclic loading (51), and the overexpression of matrix metalloproteinases (MMPs) in stem cells to improve fibrocartilage formation and biomechanical strength (52). Similar use of demineralized bone matrix between tendon and bone facilitated increased amounts of fibrocartilage and mineralized fibrocartilage in a sheep model (53). The use of a synthetic sheet of polyglycolic acid (PGA) has also been tested in regenerating the insertion; however, mechanical properties were limited

compared to normal tendon (54).

2.2 Tissue Engineering Tendon, Ligament and Its Interfaces

2.2.1 Review of Current Work

Engineering of tendon and ligament tissue, as well as the tendon/ligament-bone interface, requires strategies that ensure mechanical stability. Because the interface is crucial to proper repair, design constraints must also be applied based on the overall approach to insertion point regeneration; indeed, current work in interface engineering has focused on assisting graft anchorage (3). Although autografts (replacement tissue taken from the patient) and allografts (replacement tissue taken from a human cadaver source) are frequently used, the possibility of limited availability and donor site morbidity due to an immunogenic response are significant disadvantages (29, 55). Although many grafts have been developed using synthetic, non-degradable materials, they are not recommended as primary ACL replacements; in fact, many implanted synthetics end in failure due to fragmentation, fatigue and wear debris (29, 56).

The goal of tissue engineering tendon and ligament tissue is to use a combination of cells, scaffolds and bioactive factors to recreate a replacement tissue. Silk, collagen and the poly-L-lactide family of synthetic polymers are the most widely explored scaffolds, while mesenchymal stem cells and tendon/ligament fibroblasts are typically chosen as cell sources (17, 29). It has been proposed that MSCs may be an optimal cell source due to their increased proliferation rates and increased collagen deposition (57). After the choice of a proper scaffold and cell source, additional growth factors can be added to either MSC or fibroblast-populated scaffolds to induce further ECM deposition,

such as TGF-ß, insulin growth factor-1 (IGF-1), platelet derived growth factor (PDGF) and bFGF (58).

Because tendon/ligament tissue is primarily composed of collagen type I, collagen gels have been widely explored as scaffolds for engineering ligament tissue (17, 59). Although many studies report success with cell infiltration, tissue ingrowth and enhanced mechanical strength, most attempts do not generate matrices with mechanical properties similar to native tendon/ligament tissue (17, 60-65). Some studies, however, have produced scaffolds with mechanical properties similar to ligament. One experiment reported elastic moduli similar to native ligament tissue after 20 days in culture, with the presence of cells increasing construct peak stress (66).

Thus, due to the overall issues with collagen gel mechanical strength, many researchers use fibers or hydrophobic scaffolds. One natural material that has been widely explored is silk; silk fibers can be woven into a rope-like structure and have been tailored to match the stiffness of normal tendon/ligament tissue without reduction of ultimate tensile strength (17, 67, 68). After seeding on these fibers, MSCs demonstrated proliferation and ECM secretion over 14 days in culture (68). Scaffolds using synthetic polymers, typically PLLA and PGA, have also been utilized in tendon/ligament tissue engineering (29, 69-74). Like silk, several studies have woven PLLA fibers into 3D braids (29, 70, 72, 74). The 3D braiding technique, along with the use of PLLA allows for close control of mechanical properties, pore sizes, degradation properties, and overall geometry; a single braid can contain both a porous intraarticular zone as well as less porous bony attachment zones to assist in the formation of an interface (72).

Based on these scaffolds, one group has established multiphase matrices to

engineer the tendon/ligament-bone insertion point using scaffolds based on poly(lactic-co-glycolic acid) (PLGA) and bioactive glass (5, 75-77). In these studies, three distinct scaffolding phases were formed – one for ligament, one for bone, and a fibrocartilage interface. A study with bovine fibroblasts and osteoblasts seeded on either side of the middle phase demonstrated cells migrating into the middle layer (78). A subsequent subcutaneous implantation study in athymic rats using a triculture of bovine fibroblasts, chondrocytes and osteoblasts revealed the development of a fibrocartilaginous layer, with collagen X observed between the fibroblast and chondrocyte layer; mineralization was confined to the osteoblast layer (5).

Other experiments have also used innovative transfection strategies to create scaffolds with heterogeneous properties, with areas representing tendon/ligament and separate areas representing bone tissues. In one example, poly(L-lysine) was used in to spatially immobilize a Runx2 retrovirus onto a collagen scaffold. With Runx2 inducing osteogenesis in primary rat dermal fibroblasts, the scaffold developed a similar gradient of transcription factor expression and matrix deposition consistent with osteoblastic differentiation (6). Another approach used lentiviral and adenoviral transfection to express Smad8ca and bone morphogenetic protein-2 (BMP-2) in murine and human stem cells. Although the scaffold used was not pre-designed to create heterogeneous tissues, interface regions were spontaneously generated following *in vivo* implantation in mice (79).

Finally, a number of other approaches have been employed towards forming tissue constructs that recapitulate multiple interfaces between ligament and bone, forming a single bone-ligament-bone construct. One approach used PEG hydrogels with

incorporated hydroxyapatite particles as anchors in a bone-ligament-bone construct; hydroxyapatite was shown to improve the attachment of a fibrin-based scaffold (80). A follow-up study used a calcium phosphate-based brushite cement as anchors for a fibrin scaffold seeded with embryonic chick tendon fibroblasts. Brushite showed marked improvement in anchoring the fibrin gel, and some evidence of a tidemark at the interface was shown (81). Finally, a recent scaffoldless approach has been used in a number of studies to engineer a bone-ligament-bone-like construct. In this strategy, bone marrow stromal cell (BMSC) monolayers spontaneously rolled up on laminin-coated surfaces. After culturing with osteogenic differentiation medium, "bone constructs" were pinned and cultured on a second monolayer of BMSCs cultured with ligament differentiation medium, that is, growth medium plus TGF-β (7). After spontaneous formation of bone-ligament-bone-like constructs, these were used as replacement medial collateral ligaments (MCLs) in a rat model and allowed full recovery of knee function at 4 weeks. A recent followup study used similar constructs as ACL replacements in a sheep model, and found a functional enthesis, and increased mechanical properties reminiscent of native tissue after six months *in vivo* (8).

These studies illustrate the potential of using various tissue engineering principles to create homogeneous and heterogeneous constructs that recapitulate various aspects of native tendon and ligament tissue, as well as their complex and zonally organized interfaces with bone tissue.

2.2.2 Hydrogels in Orthopaedic Tissue Engineering

Hydrogels have been used as model and applied scaffolds for orthopaedic tissue

engineering in general (82-88); as such, hydrogels have been increasingly used for tendon and ligament tissue engineering applications (59, 65, 89). By crosslinking polymer chains, scaffolds can then be formed and swelled in aqueous solution to form highly hydrated hydrogel network structures (90, 91). Cells can be homogenously encapsulated within hydrogels, allowing hydrogels to act as a cell carrier (92). Hydrogels have been formed from both natural and synthetic materials. Natural materials offer increased biocompatibility and bioactivity for encapsulated cells; however, the inherent complexity of a natural scaffold, along with such concerns as batch-to-batch variability and limitations on chemical modification are significant drawbacks (93). Synthetic materials can be precisely and uniformly engineered to exhibit specific chemical and mechanical properties; however, any bioactive functionality must be expressly included (94). However, this affords a particular advantage: by engineering bioactive moieties in a tailored fashion, one can study specific cell behaviors in a discrete and controlled approach.

One such synthetic polymer that has been widely studied in tissue engineering is poly[ethylene glycol], or PEG; examples of PEG and its derivatives in orthopaedic tissue engineering include osteochondral interface tissue engineering (87), cartilage tissue engineering (95-97), and bone tissue engineering (98-100). PEG is widely studied due to its non-fouling properties (101), which enables PEG to be a "blank slate" upon which additional bioactive functionality can be specifically included in the hydrogel formulation. Furthermore, PEG can be modified with hydrolytically degradable fumarate groups to produce such polymers as oligo[poly(ethylene glycol)] fumarate (OPF) (102). OPF is cytocompatible (102, 103) and has been used extensively for bone, cartilage and tendon

tissue engineering (89, 104-108). To crosslink and form PEG-based hydrogels, PEG is usually chemically modified to include acrylate groups. The resulting PEG-diacrylate (PEG-DA) polymerizes with itself as well as OPF via free radical polymerization; polymerization occurs through a chain-growth mechanism that involves chain transfer of the radical to a free double bond on either the acrylate or fumarate groups (109). Radical initiators include the thermally responsive tandem ammonium persulfate (APS) and tetramethylethylenediamine (TEMED), as well as the photosensitive Irgacure 2959 (105, 110-112).

2.3 Considerations for Hydrogel-Based Tissue Engineering Models of Ligament

In the work presented in this dissertation, the use of synthetic hydrogels in a tensile culture bioreactor facilitated the detailed study of certain cell behaviors found in natural tissues. In this system, bioactive functionalities were presented in the microenvironment of a cell in a highly controlled manner to elucidate the role of each functionality – enzyme-directed degradation and mechanical strain – in certain cell behaviors which may be biologically relevant for regenerating the interface, including cell migration, changes in cell morphology, and gene expression/ECM deposition in response to the application of a specific tensile strain regimen. Aspects of the material and mechanical considerations in this model system are reviewed in the following sections.

2.3.1 Biomaterial Modification

2.3.1.1 Enabling Adhesion

In this work, PEG hydrogels were modified with additional bioactive moieties to elicit and facilitate several desired cell behaviors. One widely used bioactive peptide sequence that was included was the adhesion peptide RGD. RGD has been extensively characterized as an enabler of cell adhesion to formerly non-adhesive surfaces (113), and its dose-dependent effects have been investigated in a variety of orthopaedic tissue engineering studies (114-118). RGD has been implicated in ensuring encapsulated stem cell survival by preventing anoikis, or cell apoptosis due to lack of adhesion to its ECM (113, 119, 120). RGD enables cell adhesion through the protein family of integrins; integrins are transmembrane, heterodimeric receptors that bind a variety of extracellular matrix proteins (113). As one may surmise, a wide variety of extracellular matrix molecules display RGD sites, and RGD binds a wide variety of integrins, including the popularly studied $\alpha_v\beta_3$ and $\alpha_5\beta_1$ integrins, in a dose-dependent manner (113). However, with regards to the $\alpha_5\beta_1$ integrin, cytoskeletal force switches the integrin state to control binding of the PHSRN synergy site on fibronectin, providing increased mechanical strength to the bond (121, 122). Importantly, integrin expression in cells is dependent on many extracellular factors, including whether cells are cultured on 2D surfaces or in 3D matrices and whether the α5β1 synergy site is available for binding (123, 124). Following integrin activation and initial cell binding via integrin binding to extracellular ligands, focal complexes – mostly consisting of $\alpha_v\beta_3$ integrins – can cluster to form focal adhesions (125). Two groups of proteins, talins and kindlins, bind to β integrins and in turn connect them with the actin cytoskeleton (126). Thus, RGD can be included in PEG hydrogel systems to facilitate cytoskeletal involvement with its biomaterial environment via adhesive peptides. Linking of cells to its extracellular matrix also facilitates

mechanotransduction, or the sensing of mechanical aspects of the ECM (more below).

2.3.1.2 Enabling Cell-Mediated Degradation

Another bioactive functionality that has been studied in recent years has served to increase the degradability of hydrogels by including enzyme-sensitive peptide sequences in the backbone of a synthetic polymer. This functionality differs from previous efforts in enabling ester hydrolysis in previously non-degradable synthetic polymers, e.g. PEG and OPF (99, 102). Typically, natural ECM tissue is typically degraded via cell-secreted proteases, including matrix metalloproteinases (MMPs), which enable cell behaviors such as spreading within a 3D environment, migration and tissue invasion (10). Including enzyme-sensitive sequences enables cells to easily replace an implanted biomaterial with new tissue; indeed, a lack of degradability has been implicated in preventing full healing of tissue defects, due to the inability of cells to properly infiltrate the biomaterial (127-129). MMPs are a family of zinc-dependent metalloproteinases that cleave a variety of extracellular matrix molecules; all MMPs share common motifs in their active sites and inactivating propeptides (130). There are several subclasses of MMPs, of which a few are mentioned here: the collagenases, including MMP-1, MMP-8 and MMP-13, which cleave collagen types I, II and III; gelatinases, including MMP-2 and MMP-9, which cleave collagen types I-V and XI as well as laminin and aggrecan core protein; and membrane-bound MMPs (MT-MMPs) which can activate MMP-2 and degrade collagen types I, II and III (131, 132).

Significant effort has been given to finding peptide sequences that allow for facile recapitulation of cell-mediated degradation and downstream behaviors in a synthetic

environment. One of the earliest efforts used a collagenase-sensitive peptide sequence, LGPA, taken from the α1(I) chain of collagen I, and incorporated it into a PEG hydrogel to enable degradation (133, 134). Importantly, PEG hydrogels formed with this sequence could be completely degraded via addition of exogenous bacterial collagenase (135). Another more frequently used peptide, GPQGIWGQ, was developed from a more thorough search of candidate collagenase-sensitive peptide sequences (136), and has been widely used to study cell-mediated migration, tissue remodeling, and applications for bone or cardiovascular tissue engineering (98, 137, 138). More recently, a candidate peptide sequence, VPMSMRGG, was developed from a randomized dodecapeptide library with high cleavage sensitivity to MMP-1, MMP-2 and MMP-9 (139, 140). Each successive investigation has yielded peptides that are far more sensitive than original sequences, and offer increased degradation and desired cell responses in a smaller time frame (140). Other peptides have been developed for sensitivity to other enzymes such as plasmin (141). The use of cleavable peptides that are differentially sensitive to the same family of proteases can create contrasts in cell behavior based on the degradability of a particular sequence.

2.3.1.3 Encouraging Migration Within Biomaterials

Concomitant to the idea that biomaterial degradability encourages tissue remodeling is the concept of cell migration and invasion into the tissue as part of the remodeling process (142). Two aspects of tissue engineering design factor into migration: first, chemical or physical signals that may induce cells to migrate; and second, how biomaterials may be designed to encourage or discourage migration.

Many factors can induce cells to migrate; in one study, protease-digested fragments from a bone marrow stromal cell-seeded collagen matrix chemotactically induced cell migration in a transwell assay, suggesting that musculoskeletal matrix remodeling may in itself induce stem cell migration (143). Other factors implicated to cause stem cells to migrate include oxidative stress; soluble factors, including serum, platelet-derived growth factor (PDGF) AB and BB, and insulin-like growth factor 1; other soluble cytokines such as macrophage migration inhibitory factor and TGF-β1; and cocultures with other cell types, ostensibly through the release of chemotactic factors (144-153). With regards to other non-soluble signals, durotaxis, or migration in response to mechanical gradients (154-156) and haptotaxis, or migration in response to immobilized signals (157) have also been demonstrated.

Once the appropriate signal to migrate has been provided, multiple factors can affect the extent and form of cell migration, including matrix stiffness and biomaterial MMP sensitivity (158, 159). Several studies have demonstrated $\alpha_v\beta_3$ integrin-linked cell surface localization of MMP-2, assisting in cellular invasion (160, 161). The presence of adhesion peptides within the biomaterial matrix, such as RGD, also appears to be necessary for cells to spread and migrate (162, 163). In 2D and 3D, migration has been shown to be biphasically dependent on the concentration of adhesion ligands; low concentrations prevent generation of force necessary to migrate, high concentrations prevent cells from breaking adhesions to move forward, and intermediate concentrations provide a balance of both (134, 164). However, in 3D, steric hindrance and stiffness of the matrix were computationally modeled to interfere with migration (164). This computational model has been verified in several studies. Maximum migration was found

in gels of the lowest stiffness (165) and is also dependent on high levels of proteolytic degradation to migrate through small mesh sizes such as mesh sizes of PEG gels (166-168). Even with proteolytic degradation, depending on gel sensitivity to degradation, the matrix can still be a barrier for cell proliferation in 3D, depending on the nature of the matrix structure and its degree of crosslinking (169).

2.3.2 Mechanical Stimuli

2.3.2.1 Matrix Geometry and Stiffness

When considering cell differentiation, a cell's mechanical environment, including stiffness and geometry, have been shown to affect cell fate. In particular, extensive investigation has been performed concerning the effects of cell shape on various cell behaviors. An initial hallmark study investigated the effect of area and integrin attachment on cell growth and apoptosis; low areas promoted apoptosis and inhibited growth, while $\alpha_v\beta_3$ integrin binding appeared to promote cell survival (170). Using mesenchymal stem cells, which can differentiate into adipocyte and osteoblast lineages, a separate study demonstrated cell area regulated MSC adipogenic (small area) and osteogenic (large area) differentiation in identical mixed media. Upon further examination, it was shown that the ability to spread, described as cytoskeletal tension regulated by the GTPase RhoA, was the main driver of osteogenic vs. adipogenic differentiation (171). A recent, detailed investigation of cell shape features and MSC differentiation demonstrated that shapes or bioactive factors that enabled higher cytoskeletal tension, even given the same area, would result in increased osteogenic differentiation via a RhoA-driven mechanism (172). Along with geometry, matrix

stiffness can also influence stem cell differentiation. In a seminal paper by Engler et. al, a nonmuscle myosin II-driven mechanism was proposed to explain changes in MSC lineage direction based on matrix stiffness alone; with higher stiffness, MSC focal adhesions increased (173). This has been applied in orthopaedic tissue engineering applications; one recent study used a combinatorial approach to test a range of PEG hydrogel stiffnesses in inducing osteoblast differentiation, as well as demonstrate the feasibility of creating hydrogels with a seamless transition of mechanical properties (174). Interestingly, the influence of initial cell shape on subsequent cell response to mechanical strain has not been previously measured. Studies establishing differences in cell shape prior to mechanical strain in 2D and 3D would provide additional information regarding the influence of cytoskeletal organization on response to inducers of differentiation such as strain.

2.3.2.2 Mechanical Strain

Along with passive mechanical factors, active strain is frequently employed to control stem cell behavior for tissue engineering bone (175), cartilage (176, 177), and especially tendon/ligament (9, 65, 89, 178). Through the use of cyclic mechanical strain, markers of tendon and ligament tissue – collagen I, collagen III and tenascin-C, for example – have been upregulated in cells encapsulated in either natural or synthetic materials (9, 65, 89). While a variety of strain protocols have been employed, a commonly used protocol is 10% strain at 1 Hz (65, 179-182); specifically, a loading protocol of 10% strain at 1 Hz, with 3 hours of active loading and 3 hours of 0% strain, was shown to upregulate expression of collagen I in MSCs encapsulated within a fibrin

construct (183). In our laboratory, tensile culture has been employed to upregulate genes and ECM deposition associated with tendon/ligament fibroblasts, including collagen I, collagen III and tenascin-C (89).

Mechanical strain is thought to induce changes in encapsulated cells via mechanotransduction events through integrin binding and changes in cytoskeletal organization. Using NIH 3T3 cells, one set of experiments showed that mechanical strain was found to activate αvβ3 integrin and increase binding to ECM proteins (184). In one study investigating integrin expression and binding in cells derived from ligament tissue, 7% uniaxial strain was found to upregulate collagen I gene expression (185). Upon further investigation, strain was found to increase α_v expression, and collagen I gene expression was dependent on αvβ3 integrin binding. Integrin binding has been linked to various intracellular pathways including FAK and RhoA/ROCK signaling, which in turn can mediate stretch-induced differentiation of hMSCs (186-188). Thus, integrin binding in PEG-based hydrogels, facilitated through the inclusion of RGD, is a pathway for applied mechanical strain to induce changes in gene expression in encapsulated cells.

2.3.3 Co-culture and Laminated Hydrogels

Due to the zonal nature of the tendon/ligament-bone interface, and because of the widely varying cellular, biochemical and mechanical characteristics within the tissue, a variety of approaches have been employed to engineer the interface (4). As previously mentioned, multiphase scaffolds have been employed; however, an important aspect of interface tissue design has been the use of multiple cell types. In a 2D coculture study of fibroblasts and osteoblasts, markers reflective of fibrocartilaginous tissue, such as

collagen type II and aggrecan, were detected following 21 days of culture (189). In a study using a compound 3D scaffold with three different regions, co-cultures of fibroblasts and osteoblasts resulted in a collagen I matrix being deposited throughout the ligament and interface portions of the scaffold, with detectable mineralization in the osteoblast compartment (78). Moreover, a triculture of fibroblasts, chondrocytes and osteoblasts in a similar multiphasic system resulted in a collagen II and proteoglycan rich region between the fibroblast and chondrocyte layers (5).

Co-culture may also be enabled in hydrogel materials by laminating sections together during polymerization; this has been demonstrated in OPF and PEG-DA hydrogels using a thermally-based free radical initiator, with no reduction in the mechanical properties of the interface (104). Subsequent studies have employed photoresponsive radical initiators and microfluidic systems to generate patterning of multiple cell types (190). Laminated hydrogels have been frequently explored in orthopaedic tissue engineering, mostly as strategies for generating osteochondral scaffolds. In one *in vivo* study, MSCs differentiated with either osteogenic or chondrogenic medium were seeded into either end of a laminated hydrogel, created through sequential photopolymerization. Following 12 weeks of implantation, histology identified stratified layers of cartilaginous and osseous tissues, with infiltration between tissues (87). Another study used multilayer constructs to link chondrocytes extracted from superficial and deep zones of cartilage in proximity to recreate the zonal organization of articular cartilage (191). Recently, multilayer scaffolds have also been used to encapsulate MSCs for osteochondral regeneration (192); in two recent studies, biochemical composition of photopolymerized scaffolds was shown to direct a single

MSC population to differentiate into the superficial, transitional, and deep zones of articular cartilage, both as separately designed scaffolds and as one multi-layer hydrogel (193, 194).

Such laminates afford the capability to investigate paracrine signaling between multiple cell types, detecting changes in markers of differentiation in one cell type due to soluble signals from another cell type in proximity. Understanding these fundamental relationships between cell types in 3D co-culture can improve efforts to generate heterogeneous constructs that mimic elements of the tendon/ligament-bone interface.

CHAPTER 3

METHOD FOR DETERMINING CELL VERTICAL POSITION IN LAMINATED PEG-BASED HYDROGELS

3.1 Introduction

In tendon and ligament tissue engineering, one of the critical goals in modeling the tissue environment and fabricating replacement biomaterial constructs for therapeutic use is engineering the interface between tendon/ligament and bone (3, 4). The interface is composed of heterogeneous regions of tissue, transitioning from a highly fibrous and aligned collagen matrix, through regions of cartilaginous and calcified cartilaginous tissue, to highly calcified bone (18). Interfaces between tendon/ligament and bone have been studied using a variety of tissue engineering strategies that can often involve constructs with controlled heterogeneity. This includes the formation of multiphase matrices (5), single hydrogels with gradients of differentiated osteoblasts (6), and scaffoldless approaches using monolayers that are directed to spontaneously form bone-ligament-bone-like structures (7, 8).

In heterogeneous structures, cell migration has been implicated in construct regeneration. In one study, 3D triphasic matrices were used to coculture fibroblasts and osteoblasts on separate sides, with a cell-free layer in the middle. Following 5 weeks of culture, cells had migrated into the middle region, with increased matrix production and vascularization in the previously cell-free layer (78). Directed migration on and within materials has been attributed to haptotaxis (157) as well as chemotaxis; that is, soluble gradients of chemotactic factors that induce cells to migrate. Such soluble factors may be generated by different cell types when in coculture. For example, MSCs have been also

shown to migrate in a distance-dependent manner when co-cultured with endothelial cells in a microfluidic-patterned scaffold (148). Chemotactic factors may thus encourage cells to migrate as part of tissue repair.

Biomaterial model systems enable simultaneous examination of migration within a material as well as the formation of multi-layer materials. This laboratory has explored the use of poly(ethylene glycol) (PEG), a synthetic polymer that can be thermally- or photo-crosslinked to form a hydrogel that provides a "blank slate" for providing bioactive functionalities to cells (195). Cell migration has been employed in PEG hydrogels to study neural stem cell-ECM interactions (196, 197), angiogenesis (138, 198, 199), and bone defect repair (98, 127). In natural polymers such as collagen, cell migration is facilitated via larger pore sizes and the fibrillar structure of the material (167). However, proteolytic activity in PEG gels is necessary to allow migration in 3D due to a small pore size that restricts movement (165) by the integration of protease-sensitive peptides (133, 134). By also including adhesion sites, which are necessary for cell spreading and migration, synthetic hydrogels can enable study of cell migration (10, 140, 163, 200); controlled spatial patterning of adhesive ligands to direct cell movement within enzymatically sensitive gels has been previously investigated (201, 202).

In addition to enabling migration within homogeneous scaffolds, PEG-based gels have also been used to form laminated structures, where the initial layer is only partially crosslinked before another layer is added and crosslinked into the first (104). Laminated hydrogels have been used for a variety of orthopaedic tissue engineering applications, mostly with applications towards cartilage and osteochondral interface tissue regeneration (87, 191, 192, 194). Depending on the crosslinking time of the first layer,

addition of the second layer causes intermixing of both layers; thus, the thickness of the interface between two hydrogel layers can be manipulated (191). While many aspects of the laminate interface have not been studied, it is posited that, due to interpenetration of the second layer with an already polymerized hydrogel, that the interface likely exhibits a smaller mesh size than either of the two adjoining layers. A smaller mesh size would limit diffusion (203, 204) and cell movement through an interface would require additional proteolytic degradation to create pore sizes large enough for cell movement (168). The customizability of PEG gels allow these parameters to be studied in close detail.

To investigate aspects of the interface, PEG gels offer a controlled system with which enzyme sensitivity and other gel parameters can be closely studied as it relates to migration through multiphasic structures to model interface development. However, no techniques currently exist for monitoring the position of cells over time in with regard to their 3D movement through a multi-layer material; systems to track 3D cell migration either employ radial migration from a fibrin clot, in which migration is random and undirected; or individual 3D cell tracking, which provides precise information about a single cell's movement but cannot be performed on a large scale (205). Thus, the goal of this particular work was to develop a system for monitoring cell Z-position that could be employed towards tracking the large-scale migration of cells within a 3D laminated hydrogel structure for use in exploring interface tissue engineering. To do this, bovine MSCs and a highly migratory human fibrosarcoma cell line (HT-1080) were encapsulated within a single layer of a dual-layer PEG hydrogel and cell Z-position was determined at 1 and 7 days.

3.2 Methods

3.2.1 Polymer synthesis

OPF was synthesized as previously reported (102). Briefly, poly(ethylene glycol) (Mn = 10,000 Da; Sigma–Aldrich) was azeotropically distilled and subsequently dissolved in distilled methylene chloride (MeCl; Fisher) to produce a ~40% (v/v) solution. Distilled fumaryl chloride (FuCl, Sigma–Aldrich) and triethylamine (TEA; Sigma–Aldrich) in a molar ratio of 1 PEG:0.9 FuCl (2 TEA:1 FuCl) were slowly added dropwise to the PEG solution, and the reaction was held under nitrogen on ice. The OPF formulation was continuously stirred for 48–72 h at 25°C under nitrogen to ensure reaction completion. Next, excess methylene chloride was evaporated and the Cl–TEA salt was removed by filtration (Whatman). The OPF was recrystallized twice in ethyl acetate (Fisher) and washed three times in ethyl ether (Fisher). The resulting powder was vacuum dried at <5 mmHg and stored in a sealed container at -20 °C until further use.

PEG-DA was also synthesized as previously reported (157). Briefly, 24 g PEG 3.4K (Sigma-Aldrich) was dissolved in 60 mL distilled MeCl, then reacted at a 2:1 molar ratio with acryloyl chloride (AcCl, added dropwise, Sigma-Aldrich) and at a 1:1 molar ratio with TEA to create a 40% (w/v) solution under nitrogen overnight. Workup was performed by reaction with 2M K_2CO_3 (Fisher) at a 2:1 K_2CO_3:AcCl molar ratio and separation into aqueous and organic phases. This was followed by drying the solution with anhydrous $MgSO_4$ (Fisher) and precipitating the polymer in ethyl ether (Fisher). Product was filtered, vacuum dried and frozen at -20ºC until use.

PEG-DA (M_n 3770 ± 10, PI 1.1 ± 0.0), PEG 3.4K (M_n 3400 ± 30, PI 1.1 ± 0.0), OPF 10K (M_n 19,800 ± 100, PI 4.6 ± 0.1) and PEG 10K (MW 12,900 ± 200; PI 1.1

± 0.0) were characterized via gel permeation chromatography as previously reported (109).

To create enzymatically-degradable PEG, the unmodified peptide Gly-Gly-Gly-Leu-Gly-Pro-Ala-Gly-Gly-Lys (GGGLGPAGGK; Aapptec, Louisville, KY) was reacted with Acrl-PEG-succinimidyl valerate (Acrl-PEG-SVA, MW 3400; Laysan Bio, Arab, AL) at a 1:2.2 peptide:Acrl-PEG-SVA molar ratio in 50 mM $NaHCO_3$ buffer (Fisher) at pH 8.5 for 3h. The resulting solution, Acrl-PEG-GGGLGPAGGK-PEG-Acrl (enzymatically-degradable PEG), was then dialyzed for two days and lyophilized to form the final product. Similarly, the peptide GRGDS (EMD Chemicals, Gibbstown, NJ) was reacted at a 1:2 molar ratio with Acrl-PEG-SVA, then dialyzed and lyophilized to synthesize Acrl-PEG-GRGDS (RGD).

3.2.2 Cell sources

Bovine marrow stromal cells (MSCs) were harvested via a previously described protocol (118). The femur and tibia of an immature calf were isolated (Research 87, Boylston, MA), and marrow was placed into low glucose DMEM containing 10% FBS, 10 mL/L A/A, and 0.01% basic fibroblast growth factor (bFGF; PeproTech, Rocky Hill, NJ). The resulting tissue was then physically disrupted by repeatedly pipetting using 50 and 10 mL pipettes, followed by 16, 18 and 20 gauge needles. After centrifugation, the fatty layer was removed and the mixture was plated for 30 min to allow rapidly adhering cells to adhere to tissue culture plastic. The remaining cells in solution were then expanded in T-150 tissue culture flasks until confluency, then placed in Dulbecco's Modified Eagle Medium (DMEM; Mediatech) with 20% fetal bovine serum (FBS;

Hyclone, Thermo Fisher, Waltham, MA) and 10% DMSO and stored in liquid nitrogen until further use. HT-1080 cells (American Type Culture Collection; Manassas, VA) were cultured according to manufacturer's guidelines in Eagle's Modified Essential Medium (EMEM; Mediatech) augmented with 10% FBS, 10 mL/L A/A, 1 mM sodium pyruvate (Mediatech) and 1% non-essential amino acids (Mediatech). Before encapsulation, cells of either cell type were replated for 3 days in T-150 tissue culture flasks in their respective media to eliminate transitory effects from the thawing process.

3.2.3 Hydrogel formulations

In all experiments, total polymer was 10% of the initial total gel weight. Polymer formulations consisted of either enzymatically-degradable PEG or a mixture of 50% OPF 10K and 50% PEG-DA by weight. Thus, a 0% enzymatically-degradable PEG hydrogel would consist of 50% OPF 10K, and 50% PEG-DA by weight. Acrl-PEG-GRGDS at 1 μmol RGD/g swollen gel was added to facilitate cell adhesion. To distinguish one layer from another, 500 μM rhodamine methacrylate was added to enable visualization of the layer. After dissolving the polymer formulation in phosphate buffered saline (PBS; Invitrogen) and sterile filtering, 18 mM ammonium persulfate (APS; Sigma-Aldrich) and 18 mM tetramethylenediamine (TEMED; Sigma-Aldrich) were used to thermally crosslink each gel for 10 min. Information regarding the investigation of hydrogel properties and degradation due to incorporation of enzymatically-degradable peptides into PEG hydrogels can be found in Appendix A; the enzymatically degradable peptide used in this study was the "slow-degrading" peptide characterized there.

3.2.4 Encapsulation and lamination

To examine cell migration between two layers, hydrogel laminates were formed in 13-mm diameter, 1.5-mm deep two-stage Teflon molds (see Figure 3.1 for diagram). First, a polymer solution containing 500 μM rhodamine methacrylate (Sigma) was deposited into a Teflon well and, using a reverse mold, gels were created approximately 400-500 μm thick. Following polymerization, a second layer was added on top of the first layer and allowed to polymerize. This created a heterogeneous hydrogel laminate that was approximately 1 mm thick overall. In layers with cells, either MSCs or HT-1080s were seeded at 20 x 10^6 cells/mL. The experimental groups were composed as follows:

- Group A: top, bovine MSCs in 0% or 100% enzymatically-degradable PEG; bottom, 100% enzymatically-degradable PEG dissolved in PBS.
- Group B: top, HT-1080 cells in 0% or 100% enzymatically-degradable PEG; bottom, 100% enzymatically-degradable PEG dissolved in PBS.
- Group C: top, HT-1080 cells in 0% or 100% enzymatically-degradable PEG; bottom, 100% enzymatically-degradable PEG dissolved in serum.
- Group D: top, cell-free 0% enzymatically-degradable PEG;
  bottom, HT-1080 cells in 0% enzymatically-degradable PEG, dissolved in PBS.

Groups A and B were studied to explore the effects of enzymatically-degradable PEG and characterize changes in cell position between the two different cell types. Group C was included as a first pass at studying the effect of chemotactic factor diffusion on changes in cell position. Finally, Group D was included to determine the accuracy in distinguishing cells that were in the second layer instead of the first layer.

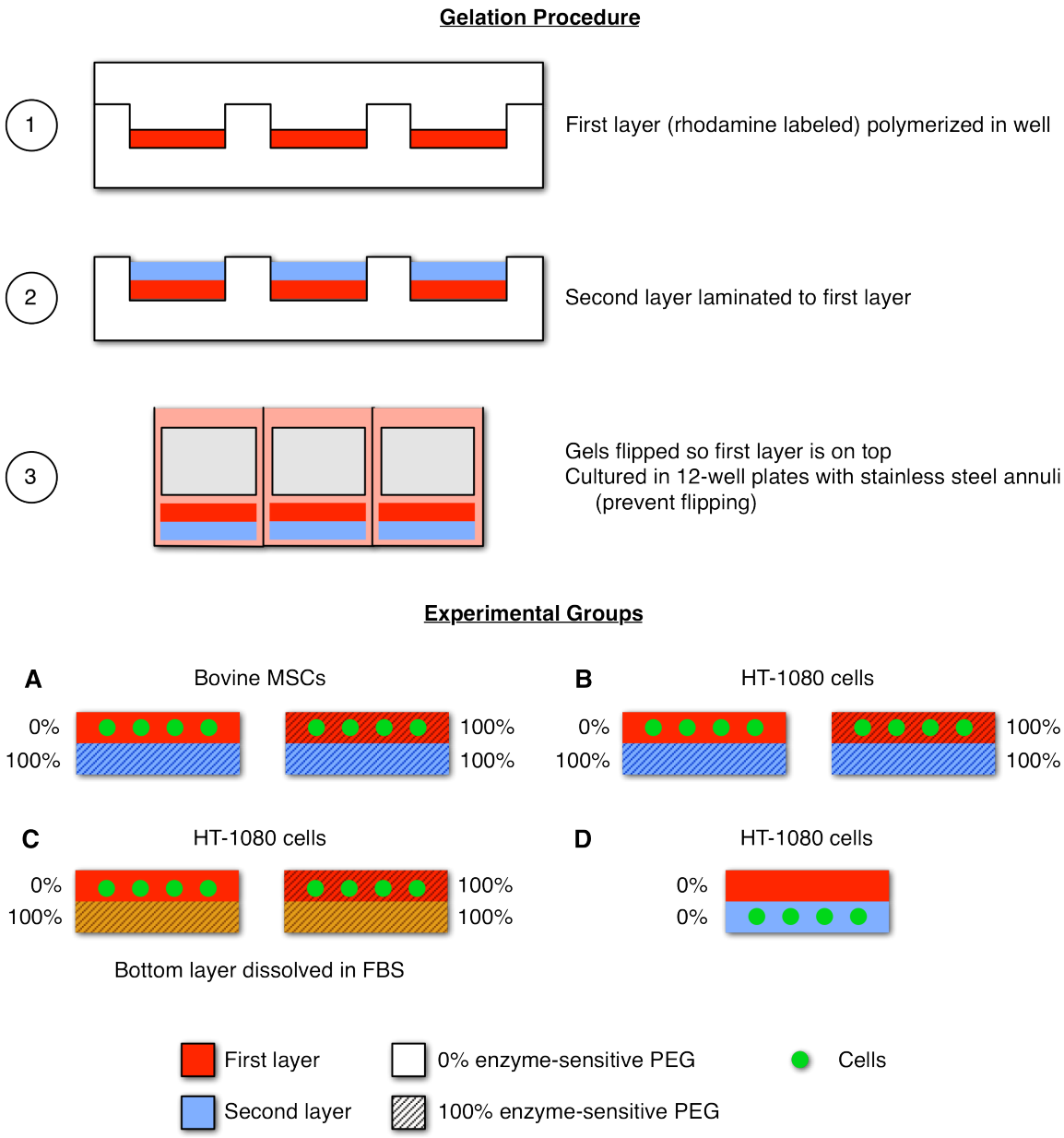

Figure 3.1. Diagram of gel polymerization and experimental group setup.

Following polymerization of both layers, constructs were flipped so the first layer was above the second one, and cultured in 12-well plates containing the appropriate medium for that cell type. At 1 day, gels were moved to 24-well plates and stainless steel annuli were placed on top of each gel to prevent gels from flipping over in each well.

Appropriate medium for each cell type was changed every 2-3 days thereafter.

3.2.5. Cell position analysis

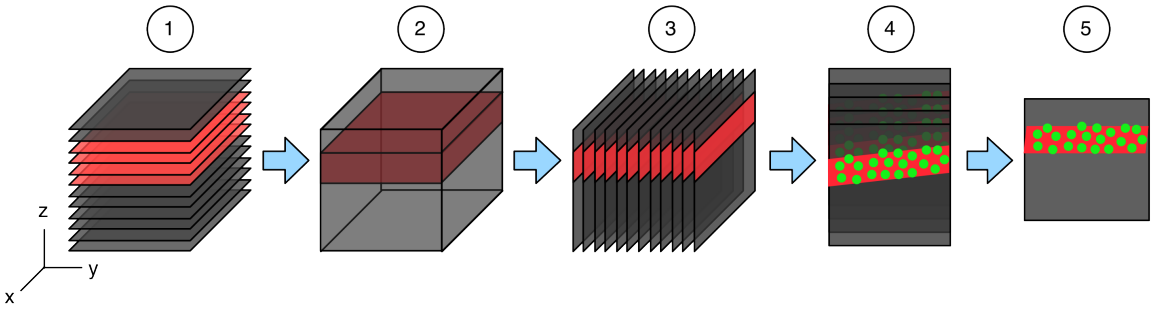

Figure 3.2. Diagram depicting image analysis.

At 1d and 7d after encapsulation, gels (n=3) were stained with 1 µM calcein AM (Invitrogen) for 1 h and imaged using confocal microscopy to evaluate cell migration through each construct. Three Z-stacks for each construct, with an interval of 10 µm, were taken through the entire detectable thickness of the hydrogel (Figure 3.2, **1**) and subsequently processed using custom macros written in ImageJ. First, Z-stacks (900 x 900 µm in the XY-plane) were resliced every 5 µm to create Y-stacks of images in the XZ-plane (Figure 3.2, **2-3**). As gels were often not parallel to the imaging surface during imaging, the skew in the first and last image of each resliced stack was manually measured. A macro in ImageJ subsequently rotated each image in the resliced stack, reversing skew and translating the image to align the entire stack along the Z-direction (Figure 3.2, **4-5**). Finally, images were compressed into a single XZ image using the maximum pixel intensity along the Y-axis for each pixel (Figure 3.2, **5**), and green pixels (representing live cells) were binned every 50 µm according to their distance within and away from the cell layer. By measuring each individual image stack, the thickness of the

red hydrogel layer could be determined, and was used to calculate the percentage of green pixels that were computed to have a Z-distance beyond the red layer.

3.2.7 Statistics

Data are represented as mean ± standard deviation. Data were normalized with a Box-Cox transformation and were statistically compared using a three-factor ANOVA with Tukey's HSD *post-hoc* test. The factors were encapsulation type (MSCs with PBS blank layer, HT-1080s with PBS blank layer, and HT-1080s with FBS blank layer), gel type, and day.

3.3 Results

3.3.1 Monitoring of cell position

Cell encapsulation in a hydrogel with incorporated rhodamine methacrylate resulted in the visualization of green cells seeded within a red layer of hydrogel (Figure 3.3). The average thickness of the cell layer across all gels was 470 ± 80 μm; there was no significant variation between gels of different formulations (data not shown). The tilted appearance of some imaged gels originates from a slight tilt in the gels themselves as they were imaged. Due to the lack of accurate resolution in the Z-direction, errant capture of light above and below the position of the actual cell distorted and stretched the vertical appearance of encapsulated cells. Moreover, in some cases, considerable settling of cells led to cells being seeded far away from the lamination point. At both 1 and 7 days, few cells were visually observed beyond the end of the red hydrogel layer. This pattern was consistent across MSCs and HT-1080 cells, across seeding in 100% or 0%

enzymatically-degradable PEG gels, and across bottom layers polymerized in either FBS or PBS (Groups A, B and C). In laminated gels where cells were seeded in the bottom layer (Group D), both top and bottom layers were clearly demarcated by rhodamine and calcein-stained cells, respectively.

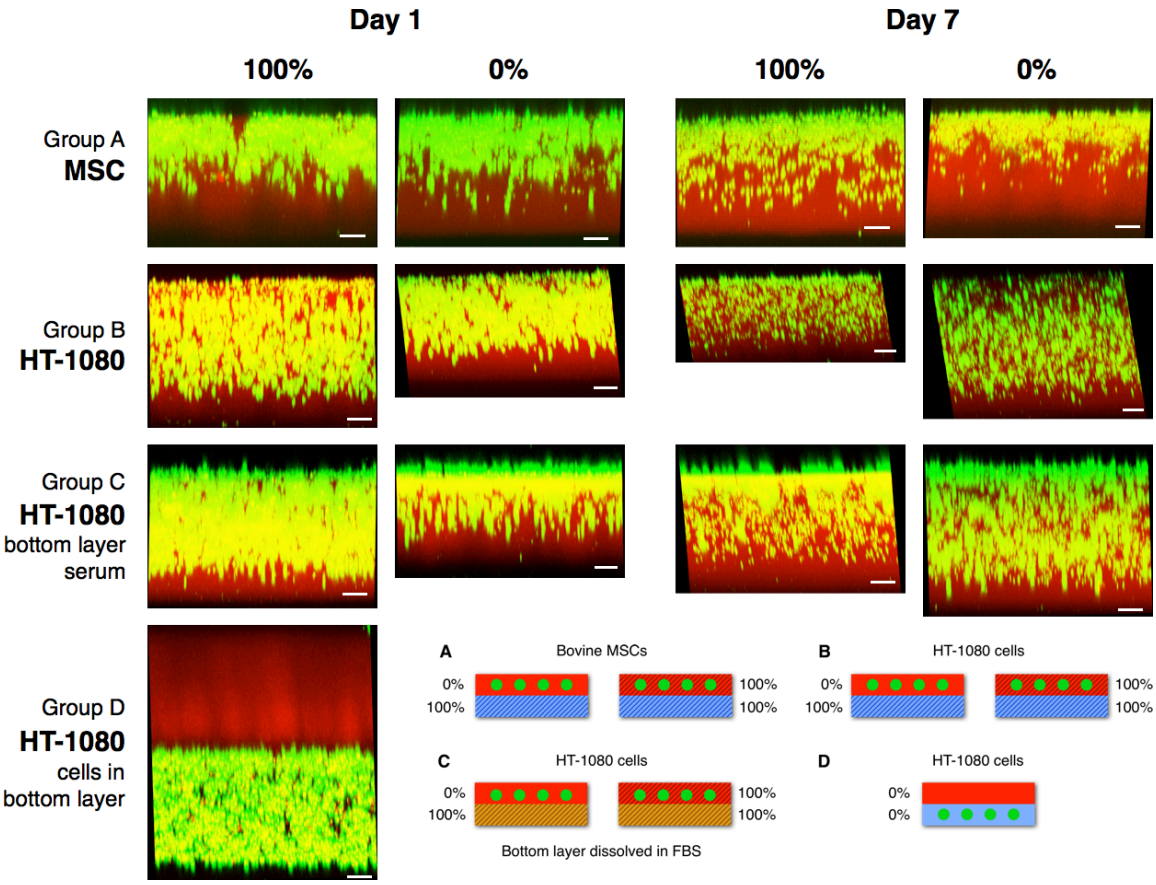

Figure 3.3. Confocal images (XZ-plane) of bovine MSCs and HT-1080 cells encapsulated in either 0% or 100% MMP-cleavable PEG hydrogels at 1 and 7 days. For Groups A, B, and C, only the first rhodamine labeled layer is shown; the rest of the gel was not visible. For Group D, both layers are visible. Experimental group setup is shown at the bottom right. Scale bar: 100 µm.

3.3.2 Image analysis

The normalized distributions of green within each hydrogel group at day 7 were plotted (Figure 3.4). Cells that were seeded in the bottom layer (Group D) were easily detected by image analysis; 99.6% of green was not in the red layer (data not shown). In Groups A and B, where the bottom layer was instead a cell-free layer that had been polymerized in PBS, the distribution of green pixels did not appear to vary, regardless of cell type or top layer gel type. However, when the bottom layer was polymerized in FBS instead (Group C), the distribution of green visually appeared to extend somewhat further than other formulations. At day 1, all Group C constructs displayed greater percentages of green beyond the cell layer than their Group A and Group B counterparts (Figure 3.5). Group B 0% constructs also displayed greater percentages than Group A 0% constructs. At day 7, the average percentage of green in Group C 0% gels was significantly greater than in Group A constructs. Time dependence on the percentage of green was not detected.

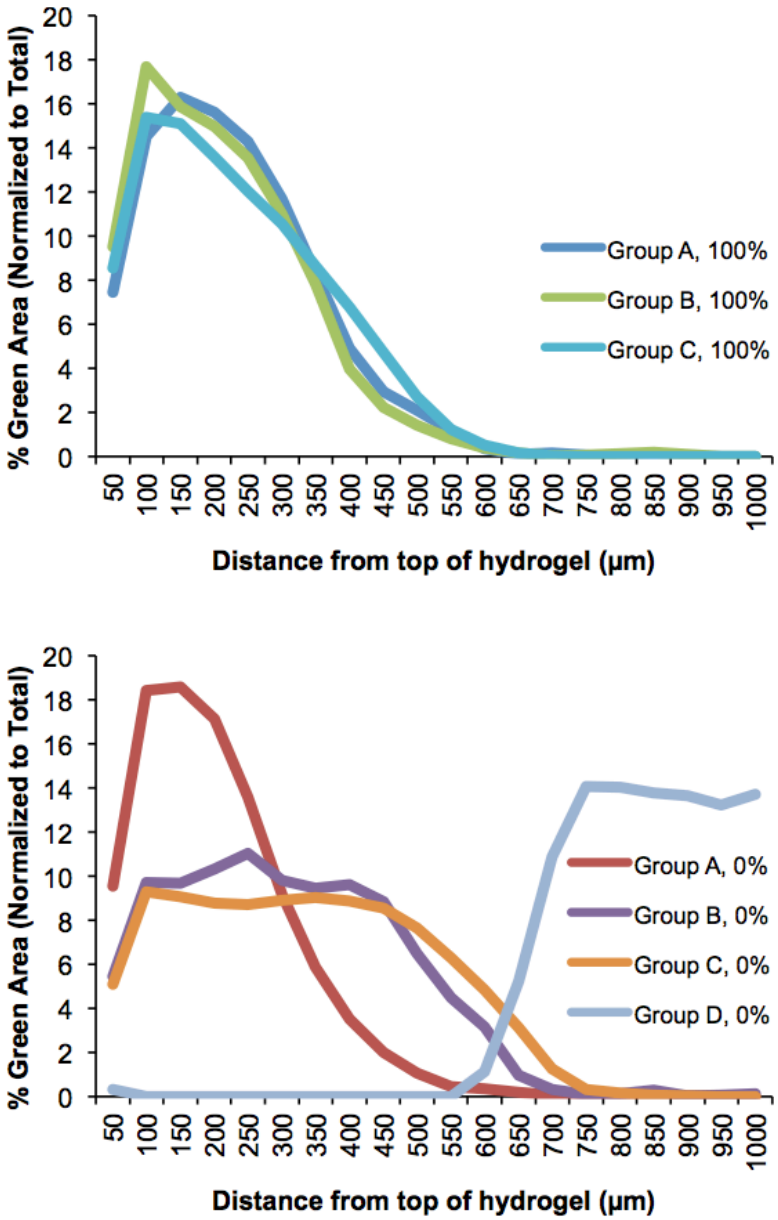

Figure 3.4. Average distribution of green pixels through the hydrogel, starting from the top of the cell layer, at day 7 (n=3). HT-1080s seeded in bottom layer (Group D, 0%) was analyzed at day 1.

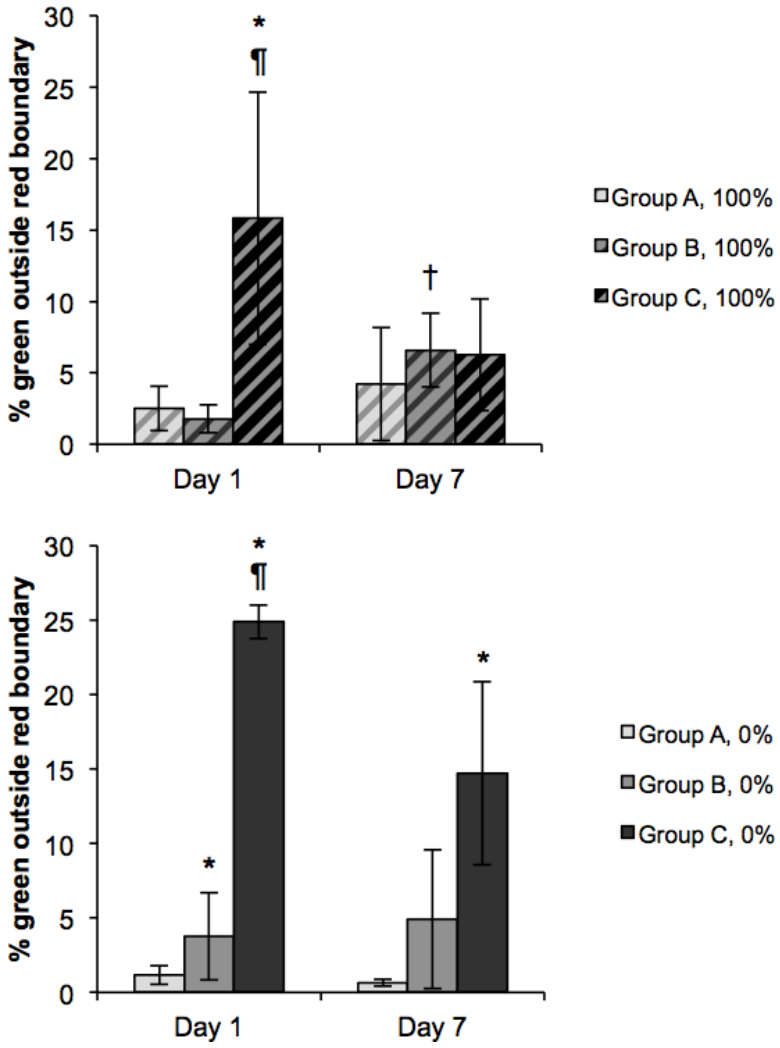

Figure 3.5. Percentage of green pixels with a z-distance past the measured red hydrogel layer. * significantly different from MSCs in the same gel type. ¶ significantly different from HT-1080s of same gel type. † represents different from day 1 time point of same gel type (n = 3-4 ± SD, $p < 0.05$).

3.4 Discussion

In order to model and regenerate tissue interfaces, multiphasic hydrogels may be employed to separate cell types and mimic aspects of the transition. It is also believed that migration within constructs, possibly generated by chemotactic factors from cocultured cells, may be involved in regeneration of the interface. PEG-based systems

have employed MMP-sensitive peptides and adhesion peptides to facilitate cell spreading and migration within crosslinked scaffolds. To track possible migration in multi-layer materials, however, new techniques are required for monitoring cell movement in 3D. The goal of this particular study was to develop a method towards tracking large-scale cell movement in a multi-layer hydrogel, using bovine MSC and HT-1080 fibrosarcoma cells as candidate cell types for encapsulation.

The two-stage process used for encapsulating cells led to the formation of a two-layer gel (Figure 3.3). Cells were seeded in a rhodamine-labeled layer composed of either 0% or 100% enzymatically-degradable PEG, and were then laminated to a cell-free layer of 100% enzymatically-degradable PEG. Lamination generated a consistent delineation between layers; using seeded cells to represent a second layer, confocal imaging revealed a distinct lamination point between gel sections (Figure 3.4 bottom left). Cell movement beyond the red layer was thought to be indicative of migration across the laminated interface. However, cells settled as gels polymerized, leading to the inconsistent placement of most cells far away from the interface; observationally, this appeared to be more of an issue with 100% enzyme-degradable gels, as the prepolymer solution viscosity appeared to be lower relative to 0% enzyme-degradable gels. Consequently, when combined with the significant thickness of the gel layer (around 470 μm), it was not even possible to identify cells that had moved within the cell layer but that had not moved across the interface. Settling also placed most cells hundreds of microns away from the point of lamination, requiring most cells to migrate substantial distances before capturing with this analysis. Future work, however, could exploit cell settling to move cells closer to the interface; additionally, reducing the thickness of a cell-seeded layer in

future work would reduce the distance required to migrate towards the point of lamination.

Confocal imaging provided information regarding the 3D position of cells within a gel; in addition to XY-positions, repeated XY imaging through the thickness of a construct provided crucial Z-position information. However, there were limitations associated with imaging that somewhat restricted the utility of this information. Tilting of gels could not be controlled during imaging, and subsequently distorted the precise coordinates of cells within the gel. To compensate, resliced image stacks were manually measured and rotated/translated to account for image skew. Following correction of manual tilt, representative 2D images were projected from each resliced stack, using green pixel data to represent the presence of cells. Compared to the data available in a normal image stack, one dimension (Y) was lost to retain XZ data of cells. The influence of multiple cells in the XZ plane aligned along the same Y-coordinate was lost in the summation; this is reflected in the scattered nature of images in Figure 3.3. Additionally, given the fundamental limitations of standard confocal microscopy, cells were distorted in the Z-direction due to light above and below the cell that was captured during imaging. Finally, the thickness of the gels (~1000 μm) at times prevented practical imaging through the complete thickness of the gel, weakening the reliability of Z-distance data at the edges of the hydrogel.

However, despite these limitations, cells seeded in the bottom layer could still be easily identified (Figure 3.3 bottom left, Figure 3.4 bottom), demonstrating the general accuracy of this type of image analysis. When compared to other work, this analysis technique compares favorably in terms of data collected. (205). In radial migration and

other coculture studies, although cells are technically seeded in a 3D gel, 2D migration is what was actually measured (98, 140, 142, 148, 167, 201). In studies that track individual cell migration, 3D movement is captured and measured via confocal microscopy, but tracking has not been scaled to large-scale monitoring of directed cell movement (137, 200, 206). Finally, in transwell studies, information regarding cell migration is binary, with little knowledge regarding distance, and migration can be affected by other factors, such as pore sizes in the transwell insert and adherence to the filter membranes (134, 205, 207). Using the analysis technique developed here, data along one dimension was lost in favor of measuring cell position along the Z-axis, something that has not been previously done on a large scale. In future work, however, enhanced imaging techniques, such as two-photon confocal microscopy, could determine cell Z-positions more accurately. It would then be quite feasible to discard potentially ambiguous pixel data in favor of using thresholding and particle analysis, linking between multiple images, to enable the determination of individual cell X, Y, and Z coordinates within a material. Coupled with live cell imaging, cell tracking of large numbers of cells could combine the current large-scale analysis of XY-data with the finesse of individual cell tracking in 3D.

Overall, few cells were observed beyond the red layer in microscopy images. However, a percentage of HT-1080s encapsulated in gels and laminated to blank gel layers polymerized in serum appeared to reside beyond the blank layer as determined by image analysis (Figures 3.4, 3.5). Serum contains multiple chemotactic factors, and human MSCs migrate in response to serum (153). HT-1080 cells have been shown to migrate over great distances in response to certain chemotactic factors. In one experiment, HT-1080 cells migrated 700 μm over 48 hours in 3D collagen gels in response to

lysophosphatidic acid (LPA) and sphingosine 1-phosphate (S1P) (208). However, studies to validate HT-1080 chemotaxis in serum were not performed in this study, and random cell motility was not verified prior to use. Moreover, serum was not explicitly retained in the gel during polymerization, and would have likely diffused from the matrix during and after swelling. Thus, any effects would only be observed over short periods of time. Although the distribution of green in these laminated gels appeared to extend beyond the original cell layer, this conclusion is, again, severely limited by the previously discussed microscopy limitations. Future efforts could use hydrogel layers modified to release specific chemical factors over a specified time period to observe long-term migration (204). Such a system would also have to restrict physical diffusion of chemotactic factors outside of the hydrogel scaffold, to ensure the formation of a chemical gradient.

One limitation throughout this study was the use of an enzymatically-degradable peptide sequence that was hypothesized to be cleavable by MMPs with specificity for collagen type I (133). Specific cleavage kinetics of this sequence using different MMPs and other enzymes have not been determined. However, since the development of this sequence, other peptide sequences have been developed with extremely high sensitivity for MMP-1 and MMP-2 (139, 140). The types of MMPs secreted by bovine MSCs and HT-1080s were not characterized in this study; however, HT-1080s have been shown to express abundant MMP-1 and MMP-2 (209). The use of peptides highly sensitive to proteases secreted by encapsulated cells are required to enable sufficient degradation of the matrix to allow migration over time (165). At the time that this study was performed, however, sequences with greatly increased susceptibility to protease degradation were not available. Future work could utilize faster-degrading sequences, for example, the fast-

degrading sequence GGVPMSMRGGGK that was investigated in Appendix A and Chapter 5.

Large-scale migration of cells was investigated in this study as part of possible cell infiltration through the interface of a synthetic, protease-sensitive construct. Significant cell infiltration and remodeling of MMP-sensitive PEG hydrogels has been previously demonstrated in a rat cranial model; however, the time scale of such remodeling was five weeks, significantly longer than this 7-day study (98). Nevertheless, migration through laminated PEG gels has not been previously demonstrated. Limited work has been done to characterize the nature of the interface as it pertains to crosslinking time (191); however, the mesh size and permeability of such an interface has not been investigated. To laminate a second layer, the prepolymer solution must interpenetrate and entangle with the first layer of gel as it polymerizes. Consequently, it is expected that average mesh size in the interface would be reduced, limiting diffusion and thus the movement of chemotactic factors (203, 210). A decreased mesh size would also further restrict migration through the interface given the increased number of sites to proteolytically cleave. Thus, it may be that the interface itself will not function as the primary gateway for soluble factor diffusion; diffusion into surrounding medium may be just as or more relevant. Future models of migration could act to encourage directionally persistent cell migration through generation of directed chemotactic gradients and construct environments that facilitate movement in a single direction, such as an aligned biomaterial scaffold (211). In developing those models, use of the technique described here would provide significant insight into the 3D position of cells migrating within a multi-layer construct. Future refinement of this system would enable high-throughput cell

tracking through improved microscopy techniques and subsequent image analysis.

3.5 Conclusions

The experiments in this study demonstrate the use of a protease-sensitive synthetic hydrogel that can be laminated to create a multi-layer scaffold with defined separation of cells. Such a system could be used to investigate possible chemotactic migration of cells through the lamination interface. The technique outlined in this work provides additional information regarding the 3D position of cells within a multi-layer hydrogel. However, significant improvements are needed to design a system that can effectively induce and monitor large-scale migration in specifically targeted cell types using a chemical gradient. Such a system would provide new insight into the nature and extent of cell movement in response to soluble signals to invade and remodel interface tissues.

CHAPTER 4

FINITE ELEMENT MODELING PREDICTS STRAIN DISTRIBUTION IN PEG HYDROGELS UNDER CYCLIC TENSILE STRAIN

4.1 Introduction

A number of tissue engineering models exist for engineering tendon and ligament tissue (29). Many strategies have used tensile strain to upregulate genes associated with tendon and ligament fibroblasts (9, 65, 89). However, certain behaviors, including collagen III expression, have been previously reported to be strain dose-dependent (212, 213). A highly variable strain distribution within a tissue engineering construct would therefore make it difficult to correlate applied overall strain with bulk encapsulated cell response, as cells in certain regions of a material may experience lower or higher local strains than the macroscopically applied strain. To shed insight into the distribution of strain, finite element modeling has been employed to computationally model a scaffold with specified mechanical properties. Detailed information can then be predicted regarding the distribution of strains and forces throughout the material when macroscopic strain is applied. Computational modeling enables the facile investigation of hypothetical loading scenarios and provides physical data that may be difficult to determine otherwise. For example, finite element modeling has simulated the effects of the pericellular matrix on the micromechanical environment of chondrocytes undergoing loading (214, 215); whole knee joint kinematics including bones, tendons and ligaments (216); and shear stresses due to fluid flow in native tendon tissues (217).

The work in this dissertation (Chapter 5) employs the use of a tensile culture bioreactor which has been used to study the application of cyclic tensile strain on cells

encapsulated in hydrogel-based scaffolds (89, 178, 218). In the initial design of this system, a finite element model was developed to characterize the distribution of strain under different loading amplitudes. However, due to the way in which constructs were strained, where a metal peg directly interacted with holes punched into the constructs, the model revealed significant variation in strains throughout the construct; under 10% applied strain, local principal strains varied from approximately 0.5-5.5% (218). To improve the uniformity of applied strain, a newer construct design allowed integration of prepolymer solution into porous polyethylene endblocks, enabling strain to be applied to the stiff endblock instead of directly to the gel (178). This construct design was recently employed in our laboratory to investigate the effects of 10% cyclic strain on the upregulation of MSC gene expression and ECM deposition associated with tendon/ligament fibroblasts (89). In both of these studies utilizing the newer construct design, however, the distribution of strain throughout the hydrogels used was not characterized. Thus, it was important for this work, and for future studies using this tensile culture bioreactor, to evaluate the distribution of principal strains within a representative construct undergoing cyclic tensile strain. Such data would provide validation of the construct design and justify analysis of encapsulated cells as a single population.

The poly(ethylene glycol) (PEG)-based hydrogels used for the aforementioned study (89) have been used to successfully encapsulate cells for a wide variety of tissue engineering applications (97, 98, 219). By modifying poly(ethylene glycol) with acrylate groups, PEG is made crosslinkable via photo- and thermally-sensitive free radical initiators (105, 112). The nature of PEG free radical polymerization allows the lamination

of multiple gels by partially crosslinking one gel before depositing the next liquid prepolymer (87, 104, 190). By controlling crosslinking and lamination, multiple gel types can be patterned next to each other, each with specifically tailored cellular or mechanical characteristics (104, 190). Laminated structures have been employed to model and study complex tissues, including cartilage (191, 194). Other types of heterogeneous structures have been employed as models for interfacial tissues, including the insertion of tendon/ligament into bone (5, 6, 78). These structures typically contain variations in geometry, biochemical/cellular composition, and/or mechanical properties.

If strain is applied to heterogeneous materials, finite element modeling provides the ability to anticipate variations in local strain based on differences in material geometry and mechanical properties. For example, in a recent study, tensile strain was been used in tandem with scaffold geometry to facilitate spatially heterogeneous cell differentiation based on a predicted distribution of compressive and tensile forces (65). Mismatches in mechanical properties and differences in laminate geometry could modify the distribution of strain within a heterogeneous material. Moreover, the distribution of strain may change temporally due to material remodeling by encapsulated cells (6).

Thus, there were two objectives in this work. First, a finite element model was developed to characterize the uniformity of local strains in hydrogels cultured in a tensile culture bioreactor. Next, models incorporated different interface geometries and differences in stiffness between laminated sections, to determine the extent of changes in strain distribution due to the laminate interface and mismatches in stiffness in different sections of the hydrogel. Lastly, a first pass was made at testing assumptions that were made in the development of the finite element models by measuring the tensile modulus

of PEG-based hydrogels.

4.2 Methods

4.2.1 Finite element modeling

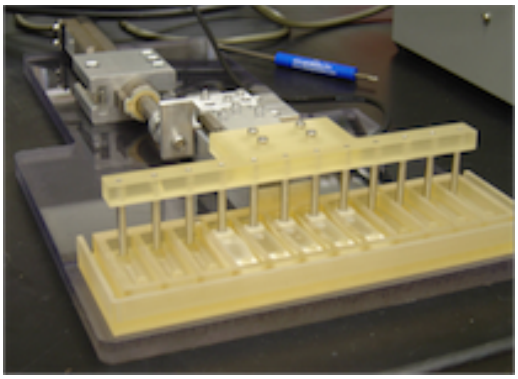

Figure 4.1. Image of fabricated gels in tensile culture bioreactor.

A finite element (FE) model of the PEG hydrogel construct was developed with Abaqus 6.11-1 (Simulia, Providence, RI) to analyze the strain distributions during tensile loading. The model was developed from an existing tensile culture bioreactor (Figure 4.1). The hydrogel (9.5 x 12.5 x 1.6 mm) was modeled using 11400 linear elastic elements with reduced integration (C3D8R) and the endblocks (9.5 x 7.5 x 1.6 mm) were modeled using 5010 linear elastic elements (C3D8R). The gel was assigned an isotropic modulus of 22 kPa and an assumed Poisson's ratio of 0.3 to compare with a previous finite element model used with this system (195, 218). The polyethylene endblocks were assigned a much higher modulus relative to the gel (10 MPa). The gel was fixed to each endblock at both ends. To simulate peg displacement similar to the tensile culture bioreactor, one endblock was fixed in space while the other endblock was sinusoidally moved at 10%

strain (1.25 mm) at 1 Hz. Displacements were applied using 50 equal time steps from 0% to 10% strain. Within the hydrogel, principle strains at each time point were calculated for post-processing analysis.

Following creation of the initial model, other geometries and stiffnesses were tested alongside the simple uniform described above. Laminates were simulated by creating two separate parts, each made of the same material, and connecting nodes of opposing faces to simulate lamination. Different laminate divisions were considered, including a flat line, a simple curve, an S-curve containing convex and concave sections, and an interlocking structure. To simulate lamination, constraints were applied to join opposing faces of each laminated section; however, lamination points were not specified with an elastic modulus that was different from the individual sections. Using a simple flat line laminate, the stiffness of one section was varied relative to the other, by a factor of 2, 5, 10, or 20, to observe the differences between mismatches in modulus. Maximum principal strain is reported as mean ± standard deviation of all gel elements.

4.2.2 Synthesis of OPF and PEG-DA

OPF was synthesized as previously reported (102). Briefly, poly(ethylene glycol) (Mn = 10,000 Da; Sigma–Aldrich) was azeotropically distilled and subsequently dissolved in distilled methylene chloride (Fisher) to produce a ~40% (v/v) solution. Distilled fumaryl chloride (FuCl, Sigma–Aldrich) and triethylamine (TEA; Sigma–Aldrich) in a molar ratio of 1 PEG:0.9 FuCl (2 TEA:1 FuCl) were slowly added dropwise to the PEG solution, and the reaction was held under nitrogen on ice. The OPF formulation was continuously stirred for 48–72 h at 25 °C under nitrogen to ensure

reaction completion. Next, excess methylene chloride was evaporated and the Cl–TEA salt was removed by filtration (Whatman). The OPF was recrystallized twice in ethyl acetate (Fisher) and washed three times in ethyl ether (Fisher). The resulting powder was vacuum dried at <5 mmHg and stored in a sealed container at -20 °C until further use.

PEG-DA was synthesized as previously reported (157). Briefly, 24 g PEG 3.4K (Sigma-Aldrich, St. Louis, MO) was dissolved in 60 mL distilled methylene chloride (MeCl; Fisher Scientific, Pittsburgh, PA), then reacted at a 2:1 molar ratio with acryloyl chloride (AcCl, added dropwise, Sigma-Aldrich) and at a 1:1 molar ratio with triethylamine (Sigma-Aldrich) to create a 40% (w/v) solution under nitrogen overnight. Workup was performed by reaction with 2M K_2CO_3 (Fisher) at a 2:1 AcCl molar ratio and separation into aqueous and organic phases. This was followed by drying the solution with anhydrous $MgSO_4$ (Fisher) and precipitating the polymer in ethyl ether (Fisher). Product was filtered, vacuum dried and frozen at -20ºC until use. OPF 10K was also synthesized as previously described (102). PEG 10K (Sigma-Aldrich) was distilled and dissolved in distilled MeCl to produce a 40% (v/v) solution. Distilled fumaryl chloride (FuCl; Sigma-Aldrich) and triethylamine (TEA; Sigma-Aldrich) at 1:0.9 PEG:FuCl and 2:1 TEA:FuCl molar ratios were added dropwise to the PEG solution and the reaction was conducted under nitrogen at 0ºC. The reaction was stirred for an additional 48-72h at 25ºC to ensure reaction completion, at which time excess MeCl was evaporated and TEA-Cl salt was removed. The resultant product was recrystallized twice in ethyl acetate (Fisher) and washed three times in ethyl ether, then filtered, vacuum dried and stored at -20ºC until use. PEG-DA (M_n 3770 ± 10, PI 1.1 ± 0.0), PEG 3.4K (M_n 3400 ± 30, PI 1.1 ± 0.0), OPF 10K (M_n 19,800 ± 100, PI 4.6 ± 0.1) and PEG 10K (MW 12,900 ± 200; PI

1.1 ± 0.0) were characterized via gel permeation chromatography as previously reported (109).

4.2.3 Mechanical testing of OPF:PEG-DA hydrogels

Constructs for tensile culture were fabricated using a 50:50 wt% mixture of OPF 10K and PEG-DA. Phosphate buffered saline (PBS) was added to fabricate a 90% wt water gel. Next, thermally activated free radical initiators ammonium persulfate (APS) and tetramethylethylenediamine (TEMED) were added to a final concentration of 0.018 M, and solutions were deposited into a Teflon mold, invading porous polyethylene endblocks as previously described (89). Constructs were polymerized at 37ºC for 10 min, then moved into excess PBS and allowed to swell overnight at room temperature.

Following swelling, constructs were mechanically evaluated by fitting metal rods through each endblock and mounting the construct on an ELF 3200 mechanical testing system (EnduraTEC/Bose) (Figure 4.2). Force was recorded using a 1 N load cell and data was recorded through computer-based data acquisition software (WinTest, EnduraTEC). Sample height, width and length were recorded using digital calipers and stress and strain were calculated from the force and displacement curves of each sample. To measure stress-strain curves at different strain rates, constructs ($n \geq 4$) were tested at 5 different rates at room temperature: 2.5%, 5%, 10%, 20% and 40% strain/sec. Gels were manually hydrated with PBS during loading. Average Young's modulus were compared using one-way ANOVA with Tukey's post-hoc HSD test.

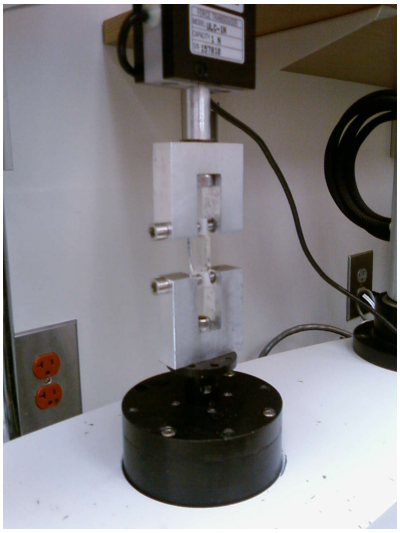

Figure 4.2. A tensile culture gel being tested in a mechanical testing system.

4.3 Results

4.3.1 Finite element modeling

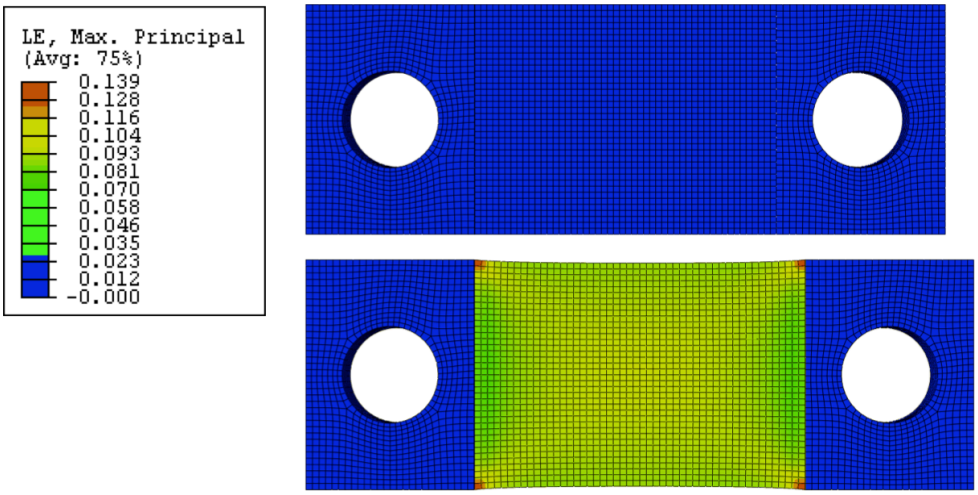

Figure 4.3. Strain field in hydrogel after 10% deformation.

False-color plots of maximum principal strains were created to depict the relative distribution for strain through the middle of the gel (Figure 4.3). At maximum displacement during cyclic loading, peak strains were located at the corners of the gel.

Lowest strains were observed where the gel interfaces with each endblock. Within the central region of the hydrogel (XY-plane), the maximum principal strains were uniform with little variation of strain. There was little variation in strain through the thickness of the construct (Z-direction). For 10% total displacement, the maximum principal strains ranged from 6.8%-13.9% (Figure 4.4). However, 88.8% of elements had a principal strain between 9% and 10.5%; the average strain was 9.58% ± 5.7%.

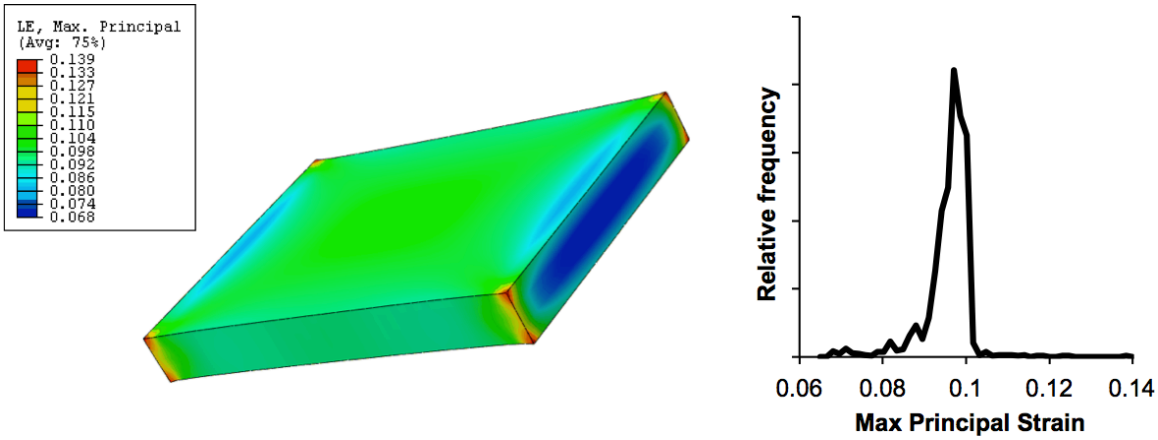

Figure 4.4. Distribution of principal strain in hydrogel. Left, three-dimensional distribution of strain in hydrogel with legend. Right, histogram of maximum principal strain across all elements in the hydrogel.

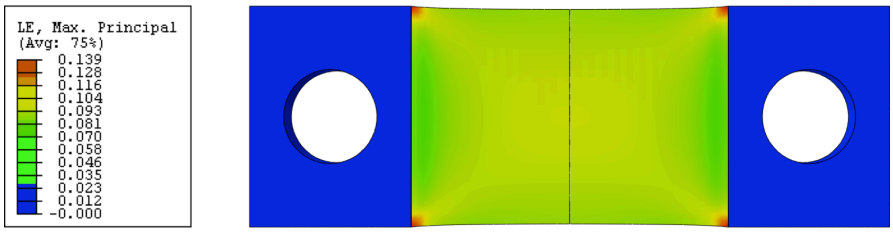

Figure 4.5. Distribution of strain in finite element model of laminated hydrogel.

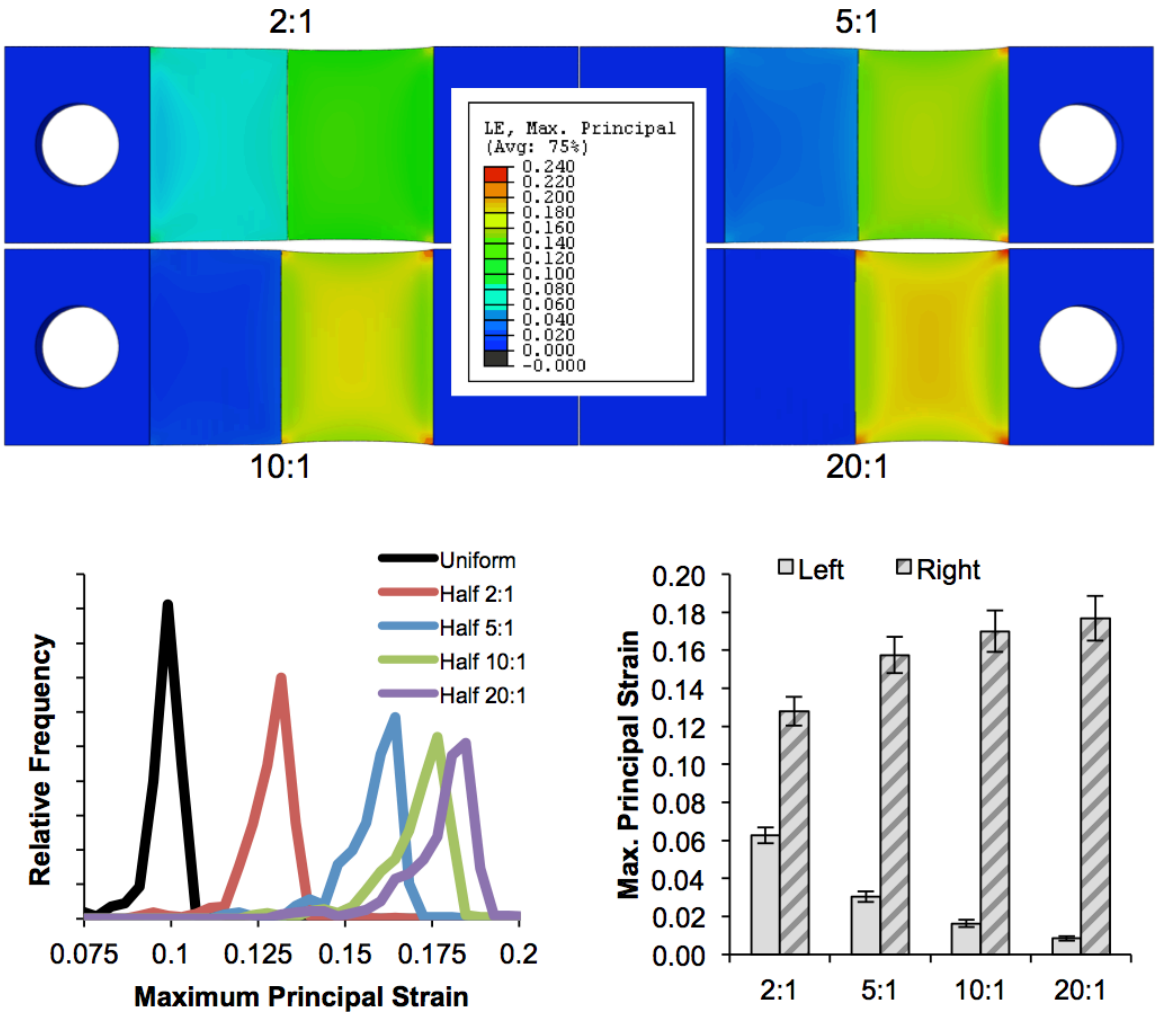

Figure 4.6. Differences in strain distribution between laminates with different relative stiffnesses. Above, distribution of strain in laminates with differences in stiffness between each side. Bottom left, histograms depicting the distribution of strain in the right gel section. Bottom right, average principle strain.

Changes in interface geometry did not affect the strains or strain distribution (Figure 4.5). However, by modifying the stiffness of a single section, changes were seen in the resulting strain profiles (Figure 4.6). By increasing the mismatch in stiffness between sections, magnitude-dependent changes in strain were detected throughout the gel. As long as the modulus ratio between the two sections was identical, changing stiffness did not change strain profiles (data not shown).

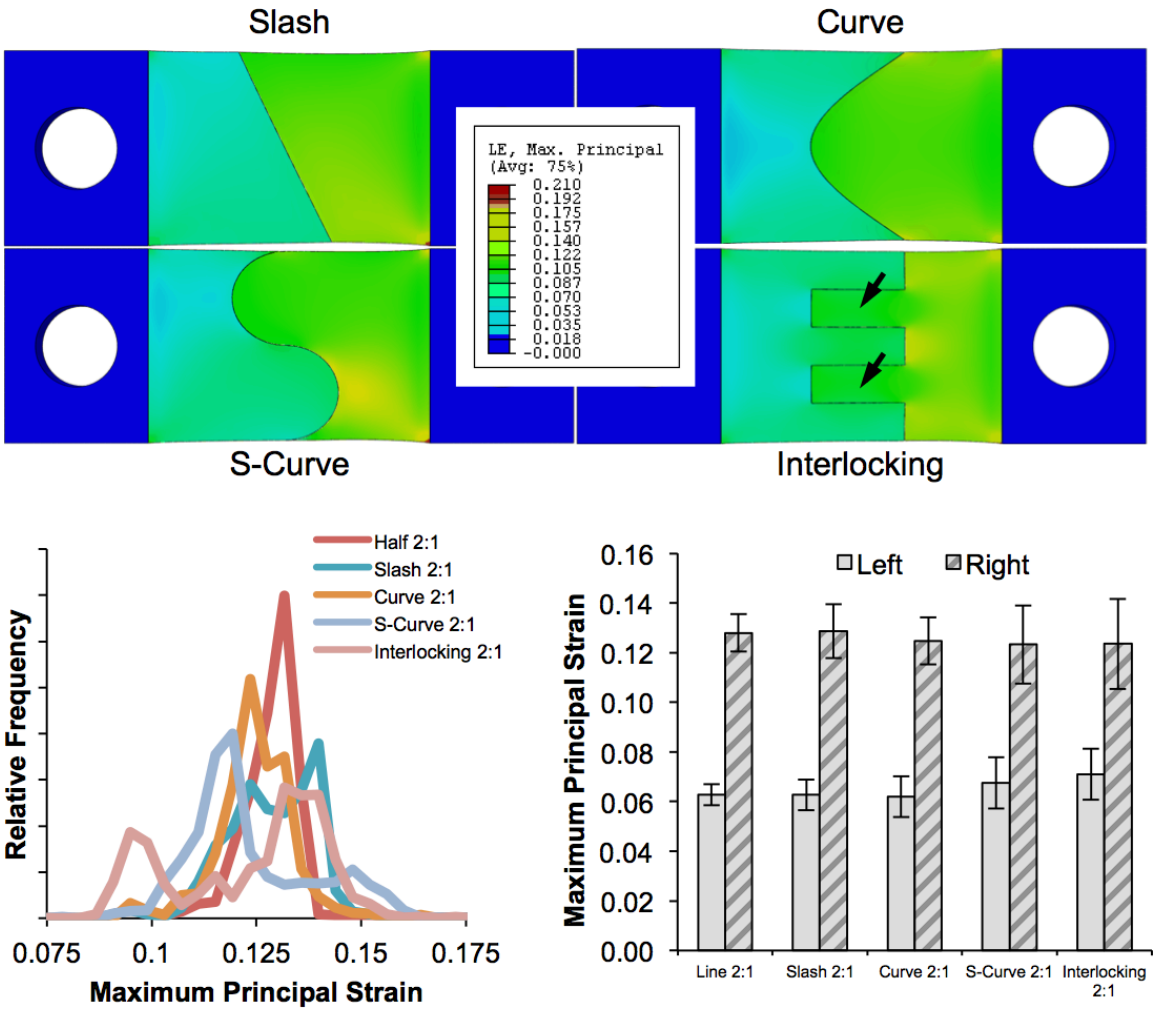

Figure 4.7. Differences in strain distribution between different laminates. Right laminate is half the modulus of the left laminate. Bottom left, histograms depicting the distribution of strain in the right gel section. Bottom right, average principle strain.

When combined with changes in stiffness, differences in interface geometry resulted in stress concentrations at the points of greatest difference in modulus (Figure 4.7). Strains in stiffer laminated sections (left sides) were noticeably lower, while sections with lower modulus (right sides) exhibited higher strains. The distribution of strain appeared to be correlated with the horizontal dimensions of the particular section;

in other words, areas of shorter horizontal width exhibited higher strains. With the interlocking laminate model, areas of higher modulus tended to shield areas of lower modulus (arrows). This was reflected in histogram data depicting the distribution of principal strains in the right gel sections of the various laminates (Figure 4.7, bottom left). Distribution of strain varied with interface geometry; any deviation from a flat line laminate widened the strain distribution. The interlocking laminate showed the most variation in strain due to shielding from the stiffer section, reducing the local principal strains in those areas. However, the average maximum principal strains were observed to be relatively similar (Figure 4.7, bottom right).

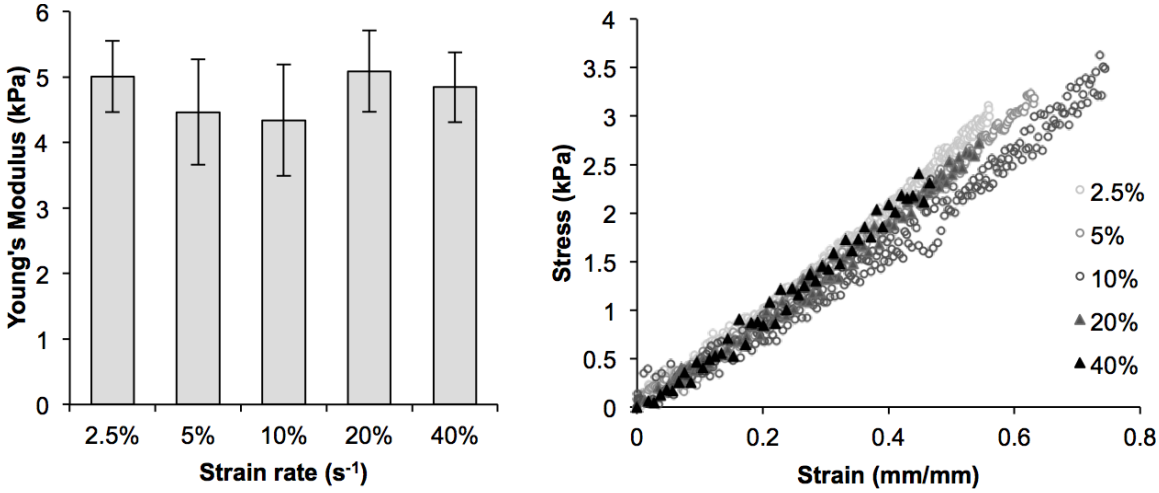

Figure 4.8. Young's modulus of OPF:PEG-DA tensile culture hydrogels strained at different rates. Left, average Young's modulus among the five strain rates tested (strain/sec). There were no statistical differences between any rates (n = 4-6 ± SD, p < 0.05). Right, representative stress-strain curves immediately prior to construct failure are shown for each strain rate tested.

4.3.2 Mechanical testing results

All constructs strained at different rates were measured to have a Young's modulus of ~5 kPa (Figure 4.8). Upon inspection after failure, gels were not noted to

have frequently broken at the interface between the endblocks and hydrogel material. There was no statistically significant difference between the Young's modulus calculated for any of the strain rates tested.

4.4 Discussion

In tissue engineering constructs that are composed of sections with varying geometries and mechanical properties, mechanical forces will induce varying strain fields across each section depending on differences in modulus and the particular geometries between each section. Even in a construct of uniform mechanical properties, however, particulars regarding geometry and the specific application of loading may prevent strain from being uniformly applied throughout the scaffold. Cells are responsive to their local mechanical environment in a magnitude-dependent manner, and mechanical forces have been shown as a putative factor in cell differentiation in a wide variety of orthopaedic tissue engineering contexts (65, 89, 220-222). Therefore, for studies involving tensile culture, such as those in Chapter 5, finite element modeling enabled the distribution of strain to be studied within various geometric configurations and variations in stiffness.

This work demonstrates that within a uniformly constructed scaffold with a high degree of symmetry and attention to minimizing contact forces within a tensile culture bioreactor, the majority of local principal strains remained between 9% and 10.5%, with approximately 5% standard deviation (Figure 4.4). This construct design (Figure 4.1, first explored in (178)) was devised to improve on a previous scaffold, where metal pegs contacted the gel directly via holes punched into the gel; direct contact led to a large disparity in local strains (218). Within this model, the attachment of the hydrogel region

to the much stiffer endblocks did lead to heterogeneity in local strains, as the corners tended to shield the middle edges from strain (Figure 4.4). However, heterogeneity in this model was greatly reduced when compared to the previous iteration of construct design (218). Drawing from the results of the model, heterogeneity appears difficult to eliminate in a system where components with relatively high stiffness directly interact with much softer hydrogels.

In this report, the lamination of interfaces did not alter the strain distribution (Figure 4.5). In reality, structures are laminated when, after the first structure has been polymerized, the second prepolymer solution is placed adjacent to the first. Although mixing can be rendered negligible (190), the prepolymer solution appears to diffuse into the first hydrogel to form a mechanical link (191, 210). This interpenetrating region may have increased mechanical properties due to increased crosslinking at the interface, but the resulting change in mechanical properties has never been measured. Knowledge of the dimensions and modulus of such a region would increase the accuracy of the model and provide additional insight into large differences in strain near the interface due to its likely higher modulus. As a first pass, characterization techniques that investigate micron-scale mechanical properties, such as nanoindentation or atomic force microscopy, could be employed to create a map of stiffness of the interface; such techniques have been previously used to characterize both hydrogels and tissues (86, 223-225). Alternatively, employing elastographic or similar particle-tracking techniques to map the interface during applied strain could be used in reverse, to build a model that approximates the distribution of strain in a laminated hydrogel (226). Profiling interfaces via surface mapping could provide relative differences in stiffness over the interface

region, providing a first approximation of changes in stiffness relative to its two adjoining layers.

Changes in modulus between laminated gel sections were shown to have altered the local strain fields in both sections (Figure 4.7). If laminates contained different material compositions or were seeded with different types of cells, laminates could also change in stiffness over time. In one example, a collagen scaffold with a gradient of immobilized Runx2 retrovirus was used to osteogenically differentiate rat fibroblasts; differences in mechanical properties were noted after 6 weeks in culture (6). Other studies have generated gradients of increasing modulus in a single PEG scaffold (174, 227). Applied cyclic tensile strain to these constructs would induce heterogeneous strain fields, but with encapsulated cells degrading the biomaterial and/or depositing ECM, local strain fields could change over time. Additionally, if heterogeneities are designed, mechanical forces could be used to spatially target differentiation depending on local strain fields. The results of these models indicate that strain fields should be modeled prior to application of strain to actual constructs, to provide detailed profiles of the local strain environment. Moreover, constructs may require monitoring and mechanical characterization over time (e.g., the aforementioned AFM or particle tracking-based imaging techniques) to clarify the evolution of changes in mechanical properties as cells remodel their microenvironment. This information would provide a time profile of local strain distribution to elucidate possible temporal effects of applied macroscopic strain.

The use of different interfaces modified the distribution of strain experienced by the softer laminate (Figure 4.8). It was shown that the use of an interlocking laminate, with areas that were shielded by the stiffer section, created apparent areas of higher and

lower local strains. The use of other types of laminates also created similar differences in the distribution of strain. Although average strains did not appear to vary, different levels of strain, as noted in the interlocking design, could cause dose dependent reactions in encapsulated cells as reported previously (212, 213). Further design could reveal optimal interfaces to encourage limited or increased heterogeneity, to control the localization of applied strain to desired areas. For example, scaffolds could be designed to target strain-linked fibroblastic differentiation in one portion, and minimized in another section, using control of interfaces and mechanical properties.

To further increase the accuracy of the model, other data regarding the failure of these gels could be experimentally determined. For example, ultimate tensile strength was not measured for gels used in this system; thus, materials in this finite element model would continue to deform without failure, whereas OPF/PEG-DA constructs failed in mechanical testing. Anecdotally, OPF/PEG-DA hydrogels required applied strains well beyond 10% (the magnitude of strain applied in Chapter 5) to fail (Figure 4.8). However, premature failure would prevent certain magnitudes of strain from being applied in hydrogel constructs that are more brittle. Failure in response to stress risers and low ultimate tensile strength would therefore be important to characterize to improve the fidelity of the model.

Another assumption in the model was the modeling of the hydrogel as an ideal elastic material. Hydrogels are known to behave similarly to rubbers (228), in which the viscous component is functionally negligible. Within the range of strain rates tested, OPF:PEG-DA hydrogels did not appear to exhibit strain-rate dependent behavior in the form of different Young's modulus (Figure 4.8). Were the viscous component of these

hydrogels a significant factor, increased strain rate would, generally speaking, translate to an increased measured Young's modulus. However, the method used in this study did not thoroughly characterize the viscoelastic properties of these hydrogels; other analyses (e.g., dynamic mechanical analysis and rheological measurements) would provide the storage and loss moduli (G' and G"), as well as the phase angle δ (228). This analysis has been performed in PEG gels in two previous studies (167, 169). In both studies, PEG gels were found to have G" values that were two orders of magnitude less than measured values of G'. When compared to collagen gels, collagen G" values were less than an order of magnitude relative to G', and $\delta_{collagen}$ = 17.7º compared to δ_{PEG} = 2.3º (167). It was posited that the difference in crosslinking (physical crosslinking in collagen versus covalent crosslinking in PEG) translated to functionally viscoelastic versus ideal elastic behavior. Given this previous work, and the first pass characterization of gels in this study, the assumption of ideal elasticity is reasonable for the finite element models presented here. However, refining the accuracy of the model may require a more detailed characterization of G' and G" for the hydrogels used in this system.

Finally, another possibly important consideration in this model that was ignored was the consideration of poroelasticity in the finite element model. As the hydrogel materials tested are fundamentally poroelastic due to their initial water weight (90%) and subsequent uptake of water during swelling, the effects of tensile strain could affect fluid flow through the construct (218). The effects of fluid flow and its resultant shear stress have been modeled in native tendon tissues to have significant effects on MMP-13 expression in rat tail tendons (217). In particular, cell response was shown to be sensitive to strain rate as well as amplitude. Thus, modeling possible hydrostatic pressures and

fluid velocities resulting from a variety of tensile strain regimens would provide additional insight into additional mechanically-driven effects that would affect cells encapsulated within a porous, synthetic construct.

Finite element models have been employed to study information regarding the distribution of strains in other hydrogel systems as well as in actual tissues. A finite element model of a proteolytically-degradable PEG hydrogel undergoing applied strain showed a similar distribution of strains within the construct; however, different boundary conditions for the model prevent direct comparison (229). Other finite element models of materials undergoing cyclic loading have provided additional insight into other aspects of biomaterial constructs; for example, a finite element was employed to investigate the effect of cyclic loading on fluid flow and solute transport within a poroelastic structure (230). With regards to tendon tissues, the aforementioned model of fluid flow in tendon tissue provided information regarding the effects of fluid-induced shear stress on cell response to loading within a transversely isotropic environment (217). Another study investigated the application of biaxial strain on local strain distribution in the meniscus, which is spatially heterogeneous and contains significant anisotropy due to its biochemical composition (18, 231). Although PEG-based gels are not intrinsically anisotropic (167), anisotropy in mechanical properties would introduce another form of heterogeneity within biomaterial constructs. Adding additional parameters based on these studies, then, would further refine the model and greatly expand its utility.

4.5 Conclusions

This study represents a first attempt at characterizing the effects of applied strain

on local strain distribution within homogeneous and heterogeneous constructs, using an existing tensile culture bioreactor as a base for a finite element model of the forces applied to a biomaterial scaffold. Results indicate that manipulation of differences in modulus and interface geometry can indeed modulate variations in local strain distribution. In using complex tissue engineering constructs with multiple designed heterogeneities present within a single biomaterial scaffold, applying strain can therefore be used to spatially target changes in strain-dependent differentiation depending on geometry and modulus variation within a material. Further characterization of the poroelastic and viscoelastic properties of these hydrogels, as well as the dimensions and modulus of the lamination interface, would provide improved information and increase the relevance of the model for describing possible changes in local strain fields experienced by cells.

CHAPTER 5

MANIPULATION OF DEGRADABILITY IN PEG-BASED HYDROGELS ELICITS CHANGES IN MESENCHYMAL STEM CELL MORPHOLOGY AND LIMITED EFFECTS ON TENDON/LIGAMENT FIBROBLAST-RELATED MARKERS UNDER CYCLIC TENSILE STRAIN

5.1 Introduction

It has been estimated that at least 200,000 people in the United States receive treatment for injuries to tendon or ligament tissue each year (2). In response, a multitude of tissue engineering approaches have been employed to engineer replacement fibrous tissues, many of which include scaffold materials such as PLLA, silk and collagen type I (18). Typically, either tendon/ligament fibroblasts or multipotent mesenchymal stem cells (MSCs) have been explored as cell sources for these constructs (232, 233). However, MSCs offer an advantage in that they can be easily isolated and expanded to sufficient numbers for therapeutic use (17). For those utilizing MSCs as a cell source, a number of approaches employing culture under tensile strain to induce differentiation toward a fibroblastic lineage have been investigated (9, 59, 89, 181). However, more information is needed to clarify the role that the biomaterial scaffold may play in affecting MSCs' response to external loading during the pre-culture (differentiation) period in order to optimize pre-culture conditions for maximal cell differentiation.

In response, our laboratory has designed a well-controlled model system to better understand how changing the degradability of the extracellular environment will affect changes in cell morphology and subsequent differentiation under tensile loading. Previous studies have shown that, in addition to tensile strain, the local extracellular

environment, including stiffness and geometry (173), can affect cell fate. The regulation of cell shape and area has been implicated in driving MSC differentiation into either osteoblast or adipocyte lineages (171, 172). For chondrogenic differentiation, a rounded shape has been shown to be highly linked with gene upregulation indicative of chondrogenesis (234, 235). In engineering tendon/ligament tissues, changes in cell shape have been shown to affect collagen I and collagen III expression in anterior cruciate ligament cells seeded on blends of PCL/chitosan (236). However, by using a primarily synthetic biomaterial with targeted degradation sites, such as that employed in this study, the local extracellular environment can be precisely tailored to enable cell spreading in a highly controlled manner, facilitating examination of the interplay between cell shape and response to tensile strain.

In order to create this model system, poly(ethylene glycol) (PEG)-based synthetic hydrogels were chosen due to their cytocompatibility and the relative ease of tailoring these systems with specific functionalities (10). Our laboratory has previously utilized PEG-based hydrogels to direct differentiation of MSCs towards a tendon/ligament fibroblast phenotype (89). To engineer cell-mediated degradation in these synthetic scaffolds, matrix metalloproteinase (MMP)-sensitive sequences were integrated into the hydrogel (133, 140). MMPs are a family of endopeptidases that degrade extracellular matrix (ECM) components. These may be secreted by MSCs to cleave surrounding ECM and enable cell-initiated spreading, migration and matrix deposition (10, 237).

Several MMP-cleavable sequences have been previously incorporated in PEG-based hydrogels, originally including LGPA, derived from the collagen I α1(I) peptide chain, and more recently, VPMSMRGG, derived from a combinatorial approach using a

completely randomized dodecapeptide library and demonstrating enhanced susceptibility to MMP-1 and MMP-2 (133, 135, 139, 140). Using peptides with comparatively slow or fast cleavage kinetics allows the possibility of selectively manipulating cell morphology by altering the degradation rate of the surrounding matrix. Therefore, the objective of these studies was to characterize cell morphology in fast- and slow-degrading MMP-cleavable hydrogels, as well as examine the effects of the degradability of the surrounding hydrogel on MSC response to cyclic tensile strain in a custom-designed tensile culture bioreactor.

5.2 Methods

5.2.1 PEG-peptide polymer synthesis

MMP-sensitive PEG products were synthesized according to published protocols (238). Slow-degrading (GGGLGPAGGK) and fast-degrading (GGVPMSMRGGGK) peptide sequences (Aapptec) were dissolved in 50 mM sodium bicarbonate buffer at pH 8.5. Acrl-PEG-succinimidyl valerate (Acrl-PEG-SVA; M_n ~3400; Laysan Bio) was added at a ratio of 1:2.2 peptide:Acrl-PEG-SVA. After reacting for 3 hours with gentle stirring, the mixed solution was transferred into 3500-5000 Da molecular weight cutoff dialysis tubing (Spectrum Labs) and dialyzed for 2 days to remove unreacted reagents. Similarly, GRGDS (PeproTech) was conjugated to Acrl-PEG-SVA as above, and dialyzed against 1000 Da molecular weight cutoff tubing (Spectrum Labs). All three products, Acrl-PEG-GGGLGPAGGK-PEG-Acrl, Acrl-PEG-GGVPMSMRGGGK-PEG-Acrl and Acrl-PEG-GRGDS, were lyophilized (Labconco) and stored at -20ºC.

5.2.2 Cell culture

Human MSCs were obtained from the Texas A&M Health Science Center College of Medicine Institute for Regenerative Medicine at Scott & White at passage 1. Following cell expansion for studies, cells (passage 2) were seeded in triple flasks (Nunc) at 50 cells/cm^2 following recommended protocols. The growth medium used was α-MEM with 16.3% fetal bovine serum (FBS, Atlanta Biologicals), 1% antibiotic/antimycotic (Mediatech), and 4 mM L-glutamine (Mediatech). (Note: The fetal bovine serum lot used was pre-screened for MSC growth while maintaining collagen I, collagen III and tenascin-C gene expression.) Following expansion, cells were frozen at passage 2 in liquid nitrogen until further use. For these studies, cells from three separate donors were thawed, expanded separately, and combined prior to encapsulation at passage 3.

5.2.3 Cell encapsulation and tensile culture

Both slow-degrading and fast-degrading PEG were used to encapsulate cells as follows. 1 μmol Acrl-PEG-GRGDS/(g swollen hydrogel) was added to each polymer type to enable cell adhesion. Polymer was dissolved in phosphate buffered saline (PBS) to create a 90 wt% water solution, then sterile filtered using a 0.2 μm glass prefilter (Nalgene). 0.07 wt% Irgacure 2959 (D2959; Ciba) in PBS/dimethyl sulfoxide was added to enable photopolymerization using UV light. Next, hMSCs were added at a final concentration of 10 x 10^6 cells/mL, and the hydrogel solution was deposited into Teflon molds, integrate with porous polyethylene endblocks as previously described to form gels 12.5 x 9.5 mm x 1.6 mm (89). Following 10 minutes of exposure to UV light (10.5 mW/cm^2; 365 nm; UVP), tensile constructs were placed into 6-well plates containing α-

MEM with 10% FBS, 1% antibiotic/antimycotic (Mediatech), 4 mM L-glutamine (Mediatech), and 50 μg/mL ascorbic acid (Sigma). Constructs were allowed to swell overnight to reach equilibrium swelling prior to culture.

Swollen fast-degrading and slow-degrading constructs with encapsulated MSCs were loaded into the tensile culture bioreactor and a loading regimen was applied for the duration of the experiment as reported previously (89). Specifically, constructs were maintained using 10% sinusoidal cyclic strain (5% offset, 5% amplitude) at 1 Hz for 3 h, followed by 3 h at 0% strain. Control hydrogels, both fast-degrading and slow-degrading constructs, were placed into a similar culture system and held at 0% strain. Culture medium was replaced every 2-3 days.

5.2.4 Cell viability, confocal imaging, image processing and particle analysis

At 1, 7 and 14 days, constructs (n=3) were removed from the bioreactor and incubated in LIVE/DEAD fluorescent staining solution (1 μM calcein AM and 1 μM ethidium homodimer-1 in PBS; Invitrogen) for 1h, then imaged in PBS on a confocal microscope (Zeiss LSM 510). Images were taken every 10 μm through the entire thickness of the gel from three separate regions in each sample.

Image files were processed using ImageJ 1.45h (http://imagej.nih.gov/). For circularity analysis, each image stack was smoothed using ImageJ's nearest neighbor function, and the green channel was isolated and thresholded using a cutoff of 60 (out of 255; threshold arbitrarily set). For each image, a particle analysis was performed to identify particles greater than 60 square pixels, and area (in μm^2), circularity, and a best fit ellipse was calculated for each particle in each image slice. Circularity is defined as

$4\pi A/P^2$, where A and P are the area and perimeter of the particle. A perfect circle would have a circularity of 1; circularity decreases towards 0 in more elongated (spread) cells. To prevent cells on the surface of the gel from being considered, and to prevent single particles from being counted multiple times, 5 images 50 μm apart, 200 μm from either edge were isolated from each stack. This was performed in an automated fashion by automatically calculating a best fit line in MATLAB (MathWorks) using a least squares regression and the average circularity of each slice within a stack. The five images were selected based on the best fit line having a near-flat slope and a high goodness of fit. Particles were combined from multiple stacks (≥3 stacks per gel). To calculate particle alignment, the angle of the major axis of each best-fit ellipse was calculated relative to the x-axis of the image; 90º describes a particle oriented perpendicular to the x-axis. Histograms describing the distributions of particle circularity and angle were normalized to the total number of particles in each sample (relative frequency) before plotting, so that the area under each curve is 1.

5.2.5 Cell number

At 1, 7 and 14 days after culture, constructs were removed from the tensile culture bioreactor and the wet weight of the hydrogel was measured. Gels were mechanically disrupted using a pellet grinder (VWR International) and 500 μL distilled deionized water was added. To release DNA from encapsulated cells, samples were subjected to three repetitions of freeze-thaw cycles followed by sonication (Ultrasonik 28X, NEY). DNA content, representative of cell number, was determined by assaying the supernatant with PicoGreen reagents and included DNA standards (Invitrogen). Results were

normalized against the hydrogel wet weight.

5.2.6 Gene expression

At 1, 7, and 14 days after culture, constructs were removed from the tensile culture bioreactor, allowed to rest in culture medium for 2h, and processed using a pellet grinder as previously described. RNA was isolated from the disrupted hydrogels using QIAshredder columns (Qiagen), and RNA was purified using an RNeasy mini kit (Qiagen). To create cDNA, cDNA was synthesized using SuperScript III reverse transcriptase (Invitrogen) and nucleotide mix (Promega). Real-time polymerase chain reaction (PCR) was performed using custom designed primers, SYBR Green (Applied Biosystems), and a StepOnePlus™ Real-Time PCR System (Applied Biosystems). To analyze PCR amplification data, the raw fluorescence data was processed using LinRegPCR (v12.11; http://www.hartfaalcentrum.nl (239)). Genes examined included collagen I, collagen III, and tenascin-C as markers for tendon/ligament fibroblast gene expression (9). Starting concentrations of each target gene were normalized to a geometric mean of three housekeeping genes – glyceraldehyde phosphate dehydrogenase, β-actin, and 18S ribosomal RNA (240). Scleraxis, a transcription factor expressed in tendon progenitor cells, was also examined via PCR (65, 241). Finally, MyoD, a marker for myofibroblast differentiation, was also evaluated (65, 241, 242). Sequences for the forward and reverse primers used are listed in Table 5.1.

Table 5.1. Forward and reverse primers used in RT-PCR.

Gene	Forward primer	Reverse primer
Collagen I	gaaaacatcccagccaagaa	gccagtctcctcatccatgt
Collagen III	tacggcaatcctgaacttcc	gtgtgtttcgtgcaaccatc
Tenascin-C	ccacaatggcagatccttct	gttaacgccctgactgtggt
Scleraxis	gcgcgagcgagaccgcaccaaca	cccgccagcagcacgttgccc
MyoD	gtcgagcctagactgcctgt	gtatatcgggttggggttcg
GAPDH	gagtcaacggatttggtcgt	ttgattttggagggatctcg
18S rRNA	cgatgggcggcggaaaatagcctttgc	cagtggtcttggtgtgctggcctcgg
β actin	gcagtcggttggagcgagcatcccc	tcccctgtgtggacttgggagaggac

5.2.7 Histology and immunohistochemistry

At 1 and 14 days, samples were removed from the tensile culture bioreactor and placed into a solution of 5% sucrose in PBS under vacuum. Over 2 h, the concentration was increased to 15% sucrose. Next, over 4 h, gels were subjected to increasing concentrations of 20% sucrose:OCT (VWR) to achieve a 1:2 20% sucrose in PBS:OCT solution. After vacuum infiltration overnight, samples were gently frozen in liquid nitrogen and stored at -80ºC. Infiltrated hydrogels were cryosectioned at 20 μm. Sections were fixed in acetone, blocked with 0.3% hydrogen peroxide in methanol, then blocked with 1% BSA solution with 2% goat serum and 0.1% Triton X-100. For primary antibody binding, sections were incubated overnight in mouse anti-human collagen I, collagen III, or tenascin-C (Abcam). Sections were then incubated for 30 min with goat polyclonal biotin-conjugated anti-mouse immunoglobulin G (Abcam), followed by signal amplification using an avidin-conjugated horseradish peroxidase as part of a Vectastain Elite ABC kit (Vector Laboratories). Finally, sections were exposed to diaminobenzidine chromogen (Abcam) for 4 min to generate color change. Negative controls were stained as described, but with the primary antibody omitted.

5.2.8 Statistics

Results are reported as mean ± standard deviation. For statistical analysis, particle analysis and PCR amplification data for each gene were first transformed using a Box-Cox transformation (243). A three-factor ANOVA with Tukey's post hoc multiple comparison test was used to determine statistical significance with $p \leq 0.05$ to indicate significance between individual samples. For circularity, cell number, and gene expression analysis, the factors were day, strain condition, and gel type. To analyze angle distribution in individual gels, chi-squared goodness of fit tests (compared to a uniform distribution) were conducted, with $p \leq 0.05$ indicating significantly different than a uniform distribution.

5.3 Results

5.3.1 Confocal microscopy and image analysis

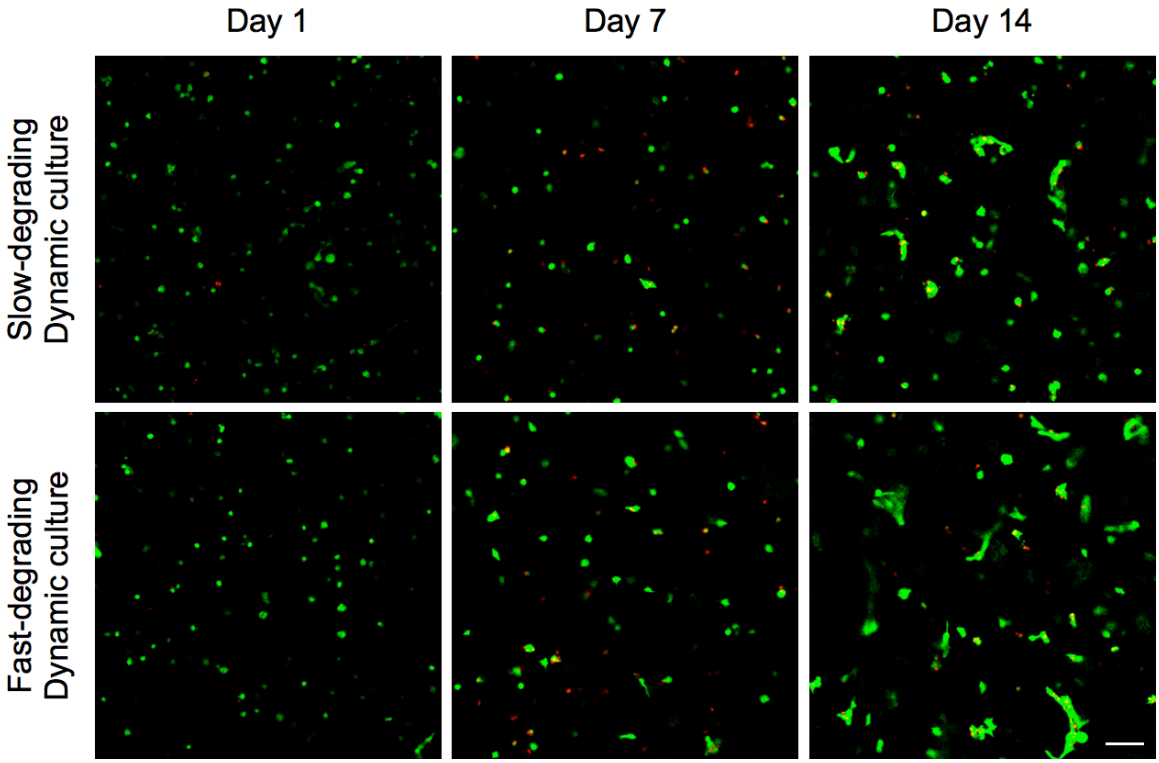

Figure 5.1. LIVE/DEAD images of encapsulated hMSCs (n=3) at 1, 7, and 14 days, cultured dynamically. (Images taken from gels cultured statically appeared similar to images from dynamically cultured gels.) Scale bar: 100 µm.

As indicated by green staining visible in confocal microscopy, MSCs remained viable in both slow- and fast-degrading hydrogels, cultured statically or dynamically, through 14 days of culture (Figure 5.1). At day 1, MSCs were not visibly spreading in any gel type or strain condition, and this continued through day 7. However, at day 14, a certain amount of spreading was visually evident in all gels. No difference was seen between dynamically and statically cultured gels. Additionally, cell alignment was not visually apparent.

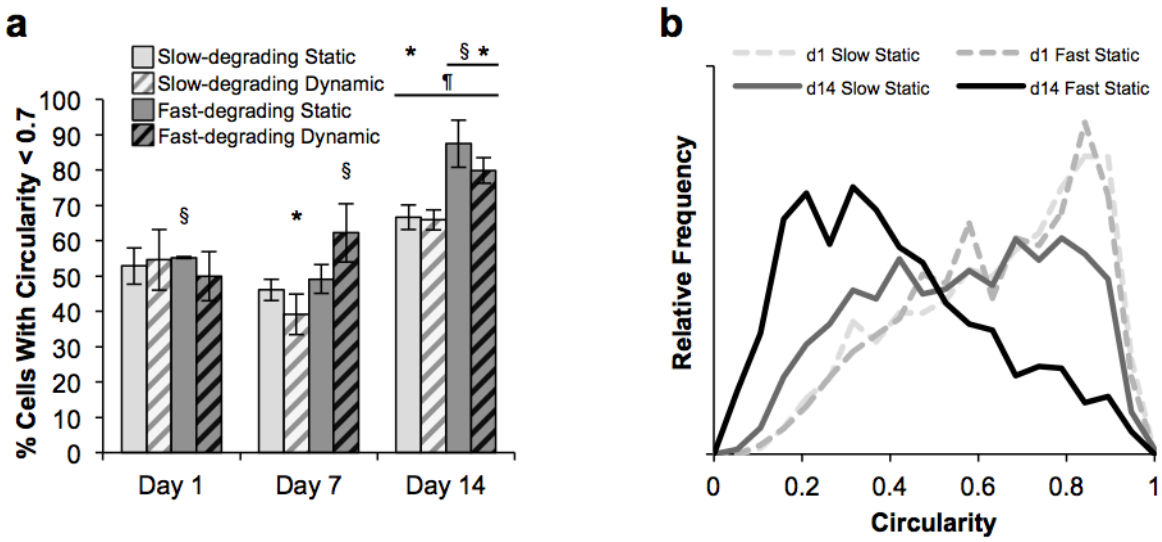

Figure 5.2. a) Percentage of cells below circularity of 0.7 in each gel type and culture condition at 1, 7, and 14 days. b) Histograms of cell circularity distribution in representative statically cultured samples; curves are normalized so the area underneath each curve is 1. * represents significance versus the same sample type on day 1; ¶ versus the same sample type on day 7; § versus the other gel type at the same time point (n = 3, $p \leq 0.05$).

To differentiate between "spread" and "unspread" cells for particle analysis, a circularity <0.7 was chosen to represent "spread" cells, based on average circularity values among all groups at day 1 (data not shown). Corroborating with confocal microscopy images, few significant differences in the percentage of spread cells were found between day 1 and day 7 (Figure 5.2a). Static fast-degrading gels on day 1 and dynamic fast-degrading gels on day 7 had more spread cells than slow-degrading groups. However, more cells were spread in fast-degrading gels at day 14, regardless of strain condition. Staining for F-actin using AF546-phalloidin demonstrated qualitative changes in the nature of actin organization in fast-degrading, statically cultured gels compared to slow-degrading, statically cultured gels at day 14 (Appendix Figure B.1). Almost all day 14 samples also had a higher percentage of spread cells than their day 1 and day 7 counterparts. To closely examine the differences between circularity distributions,

histograms of circularity values were also calculated (Figure 5.2b). At day 1, the majority of cells trended towards a highly circular shape (circularity of 1). At day 14, more cells in slow-degrading gels had lower circularities; however, the trend of cells in fast-degrading gels towards low circularity was much more dramatic. No differences were visually noted in circularity distribution between static and dynamic gels.

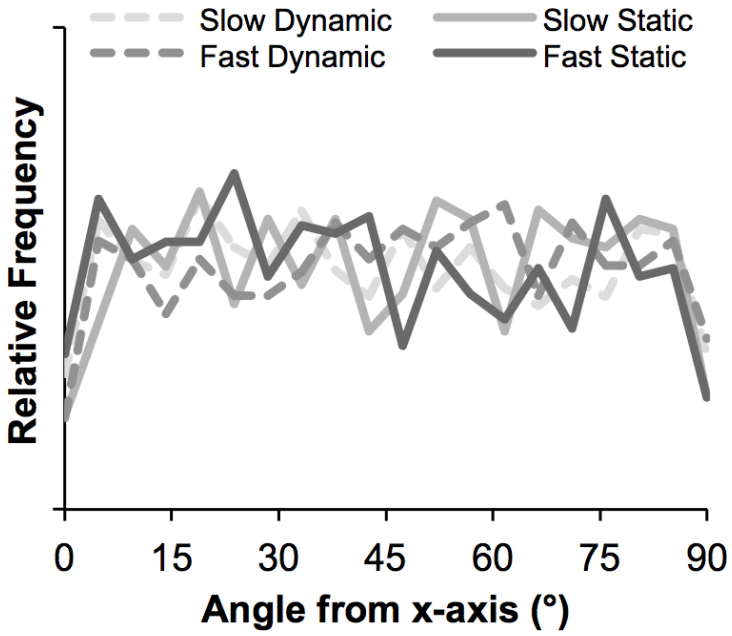

Figure 5.3. Histogram of particle alignment with x-axis from representative image stacks taken at day 14, normalized to total number of particles in each sample so the area under each curve is 1; 90° represents oriented perpendicular to the x-axis.

Finally, particle alignment data was collected to determine whether cells had oriented in the direction of strain. There was no difference in average angle between any sample group at any time point (data not shown). Angle distributions were plotted (Figure 5.3). Visually, there were no notable differences in distribution between gel type, strain condition, or time. To qualitatively determine if angle distributions in individual gels were non-uniform, chi-squared goodness of fit tests were used to compare each gel's

angle distribution against a uniform distribution (n=3 for each gel group). Gels that demonstrated significant differences were scattered across dynamically and statically strained gels, slow-degrading and fast-degrading gels, and time points, with no more than one gel per sample type exhibiting a significant difference in distribution.

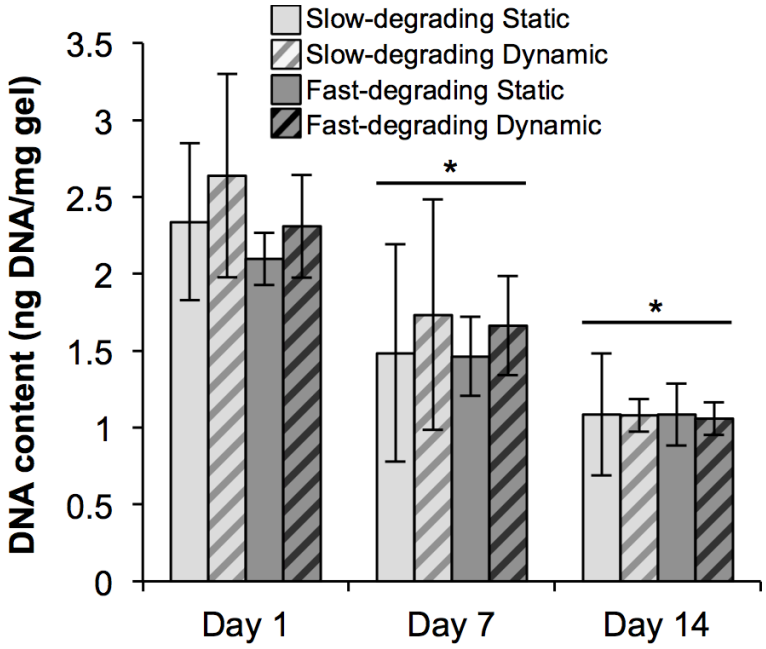

Figure 5.4. PicoGreen data from encapsulated hMSCs (n≥5), cultured statically or dynamically, at days 1, 7, and 14. Data are normalized to gel wet weight. * represents significance versus the same sample type at day 1 ($p < 0.05$).

5.3.2 Cell number

DNA content/gel wet weight (indicative of cell number per gel) did not change between any group at each time point (Figure 5.4). However, all groups at day 14 and day 7 were significantly lower than day 1 groups, indicating a decrease in DNA content (and therefore cell number) over time.

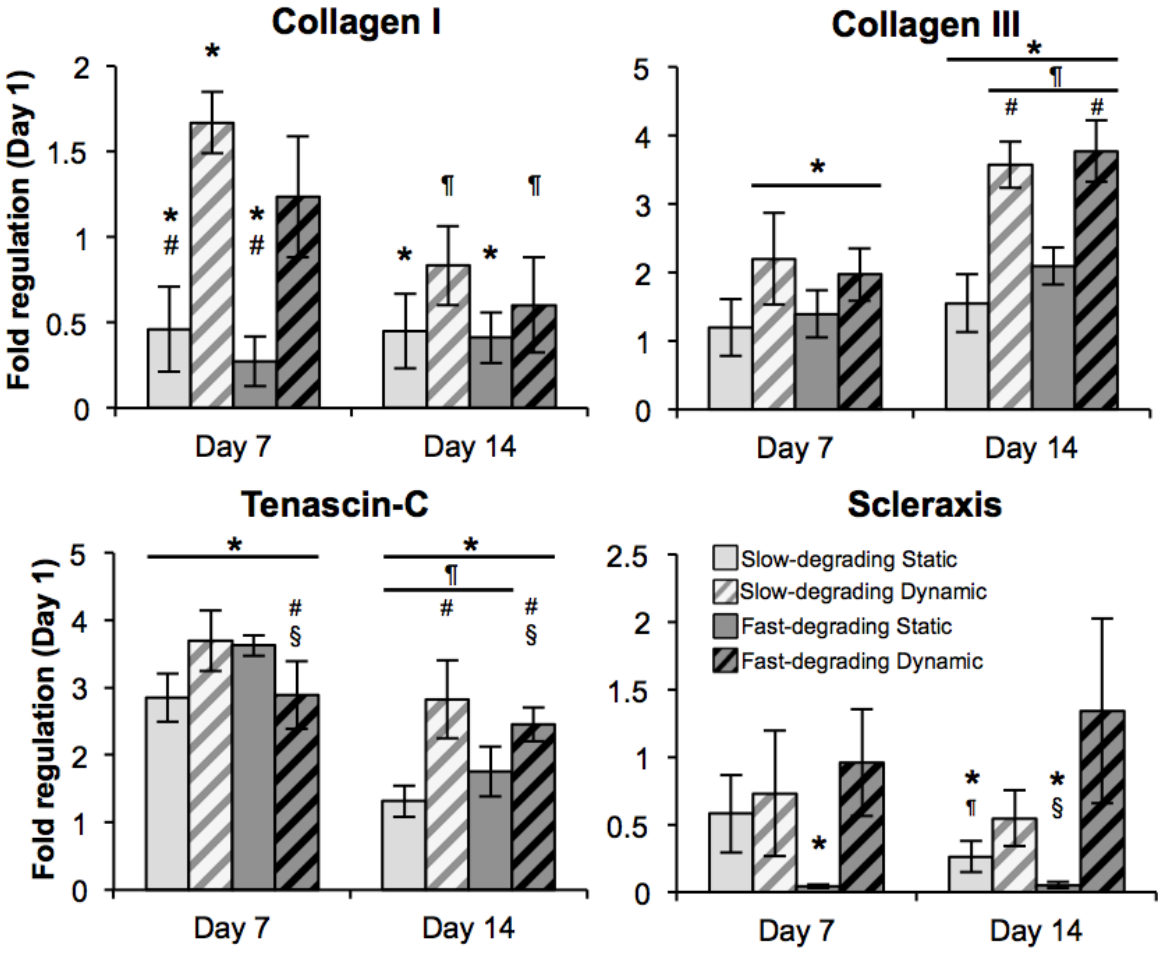

Figure 5.5. RT-PCR data of encapsulated hMSCs (n≥5), cultured statically or dynamically, at days 1, 7, and 14. Data are normalized to their respective day 1 groups. * represents significance versus the same sample type at day 1; ¶ versus the same sample type at day 7; # versus the other strain condition at the same time point; § versus the other gel type at the same time point ($p < 0.05$).

5.3.3 Gene expression

Scleraxis was maintained or downregulated over 14 days; static samples were downregulated at 14 days relative to day 1 samples, while dynamic samples were not different from day 1 (Figure 5.5). MyoD amplified late (average cycle number 39.3) and data was noisy (not shown). Overall, collagen I mRNA expression was downregulated over time; samples at day 14 were significantly lower than either day 1 or day 7 samples.

Statically cultured samples at day 7 were also significantly lower than day 1 samples and their dynamically cultured counterparts.

In contrast, collagen III was upregulated in most sample types at 7 days relative to day 1 samples, and all day 14 samples except the slow-degrading, static group were upregulated relative to their day 7 equivalents. In particular, there were significantly higher expression levels of collagen III in dynamically strained groups than statically cultured samples at day 14, regardless of gel type. Tenascin-C expression levels at day 7 were significantly upregulated in all groups relative to day 1 samples; however, all day 14 samples except the fast-degrading dynamic group were downregulated relative to day 7. Nevertheless, all day 14 samples remained significantly upregulated relative to day 1 samples, and there were also significant differences noted between hydrogel type for each culture condition (static and dynamic). However, fast-degrading, dynamic samples at days 7 and 14 showed significantly lower tenascin-C expression relative to their slow-degrading counterparts.

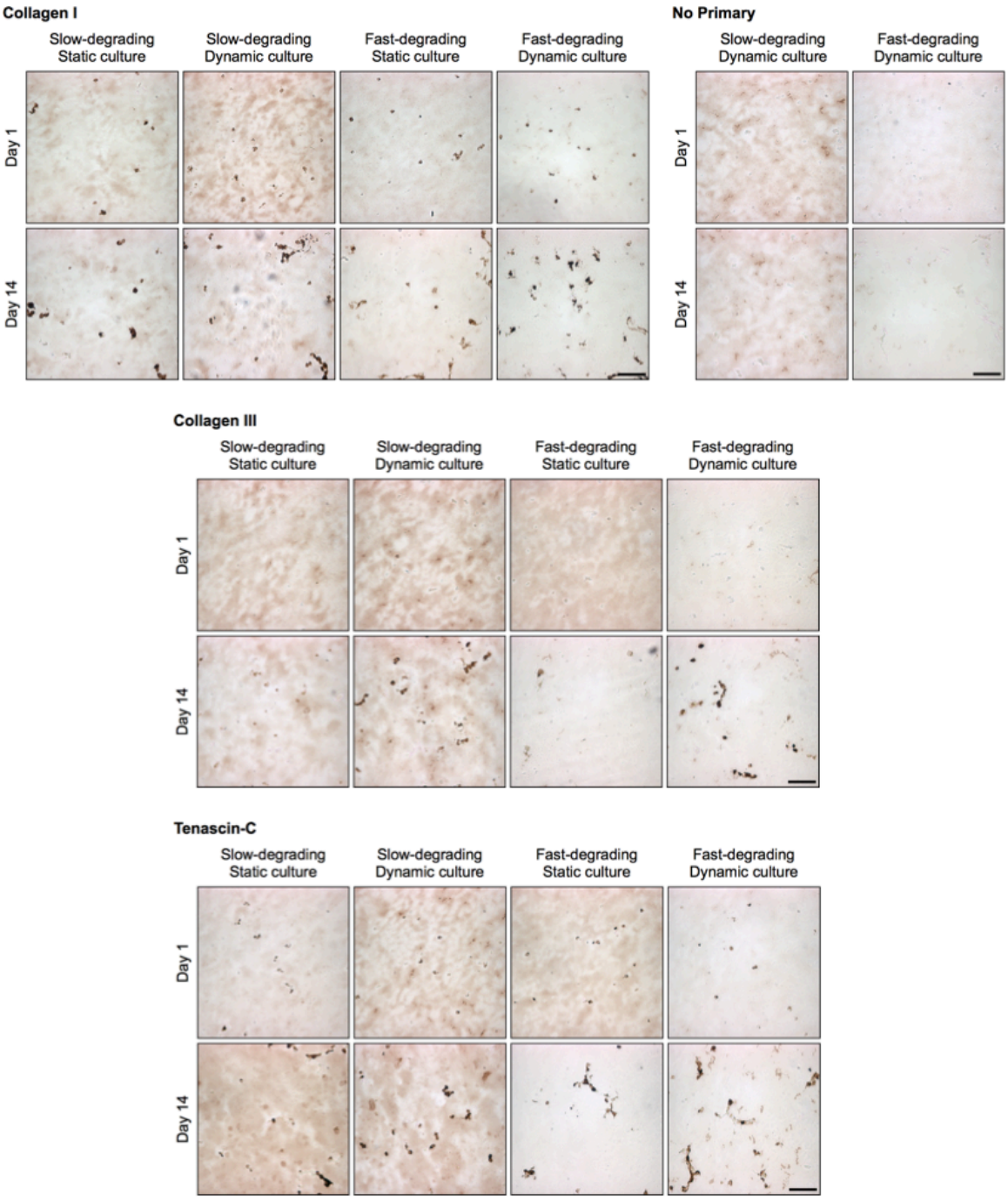

Figure 5.6. Histology of collagen I, collagen III and tenascin-C of MSCs encapsulated in both slow- and fast-degrading hydrogels (n=2). Scale bar 100 µm.

5.3.4 Histology

At day 14, all samples showed changes in cell morphology reflective of qualitatively increased spreading noted in Figures 5.1 and 5.2 (Figure 5.6). Immunohistochemistry revealed the presence of collagen I in all samples at day 1, with apparent increases in cell-associated deposition at day 14. The presence of collagen I did not appear to be different between static and dynamic samples. Cell-associated collagen III deposition was observed only at day 14, with more apparent staining in dynamically strained samples. Tenascin-C staining was seen at day 1 and continued through day 14; dynamically strained constructs seemed to show more prevalent staining overall. No cell-associated staining was observed in control sections that were not stained with primary antibody; however, some background staining was evident, especially in slow-degrading gels.

5.4 Discussion

In these experiments, hydrogels were fabricated using two established MMP-cleavable peptides with different MMP sensitivities and used to examine how degradability of the surrounding matrix affects MSC response to tensile strain (133, 140). Fabricated gels showed no statistical differences in fold swelling (Figure A.5), indicating that no differences exist in initial mesh size between the two hydrogel types (104). However, after exposure to collagenase, gels rapidly degraded. In contrast, non-degradable gels, with no bioactive peptides, resisted collagenase degradation. Moreover, enzyme-sensitive gels remained unchanged in culture medium over one week, demonstrating that active collagenase enzyme, and not other factors in medium, was the

main effector of changes in hydrogel integrity. The implications of these results are twofold: 1) cells should be able to locally degrade the gel by releasing proteases, and 2) cells encapsulated within an MMP-sensitive hydrogel could be recovered, via addition of exogenous enzyme, for further analysis or implantation into tissue defects. Thus, this system allows cells to be exposed to highly controlled 3D environments, with precise biochemical and mechanical stimulation, to "prime" cells prior to retrieval for further therapeutic applications.

Confocal microscopy and image analysis were used in tandem to verify cell viability within the construct as well as evaluate changes in MSC morphology during culture (Figure 5.1). At 14 days, cell spreading was visually noted in both types of gels, with image analysis revealing that significantly more cells were spread in fast-degrading gels relative to slow-degrading gels, regardless of strain condition (Figure 5.2). By staining for actin filaments, qualitative differences in the cytoskeletal network between cells in slow- and fast-degrading gels were also observed (Supplementary Figure B.1). Although the exact proteases secreted by these MSCs were not characterized, enough active enzyme was produced to cleave local matrix and allow spreading to occur, as clearly evidenced in the LIVE/DEAD images (Figure 5.1). The combination of these degradation and cell morphology results demonstrate the high amount of control that exists in the use of synthetic hydrogels, which provide a blank slate for the precise inclusion and presentation of bioactive factors. In contrast, natural materials, such as collagen, provide a default level of bioactivity that cannot be as easily tailored and therefore may be less useful in isolating effects of specific matrix properties on cellular response to exogenous cues.

Particle alignment to the x-axis was calculated by the generation of best fit ellipses to represent each particle, followed by angle measurement of the major axis relative to the x-axis (Figure 5.3). To determine if angle distributions in individual gels were non-uniform, particle angle distribution for each gel was compared against uniform distributions using a chi-squared goodness-of-fit test. The inconsistent nature of gels that exhibited non-uniform distributions suggests that cells did not align when static or dynamic strain was applied. The presence of a covalently crosslinked, non-aligned scaffold – as opposed to fibrous collagen gels, where pore sizes are larger and facilitate cell movement (167) – may have deterred cell reorientation over this time period. This result can be correlated with a two-part study of human foreskin fibroblasts in proteolytically degradable PEG gels (229, 244). Here, cells were shown to reorient in the direction of strain following the application of 20% static strain for 24h (244). However, cyclic strain (5%, 0.5 Hz, 24h) did not induce changes in reorientation. Although gels between those studies and this one are not directly comparable due to differences in gel type and other particulars of crosslinking, future study of cell reorientation in these types of gels may require the characterization of different strain regimens in inducing changes in cell orientation.

From PicoGreen data (Figure 5.4), although cell number decreases over time, these results correlate with earlier work in our laboratory showing similar effects with MSCs encapsulated in non-degradable hydrogels (89). Importantly, no differences were noted in DNA content between gel types or strain conditions in this study, and confocal microscopy images demonstrated cells were viable at all time points. Thus, cell number is likely not a driving factor behind differences seen among different gel types or strain

conditions. In this study, DNA content was assayed using DNA collected from manually disrupted gels. Because gels were not completely degraded beforehand, the gel likely retained a significant fraction of total DNA. A brief experiment was conducted to compare manual disruption versus enzymatic gel degradation using MSCs encapsulated in fast-degrading, statically cultured gels. Results indicated that degrading the gels indeed resulted in a significant and dramatic increase in the assayed amount of DNA (Supplementary Figure B.2). This points to future use of enzymatic gel degradation to more accurately determine gel DNA content. Nevertheless, an overall decreasing cell number suggests that proliferation continues to be limited by a small hydrogel mesh size (169). Further work remains in providing space for cell proliferation in these materials while maintaining sufficient mechanical properties to allow tensile loading over relevant time periods.

After loading for up to 14 days, MSCs embedded in both gel types were evaluated for expression of genes related to the tendon/ligament fibroblast phenotype (Figure 5.5). Scleraxis, a transcription factor expressed by tendon progenitor cells in developing mesenchymal tissues, is often considered a tendon fibroblast marker (65, 181, 241). In this study, scleraxis was minimally expressed relative to housekeeping genes (data not shown), and was maintained or downregulated in all groups. In contrast, scleraxis was upregulated in a study using rat MSCs in a collagen gel using the same strain amplitude and rate, but with no rest period over 7 days (65). Another study utilizing primary human MSCs in collagen gels showed maintenance of scleraxis expression under 1% strain at 1 Hz for 30 min/day over 7 days (181). Finally, in a recent study, cells from a C3H10T1/2 mesenchymal stem cell line in collagen gels upregulated scleraxis expression under 10%

strain at 0.1 Hz with 10s rest periods (245). Variations in scleraxis expression from what was observed in this study may be attributable to differences in type of scaffold (collagen), cells, or strain regimen employed by other groups.

MyoD expression was erratic and did not vary across gel types or culture conditions. The use of MyoD as an indicator and effector of myofibroblast differentiation is well established (242, 246, 247); however, while MyoD has been studied in examining MSC response to surfaces of different stiffnesses (173), the regulation of MyoD in tendon/ligament fibroblast differentiation has not been studied. Given the use of mechanical tension in this study, the downregulation of collagen I, and the presence of collagen III, there was a possibility that myofibroblast differentiation was occurring in MSCs in this system (248). The data seem to indicate that cells in this system are not differentiating towards a myofibroblast phenotype. Some studies have suggested that myofibroblastic differentiation is desired, and that myofibroblasts are simply "activated" fibroblasts (249, 250). However, myofibroblasts have been associated with inflammatory responses, including tendon disorders, wound healing processes, and fibrosis (242, 251). Further attempts to engineer tendon/ligament should account for myofibroblastic differentiation, whether in a cooperative or antagonistic approach.

Contrary to some previously published reports (65, 89), collagen I gene expression was downregulated over time in all gels; however, although differences were shown between static and dynamic gels at day 7, this difference was not evident at day 14. These results differ from previous results in our laboratory using the same strain regimen, although those experiments used a scaffold that was not enzyme-degradable and MSCs from a different cell bank (89). The reason for the downregulation is unclear, although

one report suggests that some changes in gene expression are dependent on scaffold and cell orientation (252). Although cells were able to spread in these scaffolds, no alignment was visually detected over time in dynamically or statically strained samples in any hydrogel type (Figures 5.1 and 5.3). Since no orientation was observed in these gels, the lack of directional bias may have inhibited potential changes to collagen I expression. However, other results using bone marrow-derived MSCs in a collagen scaffold have indicated collagen I remains relatively unchanged under strain (181). From immunostained sections, collagen I deposition was detected at day 1 and more intense staining was observed at day 14, regardless of gel and strain parameters (Figure 5.6). The deposition observed may simply be a reflection of a high resident level of gene expression observed at day 1 relative to other tested genes (data not shown); therefore, additional gene upregulation might not be expected in this system.

Collagen III and tenascin-C are frequently used as markers of tendon/ligament fibroblast differentiation (9, 17, 59, 89, 253-255). Dynamically strained samples, regardless of gel type, demonstrated an increase in collagen III expression, both over time and relative to static samples. Correspondingly, immunostaining revealed collagen III staining only in dynamically strained gels. This correlates well with data from our laboratory and other studies (59, 89). Tenascin-C levels in all gels at days 7 and 14 were upregulated relative to day 1, with generally higher expression at day 7 relative to day 14. Importantly, however, dynamic samples exhibited significantly higher expression levels of tenascin-C relative to static samples on day 14. Tenascin-C has been previously shown to be regulated by mechanical strain (256) but has also been speculated to play an 'inhibitory for spreading' role that allows cells to modify adhesion contacts to avoid

overstretching (16). Thus, restricting the ability to alter cell shape under strain may have triggered increased tenascin-C expression in slow-degrading dynamic gels relative to fast-degrading dynamic gels on days 7 and 14. Differences in gene expression levels, however, were not readily correlated with immunostaining. Tenascin-C was detected at day 1 and day 14, with visually increased staining in all samples at day 14. The lack of differences between groups at day 14 may have been related to the consistent expression levels between groups on day 7. Longer culture times might provide tensile strain-related upregulation of gene expression more time to emerge in the form of increased staining at time points beyond day 14.

In this study, all samples, whether statically or dynamically cultured, were removed from the tensile culture bioreactor for a minimum of 2 hours before RNA was extracted from cells. Limited information is available concerning the kinetics of gene regulation after applying mechanical strain to cells in orthopaedic tissues (257-259). In a study where chondrocytes were subjected to hyperosmotic loading, aggrecan promoter activity was maintained one hour after isosmotic loading was resumed but had returned to normal levels by the next time point, five hours after loading (257). Other studies have detailed effects of mechanical strain that last several hours. Strain-related phosphorylation of ERK1/2 in rat Achilles tendon fibroblasts in a fibrin gel required only 10 minutes of strain, returned to basal levels after one hour, and the refractory period lasted six hours (259, 260). This suggests that downstream effects of ERK activation do not require strain to be applied beyond a short duration (261). In another study, chick embryo fibroblasts required a minimum of two hours of cyclic strain (10%, 0.3 Hz) followed by 4 hours of rest to upregulate tenascin-C expression levels (258). These

studies in tandem imply that transient changes in strain-linked gene expression may last through several hours. Collagen III and tenascin-C expression levels in dynamic samples were upregulated at day 14 relative to day 1 samples; both day 1 and day 14 samples were subjected to a period of cyclic strain with rest, suggesting that higher expression levels in tenascin-C are an adaptation to strain applied over time. Future studies could be performed to characterize the temporal aspects of strain-induced gene expression to optimize strain regimens for directing long-term construct culture.

Together, the results of this study indicate that in a synthetic hydrogel system with highly controlled presentation of adhesive and degradable bioactive ligands, MSCs were shown to differentiate towards a tendon/ligament fibroblast phenotype based on changes in relevant gene expression and ECM deposition. This experiment, along with previous experiments in our laboratory (89), suggests that tendon/ligament differentiation can be recapitulated based on the application of mechanical strain, without providing natural cues in the form of a collagen, fibrin or fibronectin-based biomaterial. This experiment also suggests that the level of hydrogel susceptibility to MMP degradation, with corresponding changes in morphology of embedded cells, does not affect MSC response to cyclic tensile strain. However, it should be noted that, in these experiments, significant cell spreading was seen only at 14 days, which was the longest time point examined. A longer culture period may be needed to allow changes in spreading to affect gene expression levels accordingly. Alternatively, cells could be precultured in gels to allow spreading prior to tensile loading, as cell shape has been demonstrated as a potent influence on differentiation state (172). However, the interplay between mechanical strain and cell geometry on cell differentiation is not fully understood, and requires further

clarification (262). It is also possible that the inclusion of RGD peptides in all gel types, which interact with integrins on MSCs, might facilitate cytoskeletal interactions with the synthetic scaffold and enable sensing of mechanical strain (113). Thus, cells in slow-degrading gels may be able to respond to tensile strain even if their ability to spread is limited.

Finally the pericellular matrix surrounding a cell may factor into local principal strains experienced by the cells. Deposition of collagen I, collagen III, and tenascin-C were localized to encapsulated cells (Figure 5.6), which may reflect protein within or adjacent to the cell. In bone and cartilage tissues, it is believed that small strains can be amplified into larger strains via effects of fluid drag forces on the pericellular matrix surrounding an encapsulated cell (263-266). Moreover, factoring pericellular matrix into a finite element model of cell-matrix interaction in cartilage resulted in stress concentrations at the cell border due to different mechanical properties of the cell, the pericellular matrix and the extracellular matrix (214). In this study, any pericellular matrix secreted by cells could have factored into MSC response to strain by communicating forces different from macroscopic predictions (Chapter 4). Manipulating the expression and distribution of this matrix, and characterizing the mechanical properties of deposited matrix, could therefore permit the examination of pericellular effects on cell differentiation (267). A recent finite element model of fluid flow within tendon tissue was designed to predict fluid flow-induced shear stresses (217), but actual shear stresses *in vivo* are currently unknown. Synthetic gels could be employed as part of validating finite element models that predict shear stresses on encapsulated cells due to pericellular matrix deposition, and may shed insight into the effect of macroscopic strain

on shear stresses experienced by cells.

5.5 Conclusions

The experiments described here demonstrate that morphology of MSCs can be influenced by the degradability of the surrounding matrix. Similar to previous reports, MSCs embedded in our MMP-sensitive gels react to tensile strain through upregulation of collagen III and tenascin C, which are ECM molecules associated with the tendon/ligament fibroblast phenotype. However, little difference in response to tensile strain from cells embedded in either slow or fast-degrading gels was observed. Such results suggests that in these degradable, synthetic hydrogel systems, spreading may not be a major factor controlling MSC response to cyclic strain, at least over this time period. However, these findings further support this system as a well-controlled platform that allows exploration of the effects of matrix biochemistry on resulting cell response to exogenous cues, such as mechanical loading. As such, these experiments contribute key parameters toward the design of future biomaterial carriers and strain regimens to prime stem cells to a tendon/ligament phenotype prior to release and use *in vivo*.

CHAPTER 6

CONCLUSIONS AND RECOMMENDATIONS

6.1 Summary

Tendon/ligament-bone interface model systems have the potential to provide critical design parameters for enhancing integration in clinical strategies to repair damage to tendon and ligament tissues. Determining the particular cell type, application of various external stimuli, and biomaterial design are some of the challenges still to be resolved to reproduce the biochemical and mechanical heterogeneity of the native interface. MSCs are frequently used as a cell source for tendon/ligament tissue engineering due to their ease of isolation and expansion (57) and their ability to differentiate into multiple cell types, including tendon/ligament fibroblasts (17). The overall goal of this dissertation was to examine how the roles of mechanical strain and matrix degradability regulate MSC behaviors such as morphology, migration and matrix deposition/gene expression to guide parameters for future design of heterogeneous biomaterials. Specifically, a method was developed for monitoring the vertical position of cells encapsulated within a laminated hydrogel. The effects of applying macroscopic strain on the local strain distribution within uniform and heterogeneous hydrogels were explored in a computational model. Finally, the role of scaffold degradability on changes in cell shape and resultant MSC gene expression/matrix deposition in response to cyclic strain was studied. Together, these studies provided insight into the contribution of scaffold degradability and cyclic strain on MSC morphology, movement and differentiation towards a tendon/ligament fibroblast phenotype as part of regenerating the interface between tendon/ligament and bone.

Chapter 3 investigated the effects of including protease-sensitive sequences into non-degradable PEG hydrogels on possible MSC and HT-1080 migration through a laminated hydrogel interface. In a hydrogel layer with cells that was laminated to a second enzymatically-degradable hydrogel layer, the Z-position of cells within their hydrogel layer could be observed and measured through 7 days of culture. However, definitive migration was not observed in this system. In a hydrogel laminated to another hydrogel polymerized in serum, increased percentages of cells appeared to extend outside the originally seeded gel from image analysis, but this could not be visually confirmed. These results suggest that the protease-sensitive peptide used was ineffective in enabling cell-directed degradation and are overall inconclusive with regard to enabling migration across the laminated interface. Techniques developed for characterizing cell position in 3D, however, could act as the basis for useful analytical tools in designing future laminated hydrogels to monitor chemotaxis-related cell migration.

The studies in Chapter 4 characterized the range and distribution of local strain within a simulated hydrogel cultured within a tensile culture bioreactor. The designed finite element model revealed that strain within a tensile culture construct, as cultured in Chapter 5, was uniform throughout the material. When laminates with different interface geometries were formed, the distribution of strain remained unchanged. However, as individual laminated sections increased in relative stiffness, stress concentrations formed due to mismatches in modulus between laminated sections. Increasing the complexity of the interface geometry appeared to widen the distribution of local strains. As a first pass at validating assumption of complete elasticity in the model, measured OPF/PEG-DA construct stiffness was independent of strain rate. These results indicate that the model

accurately represents the local strain environment in terms of pure elastic response to strain. However, hydrogels possess other fundamental properties such as poroelasticity. Further refinements to account for these additional material considerations are needed to accurately model all mechanical factors in the local microenvironment.

Chapter 5 assessed the influence of increased scaffold degradability on changes in encapsulated human MSC morphology as well as MSC response to cyclic tensile strain over 14 days. More cells encapsulated in fast-degrading PEG hydrogels were spread relative to their slow-degrading counterparts at 14 days. Cyclic tensile strain upregulated collagen III and tenascin-C expression at day 14, in both types of gels, relative to both their day 1 and static counterparts. However, certain genes commonly associated with tendon/ligament fibroblast differentiation, such as scleraxis and collagen I, were either downregulated or maintained with cyclic strain over time. Interestingly, cells were observed to deposit increased cell-associated collagen I and tenascin-C in all sample types at 14 days. Cell-associated deposition of collagen III at 14 days was observed only in dynamically strained gels, regardless of gel type. Together, these results indicate that while cyclic tensile strain induces MSCs towards a tendon/ligament fibroblast phenotype, increased degradability appears not to affect MSC response, at least over this time period.

Overall, the findings in this dissertation provide further clarity into the roles of biomaterial degradation and cyclic strain on cell spreading, migration and differentiation towards a tendon/ligament fibroblast phenotype.

6.2 Conclusions

The research presented in this dissertation advances understanding of the roles that strain and material degradation play in tendon/ligament fibroblast differentiation and of the related considerations required in engineering the tendon/ligament-bone interface. Material properties were shown to affect the range and distribution of local strain within a biomaterial construct, and degradability was shown to lead to changes in encapsulated cell morphology, but had limited effects on cell response to cyclic strain in the experimental timeframe. One important concept in this work was the interplay of various material, mechanical, and temporal factors in inducing changes in encapsulated cell phenotype.

Including enzyme-sensitive peptides into the backbone of the hydrogel facilitated cell-directed degradation and enabled complete degradation of gels with addition of exogenous enzyme. Degradation studies showed that complete degradation of a slow-degrading PEG-based hydrogel could be accomplished if 50% (by weight) or more of the polymer formulation was sensitive to enzymatic cleavage. The two peptides used in these studies had varying rates of protease sensitivity, as evidenced by the time required to degrade the gels in exogenous solution (1 hour vs. 10 min) and the significant difference in cell morphology between human MSCs encapsulated in both types of gels (Figure 5.1). The data regarding spreading of bovine MSCs in OPF/PEG-DA gels doped with increasing concentrations of slow-cleaving PEG is also instructive; changes in cell circularity in these gels was dependent on the presence of the RGD adhesive peptide, not on the amount of slow-cleaving PEG present (Figure A.4). Further culture of hMSCs in these gels led to slight changes in morphology over time; however, significantly more

cells in fast-degrading PEG were spread compared to their slow-cleaving counterparts (Figure 5.2). The implication here is that the degradation kinetics of the peptide used was a significant factor in changes in cell morphology. Circularity analysis appeared to distinguish between relatively unadherent, adhered, and spread cells, based on the circularity data among various studies (Figures A.4 and 5.2). The circularity values are not directly comparable because images were not collected in exactly the same manner, and the cell types used in Appendix A and Chapter 5 were not identical. However, using a circularity of 0.7 to distinguish between spread and unspread cells, 30% spread cells represented cells in scaffolds without RGD; ~50-60% represented cells in materials with RGD; and ≥ 80% spread cells represented appreciable gel degradation. When studies in Chapter 3 were performed, a more easily cleaved sequence had not been developed; thus, significantly longer culture times would likely be necessary to see any large-scale, detectable changes in migration using the slow-cleaving sequence. Naturally, use of a more highly protease-sensitive PEG might enable such studies in a shorter timeframe. However, behavior of cells in PEG-based hydrogels would still be different than cells encapsulated in collagen or fibrin gels, where pore sizes are orders of magnitude greater (roughly 1 μm compared to ~20 nm) (167) and thus facilitate cell migration. Future experiments should perhaps employ PEG-based materials designed with greater pore sizes to hopefully enable comparable migration rates with natural polymer hydrogels.

When hMSCs were cultured in the tensile culture bioreactor, directed cell migration was not studied, as there was no *a priori* reason to expect directed, large-scale cell movement as conceived in Chapter 3. However, in a system where multiple cell types are cocultured in the same construct, soluble factor communication between cell types

may induce chemotaxis-driven migration, as other coculture experiments in 3D have demonstrated (148). Naturally, gradients of chemotactic factors may also induce large-scale cell migration in 3D as well. The work in Chapter 3 highlights the ability to capture the Z-position of encapsulated cells, providing additional information in coculture experiments where cells may migrate perpendicular to the plane of imaging. However, in laminated materials with multiple layers, a second prepolymer solution must diffuse into the first and create a mechanical link via interpenetration of the first layer (191). Therefore, the interface itself would likely exhibit a lower mesh size, impeding soluble factor diffusion as well as migration across the interface (203, 210). Migration also appears to be distance-dependent, concomitant with soluble factor diffusion between cell types (148). The use of degradable biomaterials thus enables further characterization of cell migration in 3D. With respect to interfaces, cell migration may be employed to populate and remodel regions that were previously cell-free (3, 78). However, use of non-degradable and degradable areas in tandem, using a multi-layer structure, provides opportunities to study spatial aspects of interface tissue remodeling; for example, one cell type could be immobilized in a non-degradable layer, secreting soluble factors to induce chemotactic migration of a separate cell type into an area of different mechanical properties. Such a model could perhaps mimic aspects of ligament-bone interface formation – multiple cell types, variations in mechanical properties, and possible cell invasion/remodeling – in a highly configurable *in vitro* model using degradable biomaterials.

The role of mechanical forces in tendon/ligament fibroblast differentiation has been previously studied (65, 89). Here, chapters 4 and 5 investigated the role of cyclic

tensile strain in MSC differentiation. Although cyclic strain has been previously shown to upregulate genes and deposit ECM associated with tendon/ligament fibroblasts in PEG-based systems (89), the nature of the local strain environment was not known. Thus, in Chapter 4, a finite element model was designed in a hydrogel in the tensile culture bioreactor used in Chapter 5. The model predicted stress concentrations at areas of modulus mismatch; overall, however, the majority of local strains throughout the construct were between 9 and 10.5% (Figure 4.4). This result supported gene expression and matrix deposition from all locations in the gel as being sufficiently, consistently related to the application of 10% strain to be evaluated as one population. If substantial deviation in local strain was predicted, great care would have had to be taken in isolating particular regions of each gel to properly correlate local strains with the gene expression and ECM deposition of cells in each region. As such, the finite element model provided clarity into the possible range of local strains and clarified whether or not the gel could be evaluated as a single entity. The model also determined that the use of stiff polyethylene endblocks represented an improvement over a previous design; finite element modeling predicted large variation in local strains within the central region of the old construct (218). Thus, the development of this system significantly improves the uniformity of local strain throughout the material. However, in future development of interface tissue model systems, cocultures of different cell types, e.g. MSCs and osteoblasts, could lead to spatial differences in mechanical properties due to mineralized matrix deposition by osteoblasts (6). Alternatively, gels with laminated sections or graded stiffnesses could be used (174). Local strains in these gels would therefore not correlate with the magnitude of applied strain. Thus, the model presented here provides insight into the distribution of

strain due to mismatches in modulus, gives guidance for manipulating strain fields in future studies, and highlights the need for spatially mapping stiffness to provide a more accurate picture of how strains are distributed over the entirety of a heterogeneous material.

The accuracy of any model depends on the accuracy of its input variables and the fidelity and reliability of its behavior. While the presented model provided an accurate first approximation of local strains within the hydrogel, additional data would be required to increase its accuracy and make conclusions regarding more precise claims, including the strains and forces are actually being applied to cells. Previous finite element models related to this system factored poroelasticity into the model (218); indeed, hydrogels are fundamentally poroelastic materials, as their weight is primarily water, and as water is free to flow in and out of the polymer matrix. Finite element models which model fluid flow on cells in 3D materials have shown that fluids moving within a tissue structure can induce shear stresses on cells (263-265). As a more precise explanation, this is thought to be due to fluid pulling on the pericellular matrix surrounding the cell, creating a drag force that amplifies local strain (266). In bone, this is thought to explain the paradox in bone tissue where tissue-level strains of $< 0.2\%$ produce biochemical responses in cells that require strains that are an order of magnitude higher in *in vitro* studies (266). Thus, fluid flow may be incorporated into finite element to determine more precise information about the cell's mechanical microenvironment. Such models have already been developed for tendon tissue (217), but not for *in vitro* gels in this system. Further characterization of any pericellular matrix deposited in these gels by encapsulated MSCs may shed insight into the role of fluid flow on strains experienced by MSCs.

The concept of modulus mismatch is a significant factor in the utility of the finite element model. Although the model predicted stress concentrations due to differences in stiffness between the gel and the polyethylene endblocks, variations in strain due to interface geometry were not detected when both sections of a laminate hydrogel had the same modulus. Limited information is available regarding the mechanical stiffness of the interface. As discussed previously, however, due to diffusion of the second prepolymer solution into the first, the interface itself would likely exhibit a lower mesh size and would therefore have different mechanical properties, as higher mesh size is correlated to lower modulus (210, 268). Characterization of the interface modulus, as well as knowledge of the dependence of interface dimensions on crosslinking time, would lead to differences in stiffness between the two laminated sections, and would generate subsequent variation in local mechanical strains. This could be performed via nanoindentation or atomic force microscopy (86, 223, 225) to measure surface properties, to provide a first pass approximation of differences in stiffness. Differences in stiffness would also be found at the cell-matrix interface due to potential disparities in the modulus of pericellular matrix. Here, cell associated collagen I, collagen III, and tenascin-C were detected at 14 days in some or all samples (Figure 5.6), which could indicate the presence of pericellular matrix. In cartilage, deposited pericellular matrix has also been shown to have a different modulus than surrounding ECM (269). This information has informed finite element models that predict strains at the cell-pericellular matrix interface that are greater than strains in the surrounding ECM (214, 270). Including the dimensions and mechanical properties of deposited ECM modulus (267) would provide a foundation for a finite element model of a cell's mechanical microenvironment in these gels.

Results of Chapter 5 revealed that MSCs undergoing cyclic tensile strain (modeled in Chapter 4) upregulated genes associated with tendon/ligament fibroblasts, including collagen III and tenascin-C (Figure 5.5). The variety of tensile strain regimens, cell types, and biomaterial scaffolds used in tendon/ligament tissue engineering makes direct comparison with individual studies difficult. However, combined with a previous experiment conducted in this laboratory (89), this chapter indicates that tendon/ligament fibroblast differentiation can be achieved in the absence of a natural biomaterial such as collagen, fibrin or fibronectin by using a completely synthetic scaffold with highly controlled presentation of adhesive and degradable ligands and cyclic strain. This work represents an important step forward in describing the sufficiency of mechanical strain alone in promoting ligamentous differentiation of MSCs encapsulated in an arbitrary 3D environment, and dissolves the notion that a complete recapitulation of the native environment is necessary to ensure desired changes in cell phenotype.

It is important to note, however, that other genes representative of tendon/ligament differentiation were either maintained or downregulated over time, including scleraxis and collagen I. There is general agreement regarding the upregulation of collagen III and tenascin-C gene expression in cells undergoing cyclic strain (59, 89, 125, 271-273). Less agreement exists with regard to scleraxis (65, 181, 245) and differences may indeed be attributable to the type of scaffold (collagen versus PEG in this study), cell type, or strain regimen. Collagen I expression is typically increased under cyclic strain, but upregulation is not consistent (65, 89, 181); in this work, cyclic strain only maintained collagen I expression through 14 days. However, resident collagen I expression levels were high relative to other tested genes (not shown), and collagen I was

observed in immunostaining in all gel types, along with tenascin-C and collagen III (cyclic only) staining, at day 14 (Figure 5.6). Positive staining showed protein mostly localized around the cell; however, soluble secreted ECM molecules may have diffused from the gel and would not have been detected in immunostaining. Together, the variation in reports between gel types, strain regimens and scaffolds make it difficult to establish an accepted set of differentiation markers and strain regimens that induce upregulation of those markers. Moreover, it is unclear whether long-term application of cyclic strain, in a similar fashion to osteogenic and adipogenic differentiation protocols, induce a differentiation state in MSCs that is maintained even after strain is no longer applied. Thus, future refinement would help produce standardized conditions that could be used to properly evaluate the extent of tendon/ligament differentiation.

Interestingly, the gel type did not significantly influence the gene expression and ECM deposition of MSCs undergoing cyclic tensile strain. In this system, significant degradation (as measured by changes in cell shape) was only detected at 14 days; longer culture may be needed to allow time for degradation-driven changes to take hold. Gels may also be precultured in advance, to allow significant degradation to occur prior to cyclic loading. However, it is possible that mechanotransduction via integrin binding is primarily responsible for strain-induced changes in MSC behavior, enabling cells in slow-degrading gels to respond similarly even though degradation was restricted. Thus, cells could be cultured in degradable scaffolds that enable migration and material remodeling, allowing other aspects of cell behavior to be studied without significant changes to gene expression and ECM deposition as a result of using a degradable or non-degradable material. Further study of degradability and its connection to MSC response,

however, would provide additional clarity.

6.3 Future Directions

The findings in this dissertation provided significant insight into the roles of biomaterial degradation and applied cyclic strain on MSC spreading, migration and differentiation towards a tendon/ligament fibroblast phenotype. Future work can utilize the insights gained from this dissertation, where cell behavior was mostly studied in homogeneous materials, as a foundation for future studies that apply degradation and strain to heterogeneous biomaterials to gain biological insight for improving interface tissue engineering therapies.

The ability of cells to migrate within their environment can be exploited in the design of biomaterial models used to provide insight into how cells infiltrate and remodel tissues. The studies in this dissertation provided limited conclusions regarding the extent and control of migration. However, the use of synthetic materials with engineered protease sensitivity equivalent to natural polymers, or a similarly controllable system for degradation, would allow for characterization of cell migration as a function of matrix degradability. Additionally, directed (and thus not random and non-specific) migration could be studied using a defined bioreactor system to generate defined concentration gradients of soluble factors within a biomaterial. Such a system would allow for a combinatorial approach to investigating the factors responsible for enabling or restricting cell migration, and could utilize techniques developed in this dissertation for tracking migration on a large scale. For example, one could study the extent of migration over time, the length and variation in chemotactic gradients of a given factor that are required

to elicit cell migration, permissiveness of the biomaterial matrix to soluble factor diffusion, or the volumetric density of degradation ligands for encouraging or restricting movement. Together, a controlled design would enable a combinatorial approach to explore univariate or multivariate factors in driving cell migration. Such a biomaterial system could also provide opportunities for investigating other factors in cell migration, including durotaxis- and haptotaxis-driven mechanisms. For example, gradients of stiffness in hydrogels generated by differential crosslinking times, or control of specific integrin binding through targeted peptide sequences, would be highly valuable in characterizing other aspects of migration in 3D.

Although migration due to chemotactic factors was briefly explored in this dissertation, what was not explored was cell migration, gene expression, and ECM deposition in response to paracrine signaling due to coculture with another cell type. Knowledge regarding the extent of chemotaxis in 3D may prove useful before even attempting to place cells in coculture; for example, coupling matrix degradability with coculture may encourage cell migration due to chemotactic factors released by one cell type, placing both cell types closer in proximity and further enhancing the effect of possible paracrine signaling. *A priori* knowledge of the effect of soluble factors, then, would elucidate whether cell migration could occur to a substantial degree in a particular system due to coculture, and would provide insight into whether migration would be necessary in terms of encouraging ECM deposition and remodeling of a biomaterial construct designed for regenerating an interface. Coculture also adds an additional layer of complexity due to possible crosstalk between cell types – both via paracrine and direct cell-cell contact – and it will be necessary to carefully distinguish the effects of paracrine

crosstalk from the other individual stimuli in a tensile culture bioreactor - namely strain, scaffold degradability, other mechanical factors, time, and exogenously added soluble signals.

While finite element modeling demonstrated that local strain fields vary with variations in stiffness and interface geometries, the exact mechanical perturbations that a cell ultimately senses remain unknown. Future work could modify the finite element model to account for the effects of poroelastic fluid flow on forces acting on the cell. The effect of strain on an individual cell could also be predicted more accurately by accounting for different cell geometries based on possible changes in cell shape. Characterizing the mechanical properties of the interface would also provide additional information to the model; differences in modulus between the interface and the gel itself would lead to stress concentrations, and, owing to its likely increased modulus, possibly reduce local strain at the interface, further broadening the distribution of strain. Furthermore, cells encapsulated in these gels were shown to deposit cell-associated matrix over time. As this process occurs, strain fields within the construct could be significantly altered. This would also occur in laminates seeded with different cell types, such as MSCs in one layer and osteoblasts in another; long-term culture could further modify local strain fields due to spatially targeted deposition of ECM with different mechanical properties, such as mineralized matrix. Measurement of local mechanical properties over time would provide additional parameters to refine the accuracy of the finite element model, and could elucidate the changing influence of mechanical strain as the construct is remodeled by encapsulated cells.

Throughout development of future constructs, continuous employment of finite

element modeling would provide a basis for interpreting the contribution of various mechanical factors – whether passive mechanical properties or active mechanical stimuli – on the experimental performance of the model/construct design. In addition to experiment analysis, modeling could also be used to inform future construct designs; with an accurate model, ever more complex geometries and heterogeneities could be explored to predict theoretical strains experienced by encapsulated cells in elaborate 3D tissue structures. Models which capture the temporal and spatial effects of tensile strain, then, could provide insight into the design of future clinical solutions for tendon/ligament tissue replacement; for example, localizing macroscopically applied strain to an MSC-seeded soft section of a tissue engineering construct by designing an osteoblast-seeded stiffer section, or designing constructs to induce spatially targeted differentiation in different regions of a construct based on mechanical strain alone. The distribution of strain, as well as its resulting effects on construct development, would not be known in advance unless finite element modeling were performed.

Some of the aforementioned proposed studies – the nature of chemotactic migration in 3D, the nature of cell migration and crosstalk in coculture, and spatiotemporal changes in local distributions of strain – are combined in the study of interface tissues, where the development of heterogeneity may require the interaction of mechanical forces, materials with bioactive functionality, cell migration within the interface region, and crosstalk between the constituent cell types adjoining the interface. For example, interfaces between orthopaedic tissues – whether cartilage-bone, meniscus-bone, tendon/ligament-bone, or muscle-tendon – contain a great deal of heterogeneity in their biochemical and mechanical characteristics. As an example, a tissue engineering

model system could be designed to support a coculture of cell types representing adjoining sides of the interface, using chemotactically-induced migration to populate a region with cells. Over time, the changing mechanical properties of the interface region – perhaps modeled in advance – could lead to spatially targeted cell differentiation due to local differences in strain. Here, the studies in this dissertation provide a base for monitoring cell migration, modeling local strains within heterogeneous materials, and characterizing the effects of scaffold degradability on strain-linked differentiation.

With regards to non-orthopaedic tissues, synthetic, degradable, heterogeneous biomaterials could be designed to model other tissue interfaces and characterize the role of cell migration in their development or repair, with the additional factor of mechanical loading in influencing cell differentiation. In other tissues, such as blood vessels and skin, the heterogeneity of these tissues could be simulated by multi-layer degradable biomaterials to characterize the nature of cell migration in events such as inflammation and wound repair. Gaining a clear picture of migration through various interface regions would provide insight into the nature of remodeling in these tissues.

In considering other future work, current studies only investigated changes in degradability of the matrix as it related to changes in cell shape, gene expression, and ECM deposition in response to cyclic tensile strain. Changes in cell shape have been shown to affect MSC differentiation in mixed media, but these studies have been done in 2D. Although control of adhesion and 3D shapes would not be as easily designed in this system as on a 2D surface, nevertheless, this system may allow for studying similar effects of cell shape on other types of MSC differentiation (either osteogenic or adipogenic) in 3D. By extending this experiment to laminated structures with different

materials and cells in each layer, changes in cell shape could be restricted to cells in certain layers. This would enable the additional investigation of effects of cell shape and/or cytoskeletal organization on cell response to coculture, that is, paracrine signaling between cell types.

Questions abound regarding the role of MSCs and differentiation towards a tendon/ligament fibroblast phenotype as it pertains to engineering of the interface. While tendon/ligament fibroblast differentiation is typically marked by collagen I, collagen III and tenascin-C gene expression and ECM deposition, it is unclear whether this "tenogenic" differentiation state is an end state similar to adipogenic, chondrogenic, or osteogenic differentiation, in which a cell's phenotype is difficult to reverse. It is also unknown whether strain induces permanent effects on cell behavior. If "tenogenic" differentiation is fragile, induced differentiation may not be retained following *in vivo* implantation and ex vivo preculture would prove ineffective. To answer these questions, the biomaterials used in this work could be applied; the enzyme-degradable hydrogel allows for complete degradation of gels and recovery of encapsulated cells. Different periods of tensile culture, followed by subsequent endpoint differentiation assays, then, would provide useful information regarding the permanence of markers indicative of the tendon/ligament fibroblast phenotype. For example, MSCs could prove to be functionally equivalent in tissue engineering applications when compared to fibroblasts harvested from native tendon/ligament tissues. Alternatively, tendon/ligament fibroblasts could lose upregulated levels of gene expression and ECM deposition following extended culture periods without tensile strain.

The results in this work also pave the way for exploring new paradigms in tendon

tissue engineering. Traditionally, biomaterials are used as carriers for cells and are implanted *in vivo* to replace damaged tissues. However, the use of an enzyme-sensitive polymer in this study enabled complete degradation of hydrogels. Cells could be retrieved following two weeks of culture in a biomaterial environment where multiple inputs were applied to induce desired differentiation. Thus, cells could be "primed" to express certain desired genes and deposit desired matrix ex vivo, and could be applied to an injury site *in vivo* to deposit matrix with higher efficiency compared to unprimed cells. If cells were observed to retain gene upregulation and ECM deposition following tensile culture, biomaterials could be viewed as a method for preparing cells for therapeutic injection into desired locations.

Together, the information gleaned from the studies in this dissertation provide important information for future directions in interface tissue engineering. Techniques developed for determining cell position on a large scale can be expanded in future tissue engineering models to monitor cell migration through complex model structures. Additionally, the characterization of the effect of macroscopic strain on local strain distributions in heterogeneous hydrogels provides insight into future interface designs employing strain. For example, materials could be designed to localize the effects of macroscopic strain to particular areas of a material, using mechanical properties to increase tendon/ligament fibroblast gene expression and matrix deposition in spatially targeted areas. In combination, migration and strain-linked differentiation can be employed in studying the development of interfaces using cocultures and other heterogeneities in construct formation.

The use of synthetic biomaterials enables the precise presentation of adhesive and

degradable ligands to encapsulated cells. By recapitulating native ECM properties in a 3D material, cell behaviors can be precisely studied in a system that mimics a cell's natural microenvironment. Adjusting biomechanical and biomaterial parameters enables the study of cell spreading, migration, gene expression and ECM deposition in response to system perturbation, and provides insight into the design of strategies for regenerating tissues. The model systems developed in this dissertation illustrate the complexity of materials with designed heterogeneity and the need for careful investigation of individual material or mechanical parameters in these systems, but provide useful tools for the study of complex, multi-layer structures in which heterogeneities are explicitly designed. These systems can be used in future experiments to study the contributions of individual cell behaviors, such as cell migration and strain-linked differentiation, on the overall remodeling and development of complex tissue structures. Model systems built from the experiments presented in this work also have applications in other tissues, where similar concepts of cell invasion, differentiation in response to mechanical forces, and response to soluble factors, to name a few, may be individually and collectively evaluated for engineering the regeneration of interface tissues following injury.

APPENDIX A

CHARACTERIZATION OF INCLUSION OF ENZYME-SENSITIVE PEPTIDES IN PEG-BASED HYDROGELS

A.1 Introduction

Poly(ethylene glycol) (PEG)-based synthetic hydrogels have been employed for tissue engineering applications due to their cytocompatibility, intrinsic ability to resist protein adhesion, and relative ease of customizing gels with specific bioactive functionality (10). One such functionality is the sensitivity of the gel to enzymatic degradation, a capability that natural polymer-based hydrogels inherently retain. To engineer enzymatic degradation in these synthetic scaffolds, a variety of matrix metalloproteinase (MMP)-sensitive sequences have been integrated into these hydrogels – that is, LGPA (133), GPQGIWGQ (166), and more recently, VPMSMRGG (140). Although the LGPA sequence has never been compared to the other two peptides, the latter two sequences have been directly compared, with VPMSMRGG demonstrating highly increased sensitivity to MMP-1 and MMP-2 compared to GPQGIWGQ (140). Gels formed from LGPA and VPMSMRGG have been shown to degrade upon administration of protease (133, 140). However, the effects on fold swelling and the ability to degrade due to different concentrations of enzymatically-degradable PEG in a previously non-degradable polymer formulation (OPF 10K:PEG-DA 50:50 wt%) were unknown. Furthermore, the ability of homogeneously distributed, encapsulated cells to spread in these gels was also untested. This work 1) details the characterization of gel properties and degradation in response to varying concentrations of enzymatically-degradable PEG, 2) describes changes in cell morphology over 7 days when encapsulated

in enzymatically-degradable gels, and 3) provides a brief comparison of the differences in degradation between the LGPA and VPMSMRGG sequences. In these studies, PEG-based gels formed with the LGPA peptide were found to be relatively slow-cleaving, while PEG-based gels formed with the VPMSMRGG peptide were found to be relatively fast-cleaving.

A.2 Methods

A.2.1 Polymer synthesis

To characterize hydrogel degradation, a mixture of various ratios of OPF 10K, PEG-DA, and enzymatically-degradable PEG were studied. OPF 10K and PEG-DA were synthesized and characterized as described (Section 5.2.1). Enzymatically-degradable PEG, both slow-cleaving (Acrl-PEG-GGGLGPAGGK-PEG-Acrl) and fast-cleaving (Acrl-PEG-GGVPMSMRGGGK-PEG-Acrl), were synthesized as previously described (Section 5.2.1). In cell studies, the peptide GRGDS was added to enable cell adhesion to the hydrogel via a monoacrylated PEG tether; Acrl-PEG-GRGDS (RGD) was also synthesized as previously described (Section 5.2.1).

A.2.2 Fold swelling and degradation of OPF/PEG-DA gels with slow-cleaving PEG

Total polymer was 10% of initial total gel weight. Polymer formulations consisted of two components: first, slow-degrading PEG; second, a mixture of 50% OPF 10K and 50% PEG-DA by weight. Thus, a 50% slow-degrading PEG hydrogel would consist of 50% slow-degrading PEG, 25% OPF 10K, and 25% PEG-DA by weight; a 0% slow-degrading PEG gel would contain only OPF 10K and PEG-DA. After dissolving the

polymer formulation in phosphate buffered saline (PBS; Invitrogen, Carlsbad, CA) and sterile filtering, 18 mM ammonium persulfate (APS; Sigma-Aldrich) and 18 mM tetramethylenediamine (TEMED; Sigma-Aldrich) were used to thermally crosslink each gel for 10 min. 0%, 10%, 25%, 50%, 75%, 90%, and 100% slow-degrading PEG gels were polymerized in Teflon molds to create cylindrical gels 6 mm diameter and 1 mm thick. Gels were then swollen in PBS for 24h. One group of hydrogels remained in PBS over the time course of the experiment as a control. Another group of gels was instead immersed in PBS with 1 mg/mL collagenase type II (210 units/mg), 3 mM $CaCl_2$, and 10 μL/mL antibiotic/antimycotic solution (A/A; Mediatech, Manassas, VA), sterile filtered and refreshed daily. Gels (n=4) were weighed and lyophilized at 12h, 1d, 3d and 7d after initial swelling. Fold swelling was calculated as wet weight/dry weight.

A.2.3 Cell source

Bovine marrow stromal cells (MSCs) were harvested via a previously described protocol (118). The femur and tibia of an immature calf were isolated (Research 87, Boylston, MA), and marrow was placed into low glucose DMEM containing 10% FBS, 10 mL/L A/A, and 0.01% basic fibroblast growth factor (bFGF; PeproTech, Rocky Hill, NJ). The resulting tissue was then physically disrupted by repeatedly pipetting using 50 and 10 mL pipettes, followed by 16, 18 and 20 gauge needles. After centrifugation, the fatty layer was removed and the mixture was plated for 30 min to allow rapidly adhering cells to adhere to tissue culture plastic. The remaining cells in solution were then expanded in T-150 tissue culture flasks until confluency, then placed in Dulbecco's Modified Eagle Medium (DMEM; Mediatech) with 20% fetal bovine serum (FBS;

Hyclone, Thermo Fisher, Waltham, MA) and 10% DMSO and stored in liquid nitrogen until further use.

A.2.4 Cell spreading study

Hydrogels containing 0%, 25%, 75% and 100% slow-degrading PEG were studied. After sterile filtration, bovine MSCs were homogenously seeded at $20x10^6$ cells/mL hydrogel and the resulting polymer/cell solution was polymerized in 6 x 1 mm Teflon molds. Following gelation, constructs were placed in media and incubated at 37ºC and 5% CO_2. Media was changed 1h and 1d after gelation. At 3d, gels (n=4) were stained with LIVE/DEAD dye (Invitrogen) and imaged using an LSM 510 confocal microscope (Zeiss, Thornwood, NY). For each gel, five images were taken ~200 μm under the construct surface. MSC circularity was determined in an automated fashion using custom software macros written for ImageJ (NIH). Circularity is defined as $4\pi A/P^2$, where A and P are the cell area and perimeter, respectively; 1.0 is a perfect circle. The green channel of each image was thresholded (80 out of 255; number chosen arbitrarily) and particle analysis was performed for each image, providing the circularity of each particle (cell or aggregate) in each image. Circularities were accumulated across the images taken for each gel.

A.2.5 Comparison of MMP-sensitive peptides

Hydrogels formed with different enzymatically-degradable peptide sequences were fabricated and degraded as follows. Three polymers were tested: Fast-degrading MMP-sensitive PEG, slow-degrading MMP-sensitive PEG, and a 50:50 wt% mixture of

OPF 10K and PEG-DA (non-degradable). Each polymer was dissolved in phosphate buffered saline (PBS) to create a 90 wt% water solution, then sterile filtered using a 0.2 μm glass prefilter (Nalgene). 0.07 wt% Irgacure 2959 (D2959; Ciba) in PBS/dimethyl sulfoxide was added to enable photopolymerization using UV light. Liquid prepolymer was deposited in autoclaved Teflon molds and exposed to UV light (10.5 mW/cm^2; 365 nm; UVP) for 10 min to fabricate 6 mm diameter x 1 mm thick gels. Gels were swollen in PBS overnight and then deposited in sterile-filtered PBS with 4 mg/mL collagenase type II (Invitrogen). Plates were then placed on a shaker plate shaking at ~1 Hz. This solution was refreshed every 2 days. To characterize gels (n=4), fold swelling was calculated by W_w/W_d, where W_w is the wet weight of the hydrogel, and W_d is the weight of the hydrogel after drying.

A.2.6. Statistical analysis

Results are reported as mean ± standard deviation. For statistical analysis, all data were transformed using a Box-Cox transformation (243). One-factor and two-factor ANOVA with Tukey's post hoc multiple comparison test were performed accordingly on the transformed data, with statistical significance with $p \leq 0.05$ to indicate significance between individual samples. For fold swelling/degradation data, the factors were day and gel type. For circularity analysis, the factors were the presence of RGD and gel type.

A.3 Results

A.3.1 Gel degradation

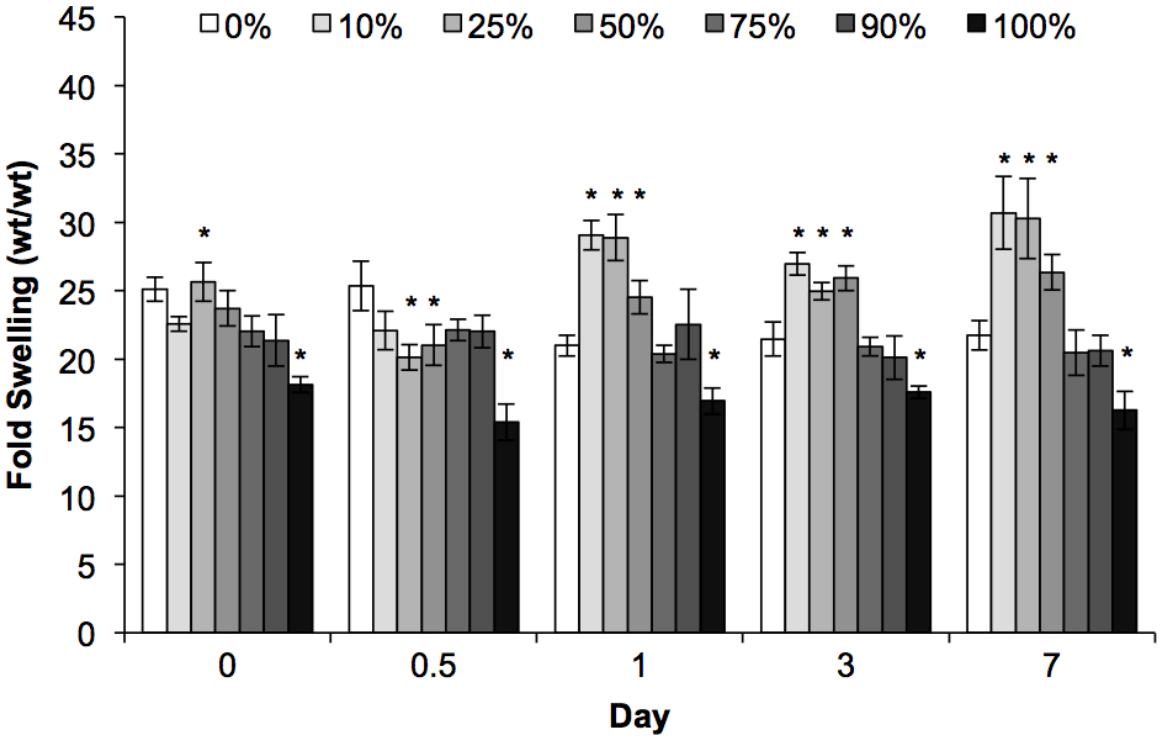

Figure A.1. Changes in fold swelling in hydrogels containing various amounts of slow-degrading PEG (by weight) in PBS over 7 days (n=4). * indicates significantly different than 0% slow-degrading PEG at each time point. Only comparisons to 0% slow-degrading PEG are shown for clarity.

Hydrogels with varying composition of slow-degrading PEG also showed variability in their fold swelling after fabrication (Figure A.1). Of note, at days 1, 3, and 7, gels composed of 10%, 25%, and 50% slow-degrading PEG were significantly higher than 0% slow-degrading (100% OPF/PEG-DA) hydrogels. Further addition of slow-degrading PEG to the hydrogel formulation appeared to decrease the resulting fold swelling of the crosslinked polymer to be statistically comparable to 0% slow-degrading PEG gels. Finally, gels that were completely fabricated from slow-degrading PEG displayed significantly less fold swelling than 0% slow-degrading PEG gels at all time

points.

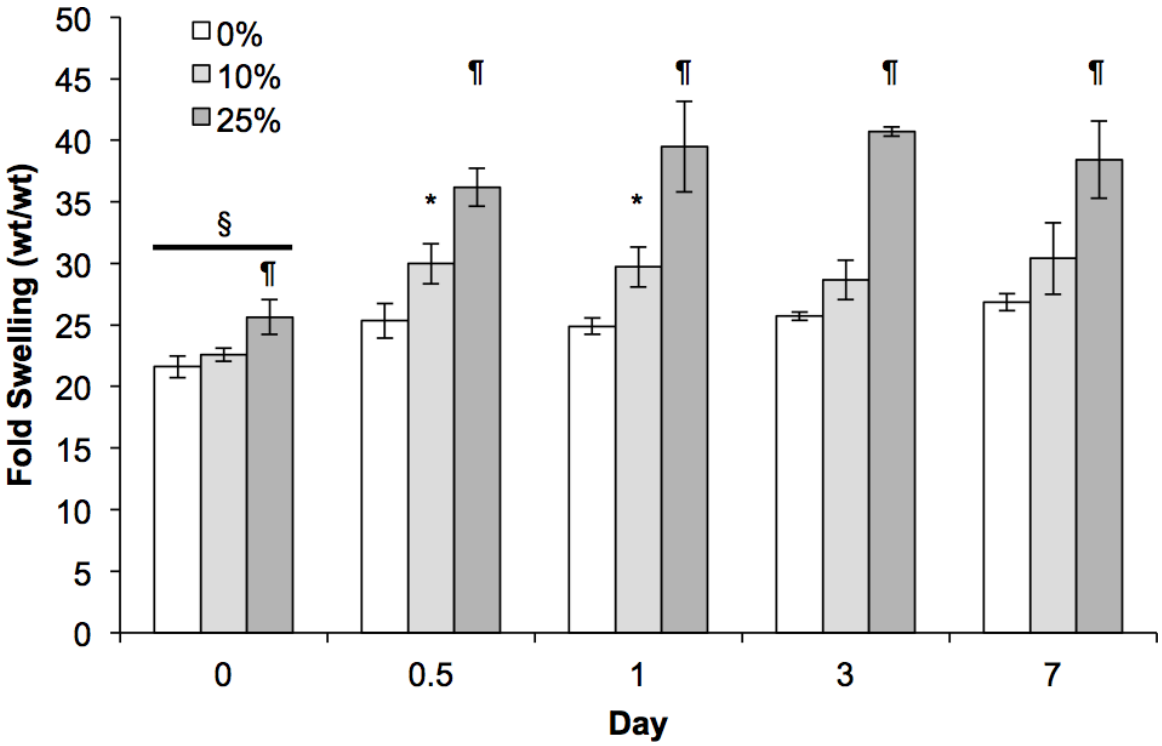

Figure A.2. Changes in fold swelling in hydrogels containing various amounts of slow-degrading PEG (by weight) in collagenase solution over 7 days. All gels ≥ 50% slow-degrading PEG degraded within 0.5d (12h; not shown). § indicates significantly different from all other time points. * indicates significance compared to 0% slow-degrading PEG only; ¶ indicates significantly different from both 0% and 10% slow-degrading PEG.

When gels containing varying concentrations of slow-degrading PEG were immersed in collagenase solution, gels containing ≥ 50% slow-degrading PEG degraded within 12 h (not shown). 25% slow-degrading PEG gels had a significantly higher fold swelling than the other two formulations, but all gels remained whole over 7 days. Following immersion in collagenase, the fold swelling of all gels was significantly higher than their respective gels in PBS. 10% gels were only higher than 0% gels at 0.5d and 1d after addition of collagenase. 25% slow-degrading gels remained significantly higher

than their 10% and 0% counterparts at all time points.

A.3.2 Confocal Imaging and Circularity Analysis

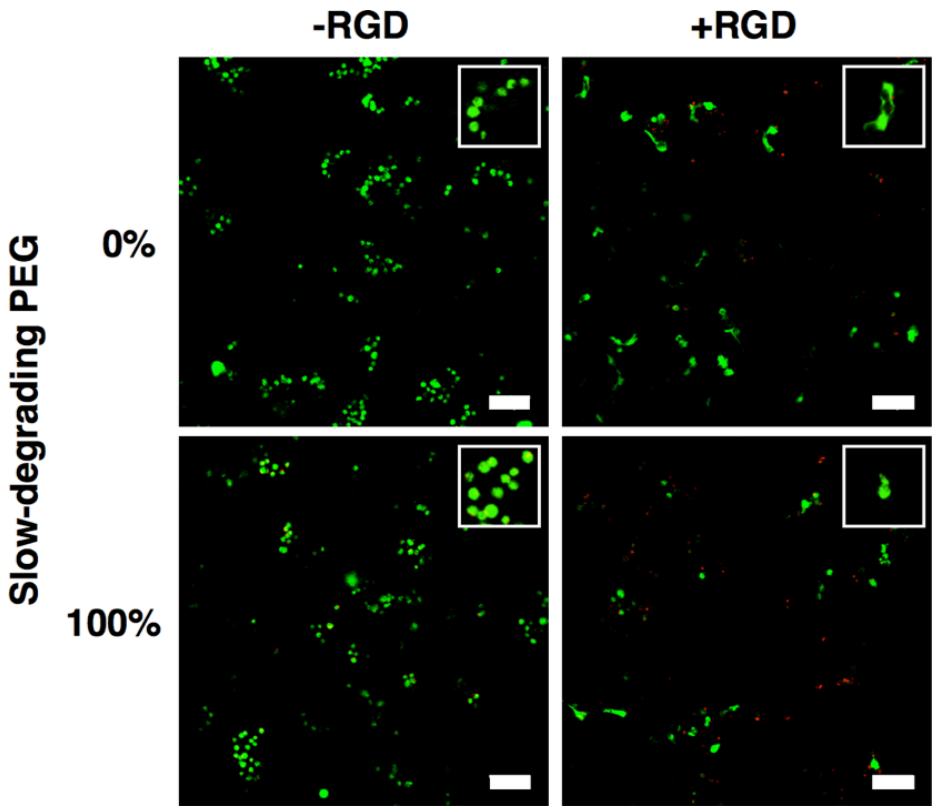

Figure A.3. LIVE/DEAD stained confocal images of bovine MSCs encapsulated within 0% and 100% slow-degrading PEG gels at 3 days. Pictures indicate spreading within all hydrogels containing RGD at 3 days, regardless of the formulation used. Scale bar and inset dimensions are 100 µm.

Confocal imaging revealed that bovine MSCs were viable following encapsulation in 0% and 100% slow-degrading PEG gels (Figure A.3). Upon visual inspection of microscopy images, there were no apparent differences in cell morphology between cells in 0% and 100% gels without RGD. In gels with RGD, there were noticeable changes in morphology indicative of cell spreading, but these changes occurred in both 0% vs 100% gels with RGD. This visual observation was confirmed in

circularity analysis of the confocal images (Figure A.4). The addition of RGD shifted the distribution of particle circularities towards lower values, and significantly increased the fraction of cells below a circularity of 0.7 in all gel types. However, there was little difference between gels with varying concentrations of slow-degrading PEG; the only difference noted was a significant decrease in the fraction of "spread" cells in 100% gels relative to 75% gels.

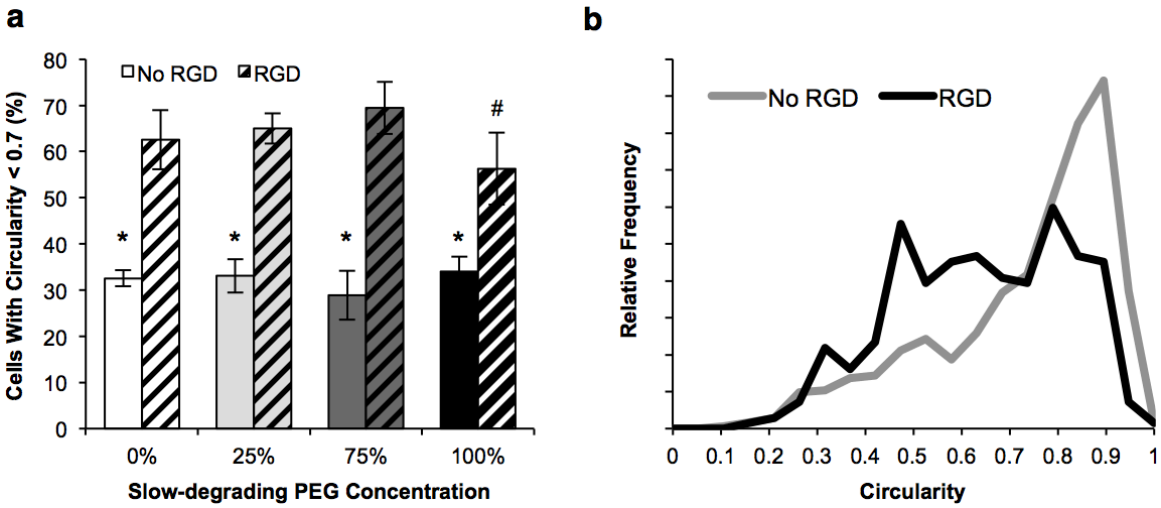

Figure A.4. Particle analysis of LIVE/DEAD images (green channel only) of bovine MSCs encapsulated within 0%, 25%, 75%, and 100% slow-degrading PEG gels with and without RGD (n=4) at 3 days. a) Percentage of cells with less than 0.7 circularity. a) Distributions of particle circularities were combined for 100% slow-degrading gels with and without RGD (n=4). * indicates different from other RGD condition; # indicates significantly different from 75% slow-cleaving PEG with RGD.

All three types of hydrogels – non-degradable, slow-degrading, and fast-degrading - swelled in PBS overnight, with no differences between gel types after initial swelling (Figure A.5). Only one difference in fold swelling between non-degradable and fast-degrading gels in cell culture media was detected at 1 day. No changes in fold swelling were noted at 7 days. Upon gel exposure to collagenase, MMP-sensitive gels

degraded rapidly as expected; slow-degrading gels degraded in 1 hour, while fast-degrading gels degraded in under 10 minutes (data not shown). In contrast, non-degradable gels remained unchanged in collagenase solution over 7 days.

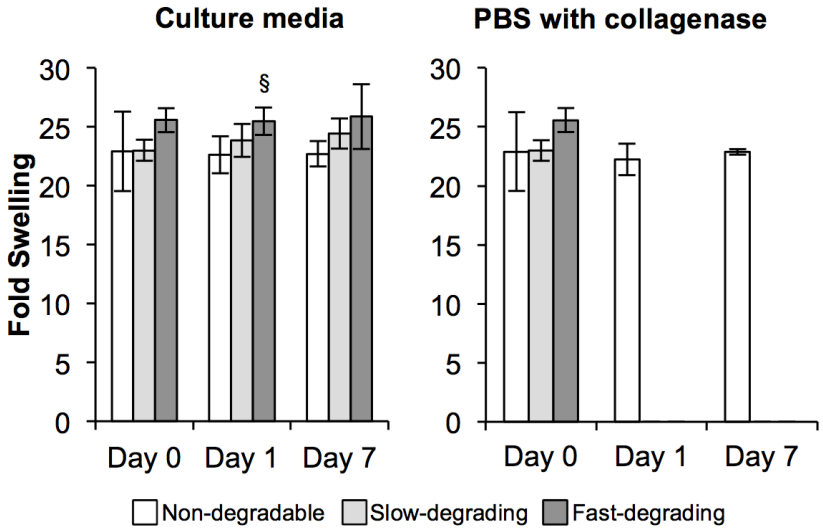

Figure A.5. Fold swelling of hydrogels in culture media and in PBS with collagenase solution at 0 days, 1 day and 7 days. § relative to non-degrading gel (n=4; $p \leq 0.05$).

A.4 Discussion and Conclusions

The incorporation of varying concentrations of slow-degrading PEG into the hydrogel formulation modified the resulting fold swelling ratio of the hydrogels (Figure A.1). Upon addition of a low concentration of slow-degrading PEG, OPF:PEG-DA gels abruptly increased in fold swelling; however, 100% slow-degrading PEG gels swelled less than 0% slow-degrading PEG gels at all time points. Enzymatically-degradable PEG was calculated to have an expected molecular weight of 7600 Da, well below the M_n of OPF 10K (19,800 Da) but higher than PEG-DA (3800 Da). Number average molecular weight and polydispersity index were not calculated for slow-degrading PEG following

fabrication, so the exact purity was unknown. However, fold swelling is linked to mesh size (104, 167, 274), and 100% slow-degrading gels polymerized and swelled less than non-degradable gels. As a hydrogel cannot be formed with poorly unconjugated products (275), this data provides confidence that a significant majority of the peptide conjugation product is presumed to be correctly conjugated. The increased fold swelling upon addition of a small amount of slow-degrading PEG is attributed to the modified nature of the crosslinked network due to different reactivities of the fumarate and acrylate groups (104, 109).

Upon immersion of hydrogels formed from different ratios of slow-cleaving PEG and non-degradable OPF:PEG-DA in collagenase solution, hydrogels degraded commensurate to the amount of slow-degrading PEG (Figure A.2). While gels with more than 50% slow-cleaving PEG degraded by 12 hours, gels with less slow-cleaving PEG changed fold swelling and remained mostly unchanged over 7 days. The immediate change in fold swelling in 10% and 25% gels, demonstrates the high activity of the collagenase for degrading protease-sensitive peptides in the hydrogel backbone. Thus, cells could release enzymes to degrade the hydrogel locally surrounding the cell. Interestingly, 0% slow-degrading gels slightly increased in fold swelling over 7 days. This is attributed to ester hydrolysis-mediated degradation in OPF (102).

Confocal images demonstrated that bovine MSCs were viable when encapsulated in PEG gels with various concentrations of slow-degrading PEG gels (Figure A.3). Spread cells were observed in all gels with RGD, regardless of the concentration of slow-cleaving PEG. MSCs in gels without RGD displayed a mostly rounded morphology, in agreement with other work in PEG gels (169). Moreover, non-degradable gels were not

susceptible to enzymatic degradation (Figure A.5). This data would seem to imply that, in these gels, inclusion of adhesive sites was the main influence on changes in cell morphology, rather than proteolytic degradation.

In these experiments, hydrogels were fabricated using two established MMP-cleavable peptides with different MMP sensitivities (133, 140). Fabricated gels showed no statistical differences in fold swelling (Figure A.5), indicating that no differences exist in initial mesh size between the two hydrogel types (104). Bovine MSCs did not appear to spread in response to enhanced sensitivity to degradation; however, the data suggests that degradation was not sufficiently enhanced to enable increased cell spreading over 7 days. Following exposure to collagenase, both slow-cleaving and fast-cleaving gels degraded in less than one hour. Although exact degradation kinetics of the LGPA peptide used in slow-degrading PEG are not known, the empirical study in this work identified a substantial difference in degradation time between slow- and fast-degrading hydrogels. The difference in time of degradation represents an effective difference in sensitivity to enzymatic degradation, and this is eventually reflected in comparisons in spreading between slow-cleaving and fast-cleaving gels in tensile culture (Figure 5.2). Importantly, enzyme-sensitive gels remained unchanged in culture medium over one week, demonstrating that active collagenase enzyme, and not other factors in medium, was the main effector of changes in hydrogel integrity.

The work here allows for several important conclusions. First, local and bulk degradation of the gel can occur at a rate related to the enzymatic susceptibility of the particular peptide. Secondly, enzyme-sensitive gels can be completely degraded, possibly enabling retrieval of encapsulated cells. Finally, the disparity in degradation time

between different peptides, linked by the identical capability to degrade both gels completely, laid the foundation for studies in Chapter 5, where enhanced proteolytic degradation in fast-cleaving gels enabled the investigation of cell shape under tensile strain.

APPENDIX B

SUPPLEMENTARY FIGURES

B.1 F-actin in hMSCs in Slow- and Fast-Degrading PEG Hydrogels

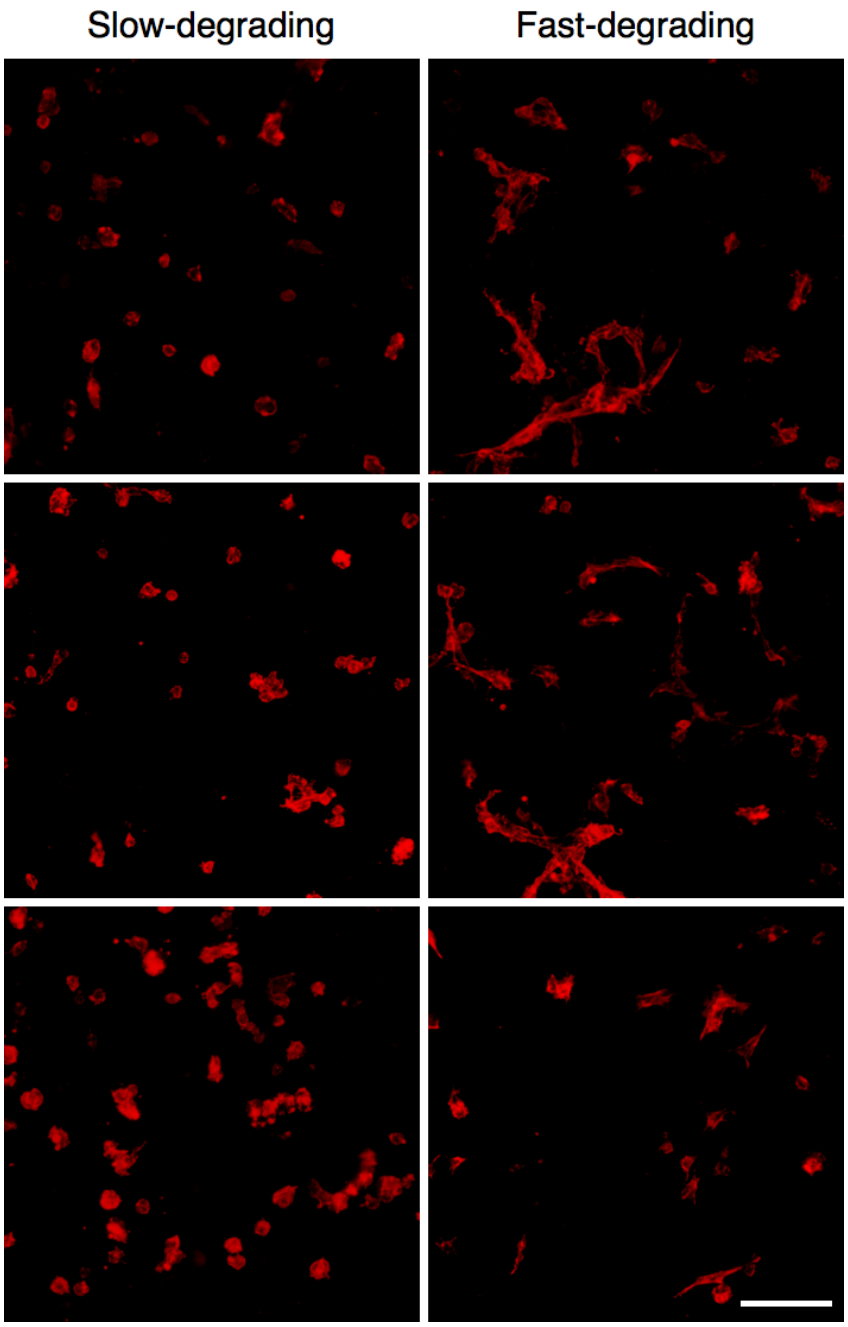

Figure B.1. AF546-phalloidin-stained hMSCs in fast-cleaving and slow-cleaving gels at 14 days (n=1). Each image was taken from a different region in the gel. Scale bar: 100 µm.

Tensile constructs were fabricated using slow-degrading or fast-degrading MMP-cleavable PEG, seeded with MSCs, and statically cultured as specified in Section 5.2.4. At 14 days, gels (n=1) were removed from the bioreactor and incubated in PBS for 30 min. Gels were then immersed in 10% formalin for 30 minutes at 4ºC, rinsed for 30 min in PBS, and stored in PBS at 4ºC. Gels were permeabilized with PBS containing 1% Triton X-100 for 30 min. Following permeabilization, gels were stained for 90 min, with gentle shaking, in PBS containing 1:50 Alexa Fluor 546-phalloidin (Invitrogen) and 5% FBS. After staining, gels were rinsed three times on a shaker plate in PBS for 15 min each, and then imaged on a confocal microscope (Zeiss LSM 510). Three stacks 100-200 μm thick (5 μm interval) were taken from each gel. In ImageJ, each stack was flattened into a 2D image according to the standard deviation of all images in the stack.

B.2 DNA Content in Differentially Processed Samples.

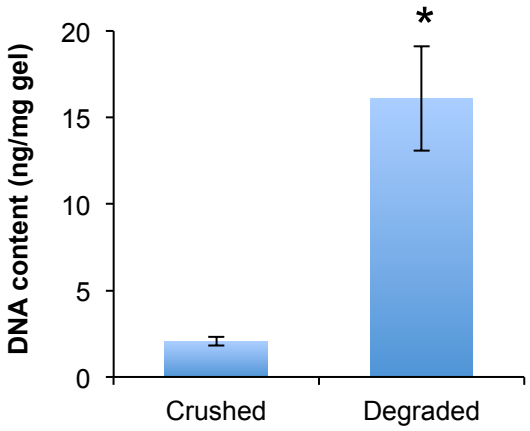

Figure B.2. DNA content in fast-cleaving static gels at day 1. * indicates significance relative to crushed samples ($n \geq 5$; $p < 0.05$).

Tensile constructs were fabricated using fast-degrading MMP-cleavable PEG, seeded with MSCs, and statically cultured as specified in Section 5.2.3. At 1 day, hydrogels (n=7) were split in half with a scalpel and the wet weight of each half was measured. One half of each hydrogel was crushed with a pellet grinder and processed for DNA content according to the protocol provided in Section 5.2.5. The other half of each hydrogel was placed in sterile-filtered (0.2 μm, Nalgene) culture medium with 4 mg/mL collagenase type II (Invitrogen), then shaken gently on a shaker plate for 30 min in a cell culture incubator at 37ºC. Gels degraded completely within that time. Each sample was centrifuged and supernatant was removed. After rinsing in PBS, samples were processed for DNA content as previously specified. Data analyzed using Student's two-tailed *t*-test. Gel sections that were degraded resulted in significantly more DNA, approximately 8 times the amount isolated from crushed gels (16.1 ng/mg vs. 2.1 ng/mg).

APPENDIX C

LABORATORY PROTOCOLS

C.1 OPF Synthesis

Fumaryl Chloride (FuCl) Distillation (if necessary)

Warning: Fumaryl chloride has a very pungent odor. Work only in the fume hood with the sash down as far as possible. Double glove, and leave jars, glassware, used gloves in the hood overnight to air out.

1. Wash and dry:

   2 x 500 ml round-bottom flasks, 1 x joint for thermometer, 1 x thermometer to fit joint (~160°C), 1 x large condenser, 1 x glass elbow, 1 x joint for desiccators, 1 x glass stopper, 1 x glass funnel, 1 x egg-shaped FuCl stir bar.

2. Set up the distillation apparatus as shown, without the FuCl flask and collection flask:

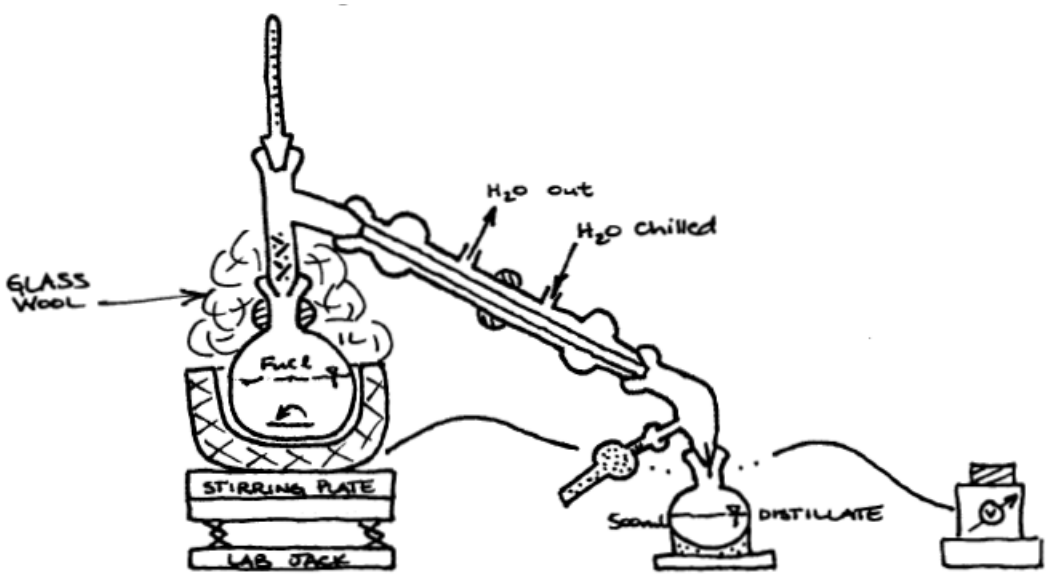

3. Replace the 500 ml collection flask with a 100 ml round bottom flask to collect the first 30 ml of distillate.

4. Clamp the apparatus to the scaffolding in the back of the fume hood.
5. Vacuum grease and clamp all connections.
6. Run cold, ice water UP the condenser tube using the circulation pump. This allows any bubbles to flow up and out of the condenser. Make sure that the circulation pump is not actively heating the water by turning the temperature control all the way down to -20°C.
7. Tie a KimWipe around the bottom of the condenser to catch external condensation.
8. Use the funnel to pour 150 ml (100 g) of FuCl into a 500 ml round-bottom flask.
9. Add the FuCl stir bar into the FuCl flask.
10. Vacuum grease the FuCl flask, and connect the flask to apparatus.
11. Place the flask in heating mantle with magnetic stirring at ~3.
12. Insulate the flask and neck with glass wool all the way up to the condensing tube to promote boiling and prevent condensation.
13. Start the transformer at 40 units.
14. Increase the transformer by 10 units, every 5 minutes.
15. Increase the transformer until the vapor temperature is 160°C (~80 units on transformer).
16. Dispose of the first ~30 ml of distillate by turning the neck up, removing the 1st 100 ml collection flask, and quickly replacing it with a clean 500 ml round-bottom flask.
17. FuCl distillate should be a light amber color.
18. The solution in the heated FuCl flask will become darker and more viscous.

19. When ~50-75 ml remains the heated FuCl flask and the solution is dark brown, turn off the transformer, remove the glass wool, turn the condenser off, and replace the heating mantle with a cork ring.
20. Stopper the FuCl distillate, parafilm the stopper, cover the flask with aluminum foil, and label it.
21. Store the distillate in the 4°C explosion-proof refrigerator.
22. Dilute the FuCl waste with tap water, and leave it in the hood overnight. Be careful of HCl production in the reaction with water, and pour the water in SLOWLY.
23. On the next day, use a spatula to break up the FuCl waste, retrieve the stir bar, and disposed of the waste in the aqueous waste container.
24. Glassware can be cleaned with acetone and the base bath.

Methylene Chloride (MeCl) Distillation

Warning: Use nitrile or silver-shield gloves when handling MeCl.

1. Wash and dry:

   1 x 1000 ml round-bottom flask, 1 x joint for thermometer, 1 x thermometer to fit joint (~40°C), 1 x large condenser, 1 x glass elbow, 1 x joint for desiccators, 1 x glass stopper, 1 x glass funnel.
2. Set up the distillation apparatus as shown, without the MeCl flask and collection flask:

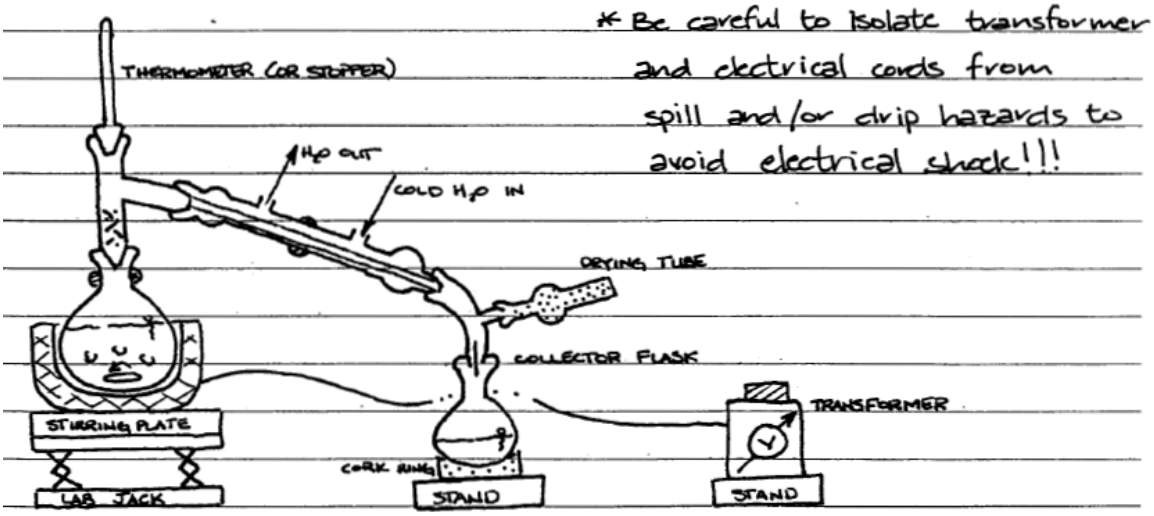

3. Replace the 500 ml collection flask with a 100 ml round bottom flask to collect the first 30 ml of distillate. Clamp the apparatus to the scaffolding in the back of the fume hood.
4. Vacuum grease and clamp all connections.
5. Run cold, ice water UP the condenser tube using the circulation pump. This allows any bubbles to flow up and out of the condenser. Make sure that the circulation pump is not actively heating the water by turning the temperature control all the way down to -20°C.
6. Tie a KimWipe around the bottom of the condenser to catch external condensation.
7. Use funnel to add 750 ml of MeCl and calcium hydride (CaH_2, if needed) into the existing MeCl + CaH_2 flask.
8. Vacuum grease the MeCl flask, and connect the flask to apparatus.
9. The MeCl + CaH_2 flask already contains a stir bar. Place the flask in heating mantle with magnetic stirring at ~4.

10. Insulate the flask and neck with glass wool all the way up to the condensing tube to promote boiling and prevent condensation.
11. Set the transformer to 35 units.
12. Vapor temperature should increase to ~40°C.
13. Dispose of the first ~30 ml of distillate by turning the neck up, removing the 1st collection flask, and quickly replacing it with a clean 1000 ml round-bottom flask.
14. When ~150-200 ml remains in the heated MeCl flask, turn off the transformer, remove the glass wool, turn the condenser off, and replace the heating mantle with a cork ring. You should have ~500 ml MeCl distillate in your collection flask (need 340-380 ml for remaining steps).
15. Vacuum grease the glass stopper, and stopper the MeCl distillate, and label it.
16. Store the anhydrous MeCl distillate in the hood overnight. Do not parafilm the stopper.
17. Vacuum grease the original MeCl + CaH_2 stopper, stopper the undistilled MeCl + CaH_2, and store it in the back of the hood.
18. Dispose of the MeCl waste in the chlorinated organic solvents waste container.
19. Glassware can be dried in the hood, and then cleaned normally.

Azeotropic Distillation of PEG

Warning: Use nitrile or silver-shield gloves when handling toluene.

1. Wash and dry:

   1 x 500 ml or 1000 ml round-bottom flask, 1 x Dean stalk, 1 x condenser,

   1 x glass stopper, 1 x Kontes #2 glass valve with LARGE hole,

   1 x egg-shaped stir bar, 1 x glass funnel, 1 x 250 ml glass graduated cylinder.

2. Set up the distillation apparatus as shown, without the PEG/toluene flask:

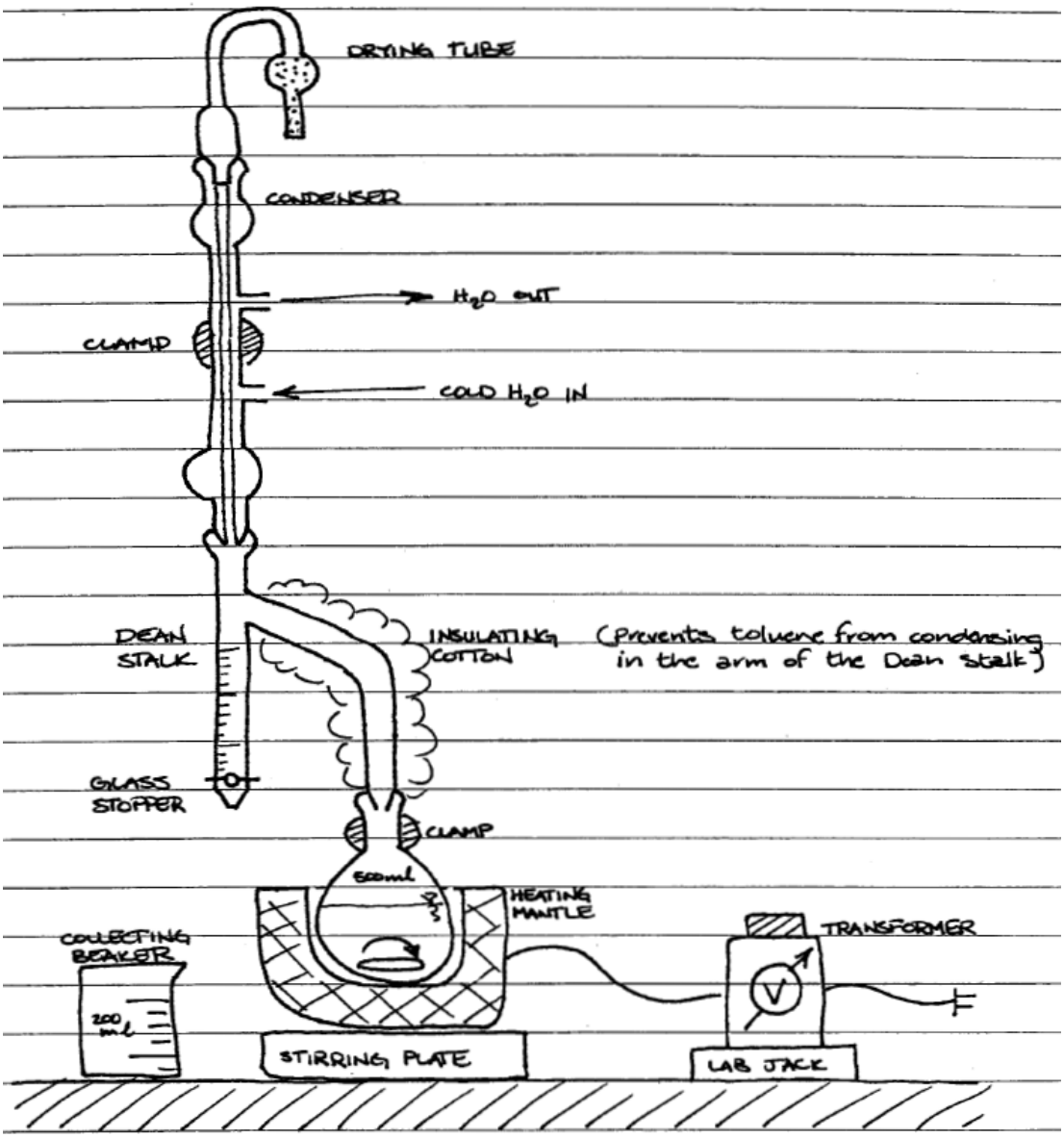

3. Clamp the apparatus to the scaffolding in the back of the fume hood.
4. Vacuum grease and clamp all connections.
5. Run cold, ice water UP the condenser tube using the circulation pump. This allows any bubbles to flow up and out of the condenser. Make sure that the circulation pump is not actively heating the water by turning the temperature control all the way down to -20°C.

6. Tie a KimWipe around the bottom of the condenser to catch external condensation.
7. Weigh 50 g PEG 3.4K or 10K in the 500 ml round-bottom flask.
8. Use the graduated cylinder and funnel to add 200 ml of toluene to the PEG in the 500 ml flask.
9. Add the stir bar to the flask, vacuum grease the flask, and connect the flask to apparatus.
10. Place the flask in heating mantle with magnetic stirring at ~5. The PEG will dissolve with stirring and heating.
11. Insulate the flask and neck with glass wool all the way up to the condensing tube to promote boiling and prevent condensation.
12. Set the transformer to 65 units.
13. When the Dean stalk fills to 20 ml, dispose of the toluene by draining the solution from the Dean stalk into a 250 ml waste beaker. The first few batches of waste may be partially cloudy, while others should be clear.
14. Repeat step 13 seven more times, removing 20 ml toluene at a time until ~160-180 ml toluene has been removed.
15. Turn off the transformer, remove the glass wool, turn the condenser off, and replace the heating mantle with a cork ring. 2-5 ml extra toluene waste may condense as you do this.
16. Allow the distilled PEG and toluene to cool, and then vacuum grease the glass stopper and stopper the distilled PEG. Parafilm the stopper, and label the flask.
17. Store the distilled PEG in the hood overnight. The PEG will solidify as it cools.

18. Dispose of the toluene waste in the nonchlorinated organic solvent waste container.
19. Glassware can be dried in the hood, and cleaned normally.

OPF Reaction

Warning: Use nitrile or silver-shield gloves when handling MeCl.

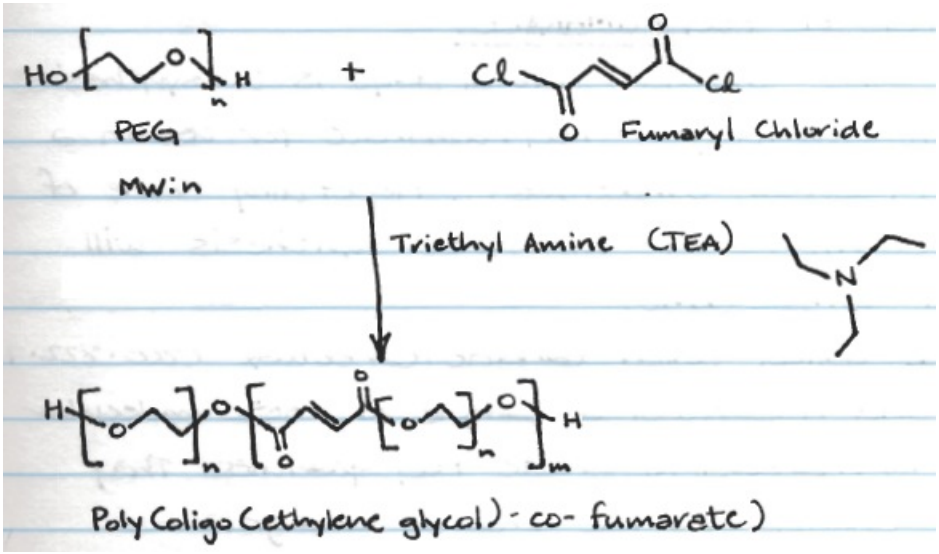

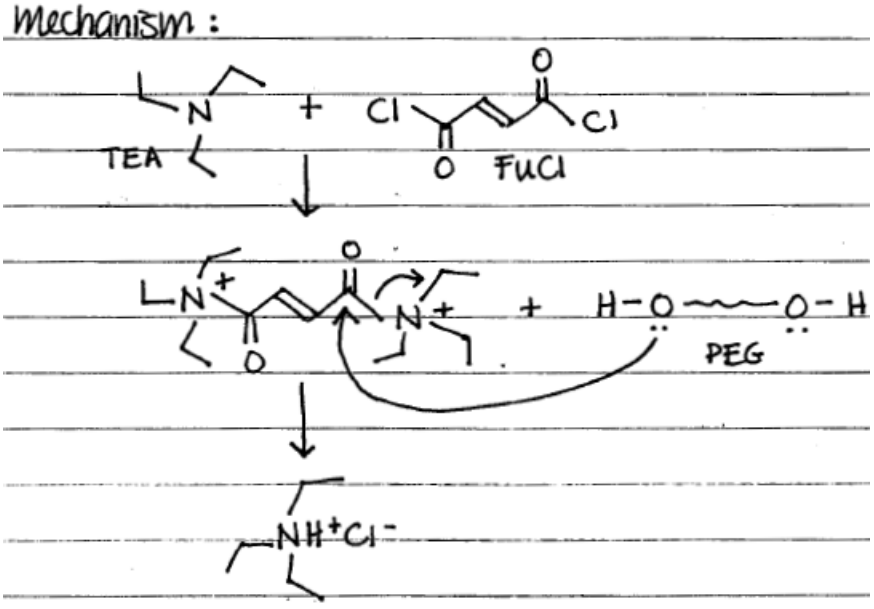

3.4K Calculations:

PEG MW = 3,400 Da

50 g PEG = 0.01471 mol PEG

1 PEG : 0.9 FuCl → 10% molar excess for PEG addition to ends of FuCl

(0.9 mol FuCl / mol PEG) * (0.01471 mol PEG) = 0.01324 mol FuCl

FuCl MW = 153 g/mol

(0.01324 mol) * (153 g/mol) = 2.025 g FuCl

FuCl density = 1.415 g/ml

(2.0235 g) / (1.415 g/ml) = **1.431 ml FuCl**

1 FuCl : 2 TEA → TEA removes Cl from ends of FuCl, 2 Cl per FuCl → Twice as much TEA as FuCl

(2 mol TEA / mol FuCl) * (0.01324 mol FuCl) = 0.02648 mol TEA

TEA MW = 101.2 g/mol

(0.02648 mol) * (101.2 g/mol) = 2.6798 g TEA

TEA density = 0.726 g/ml

(2.6798 g) / (0.726 g/ml) = **3.6912 ml TEA**

10K Calculations:

PEG MW = 10,000 Da

50 g PEG = 0.005 mol PEG

1 PEG : 0.9 FuCl → 10% molar excess for PEG addition to ends of FuCl

(0.9 mol FuCl / mol PEG) * (0.005 mol PEG) = 0.0045 mol FuCl

FuCl MW = 153 g/mol

(0.01324 mol) * (153 g/mol) = 0.6885 g FuCl

Density FuCl = 1.415 g/ml

(0.6885 g) / (1.415 g/ml) = **0.4866 ml FuCl**

1 FuCl : 2 TEA → TEA removes Cl from ends of FuCl, 2 Cl per FuCl → Twice as much TEA as FuCl

(2 mol TEA / mol FuCl) * (0.0045 mol FuCl) = 0.009 mol TEA

TEA MW = 101.2 g/mol

(0.009 mol) * (101.2 g/mol) = 0.9108 g TEA

TEA density = 0.726 g/ml

(0.9108 g) / (0.726 g/ml) = **1.2545 ml TEA**

1. Wash and dry:

   1 x 1000 ml 3-arm round-bottom flask, 2 x 60 ml dropping funnels,

   1 x joint for the N_2 balloon, 1 x PTFE valve for the N_2 balloon,

   2 x Kontes #2 glass valves with LARGE holes, 2 x glass stoppers,

   1 x 250 ml or 1000 ml glass graduated cylinder.
2. Use the funnel and graduated cylinder to add 320 ml MeCl to the distilled PEG/toluene. Dissolve PEG with stirring.
3. Use the funnel to pour the PEG/MeCl into the 3-arm flask. The PEG distillation stir bar can be reused in this step.
4. Set up the reaction apparatus as shown, without the glass stoppers and N_2 balloon:

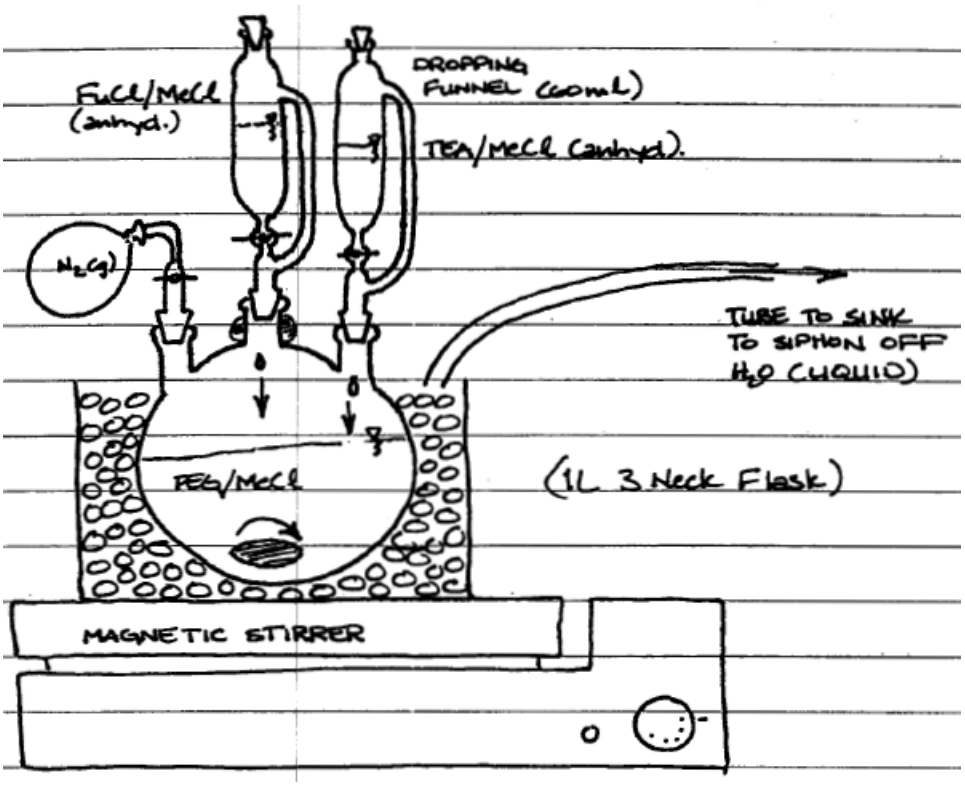

5. Clamp the apparatus to the scaffolding in the back of the fume hood.
6. Vacuum grease and clamp all connections. Be careful not to vacuum grease over the holes in the valves, or else the FuCl and TEA will not flow through. Also the PTFE valve for the N_2 balloon does not require vacuum grease.
7. Place the 3-arm flask in a small autoclave bin, filled with ice on a large stir plate. Optional: Add salt to the ice to keep the ice from melting.
8. For PEG 3.4K, use glass pipettes to add 30 ml MeCl to volumes of FuCl and TEA calculated above (3.4K: 1.431 ml FuCl and 3.6912 ml TEA). Add MeCl to dropping funnels first, then FuCl and TEA. MeCl removes the markings from glass pipettes, so exercise care when transferring MeCl.

9. For PEG 10K, use glass pipettes to add 10 ml MeCl to volumes of FuCl and TEA calculated above (10K: 0.4866 ml FuCl and 1.2545 ml TEA). Add MeCl to dropping funnels first, then FuCl and TEA. MeCl removes the markings from glass pipettes, so exercise care when transferring MeCl.
10. Flush system with N_2 gas, using the N_2 tank and hose and the N_2 filled balloon. Lift the glass stoppers from the dropping funnels slightly to purge excess air. Make sure the N_2 valve remains open.
11. Stir PEG solution on the stir plate at ~5.
12. Start reaction by dropping the FuCl and TEA at the same rate of 1 drop per ~3-4 seconds. A slower drop rate will result in a more efficient reaction.
13. Reaction will turn dark brown.
14. When necessary, siphon melted water from the ice bin, and replace the ice.
15. When dropping is complete, allow the reaction to continue on ice for the rest of the day.
16. When necessary, siphon melted water from the ice bin, and replace the ice.
17. At the end of the day, remove the ice bin, remove the dropping funnels, and replace the funnels with glass stoppers.
18. Allow the reaction to continue at room temperature with stirring on a cork ring for at least 2 days.
19. Check the N_2 balloon over the next 2 days, and refill the balloon if necessary (close valve when refilling the balloon).
20. Glassware can be dried in the hood, and cleaned with acetone and the base bath.

Rotovaporing of MeCl

Warning: Use nitrile or silver-shield gloves when handling MeCl.

1. Wash and dry:

   1 x 1000 ml round-bottom flask,

   1 x glass funnel.

2. Turn on Rotovapor by switching Vacuum Controller V-800, Rotovapor R-200, and Vacuum V-500 on.
3. Fill the water bath with distilled H2O, and heat to 40°C.
4. Use the circulating pump to flow cold, ice water through the condensing tube.
5. Use the funnel to pour the OPF solution into a 1000 ml round-bottom flask.
6. Clamp and vacuum grease the flask to the Rotovapor.
7. Lower the flask into the water bath, so the OPF solution and water levels are the same.
8. Slowly rotate the flask in the water bath.
9. Turn on the vacuum on at 850 mbar ("Set" → Up or down → "Run").
10. Gradually decrease the vacuum as necessary to maintain a steady drip of condensation into the collecting flask. Vacuum can be decreased as low as 700 mbar.
11. When OPF/MeCl solution is thick and "stew-like" consistency, remove OPF from Rotovapor.
12. Dispose of the MeCl waste in the chlorinated organic solvents waste container.
13. Glassware can be dried in the hood, and cleaned normally.

Wash in Ethyl Acetate

Warning: Use nitrile or silver-shield gloves when handling ethyl acetate.

1. Wash and dry:

   2 x 2 L aspiration flasks, 1-2 x 2 L Erlenmeyer flasks, 1-2 x 2 L beakers,

   2 x Buchner funnels, 1-2 x glass funnels, 1 x stir bar, 2 x spatulas.
2. Add ethyl acetate (EA) to the OPF solution until the flask is ~2/3 full.
3. Stir the solution while heating with the heatgun (low speed, med heat) for 15-20 min, rotating every 5 minutes.
4. Solution will become less viscous and salts become visible at the surface. Ethyl acetate is a solvent for the OPF, but not for the salts produced in the TEA reaction.
5. Connect the vacuum and filter the solution through a Buchner funnel with #1 Whatman filter paper (11 μm pores) into a 2 L aspiration flask.
6. The salts will be filtered out of the solution by the filter paper. Discard these salts.
7. Add EA to the OPF to a total volume of 1500-1700 ml.
8. Stopper the flask with a #9 rubber stopper and parafilm the stopper and aspiration neck, and place the flask into the -20°C explosion-proof freezer for at least 2 hours or overnight if necessary.
9. If necessary, clean glassware for the next step.
10. After cooling, remove the OPF/EA from the freezer. The decreased temperature alters the solubility of the OPF, causing the OPF to precipitate out.
11. Connect the vacuum and filter the solution through a Buchner funnel with #1 Whatman filter paper, capturing the OPF in the filter paper and pulling the EA into an aspiration flask.

12. While filtering, stir the solution, allowing the EA to be pulled through the filter paper. Discard the EA.
13. When nearly dry, transfer the OPF from the filter paper to a beaker.
14. Add 1 L ethyl acetate to the solution.
15. Stir the solution while heating with the heat gun to redissolve the OPF in the EA. Solution goes from light brown to dark brown and becomes less viscous.
16. Use a clean glass funnel to transfer the OPF and EA to a 2 L Erlenmeyer flask and add EA to a total volume of 1500-1700 ml.
17. Stopper the flask with a #10 rubber stopper, and recrystallize the OPF/EA solution in a 2 L aspiration flask at -20°C for 1.5 hours or overnight.
18. Dispose of the EA waste in the nonchlorinated organic solvent waste container.
19. After cooling, filter the solution through a clean Buchner funnel with #4 Whatman filter paper (20-25 μm pores), capturing the OPF in the filter paper and pulling the EA into an aspiration flask.
20. The second filtering step may proceed much more slowly than the first. If EA/OPF is solid after removing from the freezer, add more EA to the solution. Tape 2 spatulas together to scoop product from the bottom of the flask.
21. Dispose of the EA waste in the nonchlorinated organic solvent waste container.
22. Optional: Repeat steps 13-19 for a third filtering step. This may be necessary if OPF appears too dark.
23. Dispose of the EA waste in the nonchlorinated organic solvent waste container.
24. Glassware can be dried in the hood, and cleaned normally.

Wash in Ethyl Ether

Warning: Use nitrile or silver-shield gloves when handling ethyl acetate and/or ethyl ether.

1. Wash and dry:

   1 x 2 L beaker, 1 x stir bar, 1 x Buchner funnel, 2 x PTFE coated jars.
2. When OPF is nearly dry and EA is mostly gone, add 1 L ethyl ether (EE) directly to the funnel to remove the EA.
3. Once mostly dry, transfer the OPF from the funnel and filter paper to a 2 L beaker.
4. Add 1 L ethyl ether (EE) to the OPF for a second wash with stirring.
5. Filter the solution through a Buchner funnel with #4 Whatman filter paper (20-25 μm pores), capturing the OPF in the filter paper and pulling the EE into an aspiration flask.
6. Optional: Add EE to the OPF for a third wash.
7. As the EE filters through and the OPF dries, use a spatula to break up any clumps of OPF.
8. By the end, you should have a fine powder that is mostly dry.
9. Scoop the OPF powder evenly into 2 Teflon-coated jars with the spatula.
10. Leave the OPF in the hood overnight with the lid on loosely.
11. Dispose of the EE waste in the nonchlorinated organic solvent waste container.
12. Glassware can be dried in the hood, and cleaned normally.

Vacuum Dry OPF

1. Clamp a lyophilizer tube to the scaffolding in the back of the fume hood as shown:

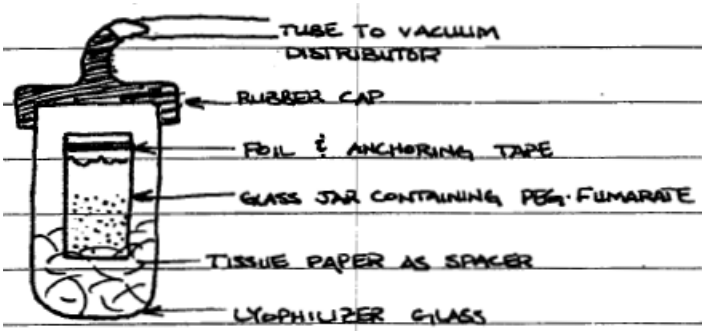

2. Tape aluminum foil to the top of the OPF jars and poke holes in the foil with a small gauge needle.
3. Add liquid nitrogen to the solvent trap.
4. Connect the vacuum to the solvent trap.
5. Close the valves to the samples (3rd and 4th from the top). Open the valve to the manometer (bottom).
6. The top 2 valves are open to the atmosphere and should remain closed.
7. Turn on manometer, and then the vacuum pump.
8. Once a vacuum is established, gradually open the valves to the samples. Open the valve to the first sample until a vacuum is established, then close that valve. Then open the valve to the second sample until a vacuum is established. Now you can reopen the first sample.
9. Pressure should be less than 10 mbar (preferably 1-2 mbar).
10. Check the pressure and the liquid nitrogen level every 30-45 minutes.
11. Refill the liquid nitrogen if necessary.

12. When OPF is dry and you cannot smell any EE in the powder, open the valve to break the vacuum and turn off the pump.
13. Dispose of solvent from the solvent trap.
14. Parafilm OPF and store it at -20°C.

Verify Product

1. A lighter brown color is preferred.
2. Polymerize a 100% OPF hydrogel with thermal and photo-initiation to test crosslinking.
3. Run GPC on the OPF in chloroform to verify molecular weight.

C.2. PEG-DA Synthesis

Reaction Calculations

1) Begin with **24 g PEG, MW 3400**.

2) React with 100% excess acryloyl chloride (AcCl; 2 AcCl:1 PEG).

24 g PEG / (3400 g/mol PEG) = 7.06 mmol PEG

7.06 mmol PEG * 2 end groups * 2 (100% excess) = 28.24 mmol AcCl

0.02824 mol AcCl * 90.51 g/mol / (1.114 g/mL) = **2.294 mL AcCl**

3) React with 1:1 AcCl:triethylamine (TEA)

0.00706 mmol PEG * 2 end groups = 0.0141 mol TEA

0.0141 mol TEA * 101.9 g/mol / (.726 g/mL) = **1.982 mL TEA**

4) Workup with anhydrous potassium carbonate (K_2CO_3)

0.02824 mol AcCl * 2 mol K_2CO_3/mol AcCl / 2 M K_2CO_3 = **28.2 mL 2M K_2CO_3** (aq)

138.205 g/mol = 276.41 g in 1L = 27.641 g in 100 mL = 8.2923 g K_2CO_3 in 30 mL ddH_2O

Day 1 – Methylene Chloride Distillation

Distill MeCl following the instructions in the OPF synthesis protocol. Keep in mind that you only need approximately 100 mL. Distillation is necessary to remove aqueous contamination (make MeCl anhydrous) that might generate unwanted side reactions in Day 2.

Day 2 – Reaction

What's going on? PEG is being acrylated. TEA acts as a catalyst by sequestering HCl to allow the reaction to proceed to completion. MeCl is the solvent used for this reaction.

Caution: AcCl doesn't smell as bad as FuCl, but it is worse for you (eye, throat irritant)!

Equipment:	
1x 500 mL 3-arm round bottom flask	1x balloon
1x dropping funnel	Glass pipettes
1x PTFE gas valve	1x stir plate
3x glass stoppers	1x clamp
1x glass stopcock	6x green clamps
1x PTFE stopcock	
	Chemicals:
1x stirbar	MeCl (anhydrous)
1x glass funnel	PEG
1x graduated cylinder	TEA
	AcCl

1. Set up 3-arm round bottom flask in the fume hood on a stir plate. Weigh and add PEG to the flask. Add stirbar.
2. Attach one dropping funnel, with a glass stopper, and a PTFE valve for N_2 gas flow. Vacuum grease glass-glass connections for the dropping funnel (excluding glass stopper) and the PTFE valve. Do not grease the PTFE valve itself.

3. Hook up N_2 tubing to the valve. Continually purge the whole system as you add 40 mL MeCl to the round bottom flask through the ungreased arm using a glass funnel. Stir. Gently float a glass stopper in the arm on the air being pushed out.
4. When dissolved, use a glass pipette to add TEA. Vacuum grease a glass stopper and gently float the dropping funnel's glass stopper as before. Let stir for 5 min.
5. Use a glass pipette to add 20 mL MeCl and the appropriate amount of AcCl to the dropping funnel. Be aware that MeCl (and its fumes) will remove markings from glass pipettes. Vacuum grease and stopper the funnel while you are adding and turn off N_2 flow.
6. Remove the N_2 hose and attach an N_2 balloon.
7. Drip the AcCl/MeCl mixture into the round bottom flask (about 1 drop every 3-4 seconds). Drip AcCl in MeCl very slowly (about 1 drop every 4 seconds).
8. After dripping is complete, you can replace the funnels with stopcocks.
9. Let stir overnight.

Day 3 – Workup

What's going on? To remove TEA-HCl, we first react the mixture with potassium carbonate to produce KCl, which will transfer to the aqueous phase. Some TEA will remain in the organic phase for Day 3 filtration.

Equipment:
1x 250 mL separatory funnel
1x glass stopper
1x glass funnel
1x glass stopcock
1x ring clamp

Chemicals:
K_2CO_3, anhydrous

10. Use a glass funnel to transfer the mixture from the

round bottom flask to a separatory funnel with a greased stopcock. (Don't forget to close the stopcock prior to transfer. Also, remember to wipe vacuum grease from connections before pouring.)

11. Add appropriate amount of 2M K_2CO_3 to the separatory funnel.
12. Stopper funnel, hold vertically, and give it a quick shake or two. Immediately open the stopper to release CO_2. Repeat a few times.
13. Hold the separatory funnel horizontally, but with the tip tilted higher. One hand should hold the glass stopper, the other holding the stopcock knob up. Rotate vigorously, and open the stopcock periodically to release CO_2. Repeat until all gas is released. Solution should have the consistency of a milky-white emulsion.
14. Leave overnight. Place a beaker underneath to capture any leaked product.

Day 4 – Filtration and Drying

What's going on? We isolate the mixture from KCl in the aqueous phase, add $MgSO_4$ to remove any additional aqueous solution, and precipitate PEG-DA in ethyl ether. TEA should remain in solution.

Equipment:
2x 250 mL beakers
1x 1L aspiration beaker
1x 2-3L beaker
2x stir bars
2x Buchner funnels
Filter paper (fine pores, 42)

Chemicals:
$MgSO_4$, MeCl
Ethyl ether

15. Drain the two organic phases into a 250 mL beaker on a stir plate with stir bar.
16. While stirring, add $MgSO_4$ until the mixture goes from a lumpy consistency to a well dispersed mixture of powder and organic solvent. It should appear as opaque milk – if it doesn't look like milk, add more $MgSO_4$. Add ~20-40 mL MeCl to keep the PEG-DA in solution (may help to have a smaller bottle or beaker with MeCl). The goal

here is to add as little MeCl as possible to keep the solution saturated with PEG-DA. But, if you add too much, no sweat.

17. Prepare a Buchner funnel with aspiration flask and filter paper and pre-wet the filter paper with MeCl.
18. Pour the mixture into the filter and a clear liquid should be collected (containing PEG-DA). If the liquid is cloudy, filtration should be performed again. The vacuum will also begin to evaporate MeCl. Thus, you can elect to evaporate MeCl if necessary.
19. Prepare a 2L beaker with 1.7L ethyl ether and a stir bar. Pour in the PEG-DA solution and wait 10 min to precipitate PEG-DA.
20. Prepare another Buchner funnel with two filter paper sheets, and pre-wet with ethyl ether.
21. Filter to separate PEG-DA. If the filtrate is not clear, re-filter. Pound into bits. See an older grad student to measure your performance.
22. Dry under vacuum until no ether can be smelled (at least 5 hours). At least some of this vacuum drying must be performed immediately after filtration.
23. Store at -20ºC. Expected recovery is approximately 75%.

Note: If necessary, you may need to dialyze the resulting product to remove impurities. Use a 1000 MWCO dialysis membrane at 0.2 g/mL and lyophilize after dialysis.

C.3. Gel Permeation Chromatography

Safety Precautions:

You must be trained to use the GPC. See Peter for details.

You must wear, at the very least, nitrile gloves. Double glove. Change whenever you get chloroform on your gloves. You can also wear silver shield gloves.

Materials Needed

Chloroform – Chloroform for HPLC; > 99.8%, ethanol as stabilizer Fisher/C606-4

Main glass syringe – BD Multifit glass syringe, Luer-Lok; 2cc

Needles – 18 gauge

Filters – BD Puradisc 25mm PTFE 0.45μm filters Fisher/14-823-10A

Vials – 1.5 mL vials with septa Fisher/03-391-9 (vials)

Fisher/03-391-32 (septa)

Clean rinse/waste beakers

Overview of GPC Setup

- When not being used, pump is always set at 0.1 mL/min.
- Samples are 5 mg/mL; injection volume 50 μL; run time 15 minutes; refractive index detector.
- Flow rate during use is 1 mL/min. Maximum pressure is 500 psi, set to 450 psi via software.
- All samples should be run in triplicate (excluding standards).

Initial Preparation

- Use 5 standards with molecular weights around your estimated range.
- Sample concentration should be around 5 mg/mL. Final sample volume should be 1-2 mL (5-10 mg). 300 μL is the absolute minimum.
- Make sure you have enough chloroform in the supply bottle.
- Record all requested information in the log book.

Set up the GPC while you are preparing your samples.

GPC Operation

Starting Up

1. If instruments are turned off, turn them on with the CBM module last.
2. Purge the autosampler. If you just turned it on, get the large glass syringe and hook it up to the small loose tube at the bottom of the autosampler. Use the controls to turn the manual purge on and let the autosampler pump 5-10 mL into your syringe (you don't need to pull). Dispose of the chloroform in a waste container in the hood.
3. Create a folder on the Desktop to store your data. Each run must have its own folder.
4. Click EZStart 7.4 on the Desktop. You should hear a machine beep indicating a successful CBM connection. If not, turn off all instruments and reboot the computer.
5. Ramp up the flow rate to 1 mL/min over 10 minutes.
    a. Select **File > Method > Ramp Up Revised.met**
    b. Select **Control > Single Run**
        i. Sample ID: **Blank**

ii. Data file: **Ramp Up**

iii. Data folder: **Your data folder**

iv. Vial number: **-1** (will not inject a vial)

v. Injection volume: [not important; either **0 µL** or **50 µL**]

c. Select **Start**.

d. Pressure should gradually increase (~270 psi). Record the maximum pressure in the log book.

e. At the end of the run, the flow rate should stay at 1 mL/min.

f. If the oven is not on, turn it on (green light under "Oven" on CTO-20A) by pressing **Oven**.

g. If the system beeps, and the UV detector screen complains of "Low Set Temp," this is normal. Using the software, choose **Control > Instrument Status**, and click **Clear Error**.

6. Load the standard method and save.

a. **Select File > Method > Open Standard Waters Method.met**

b. **Select File > Method > Save As**. Save the method in your own data folder with a unique name.

c. Select Method > Instrument Setup… > Download Method.

7. Balance the RID.

a. Click **Flow (Det. B)** on the EZStart toolbar (second row). The image looks like a spigot, and the "R flow" light will appear on the RID.

b. Wait 5 min and click **Flow (Det. B)** again to turn it off.

c. Repeat a-b 5 times (~25 mins total).

d. Flow should be off before you continue.

e. Click **Balance (Det. B)** and watch the RID-10A detector readout. The detector readout will go positive, negative and then suddenly zero. Repeat until Balance values are near zero. If you have to balance more than 3 times, see Peter.

8. Click **Zero (Det. A)** and **Zero (Det. B)** to zero both detectors.
9. It is suggested at this time that you start repeating blanks until the baseline stabilizes. Repeat step 4 with your method, monitoring the baseline drift until it stabilizes. You may need to balance or zero the detectors before you actually run your samples.

   a. Data file: **Blank 1, Blank 2, etc.**

   b. Vial number: **1**

   c. Injection volume: **50 µL**.

Preparing Samples

First steps

1. Weigh out all your samples (5-10 mg).
2. Fill your rinse beaker with around 100-200 mL chloroform.
3. Rinse the 2 mL syringe 3x with chloroform, dumping used chloroform into the waste beaker.
4. Add the appropriate amount of chloroform to all your samples.

For each sample

5. Pull up approx 1.5-2 mL of the dissolved solution. Deliberately withdraw air to prevent squirting.

6. Invert the syringe, remove the needle, attach a PTFE filter and push the filtered solution into an unused, labeled 1.5 mL vial.
7. Remove filter, attach another needle, and rinse the syringe 3x with chloroform.
8. Make a blank vial with filtered chloroform as the first vial in your sequence.
9. After your last sample has been filtered, separate the two parts of the syringe for storage. Let syringe evaporate in the hood before storing.
10. Load the autosampler tray with your samples. Make careful note of your loading sequence.

Setting up samples

1. Select **File > Sequence > Sequence Wizard...**
    a. Method: **The one you just created** (should be selected)
    b. Sample ID: Leave blank
    c. Data Path: Select your **data folder**
    d. Data File: Leave blank
    e. Number of unknown runs: **Number of vials in the autosampler**
    f. **Check** the "Create a line for each repetition" checkbox.
2. Click **Next**.
    a. Unknown vials of sequence – Start: **1**. Increment: **1**.
    b. Autosampler injection volume: **50 µL**
3. Click **Next** twice to bypass the calibration and summary windows.
4. Click **Finish**.
5. A new "Sequence" window should be visible. For each vial, edit both the **Sample ID** and the **File Name** fields for each sample, labeling what is what. Tip: Name standards

like so: ***S009601*** where *00960* is the molecular weight (M_p), and 1 is the repetition (see next step). Copy your sample ID over to the File Name field.

6. For long runs, run the standards again at the end to look for drifting. You can do this by adding additional entries in the sequence.
7. Add a few blank samples to the beginning. You can make the system repeatedly sample the first vial.
8. Add a **Ramp Down** run:
    a. Method: **C:\EZStart\Projects\Default\Method\Ramp Down.met**
    b. Data file: **Ramp Down.dat**
    c. Vial: **-1**
9. Similarly, add a **Shutdown** run:
    a. Method: **C:\EZStart\Projects\Default\Method\Shutdown.met**
    b. Data file: **Shutdown.dat**
    c. Vial: **-1**
    d. Run Type: **Shutdown**
10. Save your sequence in your data folder by selecting **File > Sequence > Save**.
11. Choose **Control > Sequence Run**. The sequence and method files should be already loaded.
12. Click **Start**.
13. While the sequence is running, you can change the viewing axes. **Right click** the window and choose **Axis Setup**. You can also **drag and select** a section of the chromatogram to look at. To zoom back to your original axes, just **double click** the window.

14. You can also simultaneously view previous data. To do so, **right click** the window and choose **Add Multiple Traces**. Select your files and click **Add**, then change each entry from SPD-20A to **RID-10A**.
15. To stop the run suddenly, click the **Stop** button on the toolbar.
16. If you need to run additional samples, you can create a new sequence file using the EZStart Offline program, add additional vials to the autosampler tray, and use Control > Sequence Run… to load your sequence. Clicking "Submit Priority" will implement your new sequence in the middle of the original sequence – after the currently running one, your new sequence will go, and then it'll finish the first sequence afterwards. Pretty neato…

Shutting down

1. If you have data that you didn't put in your own data folder, it will be in **C:\EZStart\Projects\Default\Data**. Move any relevant data inside there to your own folder.
2. Make sure the oven is not active (press the **Oven** button if light is on).
3. Dispose of samples/waste in the chlorinated solvents container. Let glassware evaporate overnight.

Analyzing data

Notes:

- You can only analyze one data file at a time.
- Make sure to select **RID-10A** at the top of the screen or else you will be analyzing irrelevant data.

- Sometimes the software will look like it's set to RID-10A when it's not. Periodically flip between an SPD channel and the RID-10A channel if your clicking doesn't look like it's doing anything.

1. Open **EZStart Offline** on the desktop.
2. Open your method.
3. Select the **RID-10A** channel (toolbar).
4. Select **Method > SEC Setup**. Check the box to enable **GPC/SEC Analysis**.
    a. Make sure it is **Narrow** calibration, **Linear** curve fit, Time slice **1 sec**.
5. Load the standard curve.
    a. For each standard, open its data file.
    b. At the bottom of the screen, there are a number of buttons. Choose **SEC Peaks**. Select the beginning and end of the peak with the mouse, and click **OK** to enter that peak into the SEC Setup window.
    c. Repeat for each data file.
    d. Enter the molecular weights (M_p) into the SEC Setup window for each time point.
    e. Save the method.
6. Process your standards.
    a. Open your sequence file. Save as a different sequence name e.g. "Sequence 2."
    b. Delete all entries except for your standards. **Save** your sequence.
    c. Select **Sequence Menu > Process**.
        i. Make sure **Print Method Reports** is **checked**.
        ii. Click **Start**.

iii. Make sure your filenames are correct as they save (remove **Z:\My Documents** from the first file name).

iv. Repeatedly click **Save** each time the dialog box comes up.

7. Load the baseline and result range and analyze your data.
   a. Open each data file.
   b. Select the result range.
      i. Select **SEC Result Range** (from bottom toolbar) and click tightly around the entire peak.
      ii. Choose a baseline that is ± ~30 sec around your result range (your choice).
      iii. Click **OK** to enter the result range into the SEC window. You might want to check the RID-10A channel is properly selected.
   c. Select **Analyze** on the toolbar (blue button in the middle).
   d. Select the **Print button > Reports > Method Custom Report**. Give a meaningful file name.
   e. Repeat for each data file. Reuse/remove baselines/result ranges as necessary.
8. Combine all the PDFs into one using your tool of choice. M_n and PI are what you are looking for, by the way. In Adobe Acrobat Professional:
   a. Select **File > Create PDF > From Multiple Files**
   b. Choose your files.
   c. **Drag** the files in order of the run.
   d. **Save** your new PDF.

C.4: Acrl-PEG-NHS/MMP Peptide Conjugation

Purpose: To attach PEG-acrylate to each end of an MMP-cleavable peptide.

Materials:

Plastic conical vial, 200-250 mL beaker, 2-3L beaker, stir plate

Acrl-PEG-NHS (SVA) [MW: 3400 Da]; MMP cleavable peptide [MW: 769.86 Da GGGLGPAGGK]

Dialysis tubing (3500-5000 Da MWCO; Spectrapor 131201/131204) and clips

Preparation:

1) Wash glassware and dialysis clips (Alconox, water, dH_2O)
2) Make a 50mM sodium bicarbonate buffer solution and pH to 8.5. For reacting 100 mg peptide, this means 420 mg sodium bicarbonate in 100 mL ddH_2O in the 200-250 mL beaker. Shield your beaker from light.
3) Calculate amounts of Acrl-PEG-NHS (2.2:1 moles of NHS to peptide) needed for cleavable peptide. For 100 mg peptide, you need 971.6 mg Acrl-PEG-SVA.

Reaction:

4) Dissolve the peptide in 20% of your buffer in a 15 or 50 mL conical (100 mg in 20 mL).
5) Dissolve the Acrl-PEG-NHS in the buffer that's left in your beaker (971.6 mg in 80 mL). The beaker should be shielded from light.
6) Immediately add peptide solution to your beaker, stir (~6) and cover with parafilm.
7) Allow to stir for 3-4 hours at room temperature.
8) Prepare tubing for dialysis. Each (super-wide, 131204) strip should hold as much

solution as possible. 100 mg peptide = 100 mL buffer = 3-4 tubes usually.

9) Rinse dialysis tubing 4x in a 2L beaker, 15 min between each rinse, to remove sodium azide.
10) Close one end of each dialysis strip with a weighted closure. Due to potential leakage, fold over the tubing before sealing with the closure.
11) Use a transfer pipette to add the solution to each tube. Close the open end of the tubing with a non-weighted closure and fold over the tubing before sealing, similar to step 10.
12) Dialyze to remove byproducts for 2 overnights. If starting on the morning of the first day change the water the morning and night of the second day. Keep from light.

Lyophilization:

13) Transfer solution from tubes to vials, with approximately 12-13 mL per scintillation vial.
14) Remove the caps from the scintillation vials and place aluminum foil over the tops and tape this foil down. Poke holes in the top of the foil with a needle to let air escape.
15) Freeze vials in liquid nitrogen and lyophilize the product for 2 overnights.
16) Combine all powder into one scintillation vial, preweighing the vial so that the mass of the product inside the vial can be determined.
17) Parafilm and store the resulting product at -20°C.

C.5: Cell Encapsulation

Purpose: Gels will be created with cells incorporated in them.

Materials:

Media (prepared day before)

Sterile PBS

15 and 50 mL conicals as needed

3 and 10 mL syringes, with one 18G needle for each.

1 mL syringe

Sterile filters

12-well plates

Sterile containers for your gels (Teflon molds, or other molds)

Spatulas, sterilized

The day before your encapsulation

1. Combine the polymers desired in a scintillation vial. You can freeze this vial down until the day of encapsulation. Note: You will lose about 200-300 μL due to sterile filtration, so adjust accordingly by making a gel that requires 300 μL more than the PBS you would have added to your polymers.
2. Sterilize Teflon molds and spatulas as required. Always a good idea to have extra.
3. Make sure you have enough sterile filters and other items for your encapsulation.

Day of encapsulation

Polymer side

4. Warm up your polymer powders, trypsin, and your media.

5. If doing a thermal encapsulation, create 0.3 M stock solutions of APS and TEMED in scintillation vials as you would normally.
    a. APS: 684.6 mg in 10 mL PBS
    b. TEMED: 0.348 g (~350 µL) in 10 mL PBS
6. Add sterile PBS to each vial according to your calculations and vortex.
7. Let the solutions sit at 37 °C for at least 30 min in order to remove bubbles.
8. Filter sterilize APS and TEMED solutions (if you're using them) into 15 mL tubes. Make sure to cover the tubes with aluminum foil to prevent photoinitiation.
    a. Open the packaging of a syringe filter, but leave the filter in its container.
    b. Attach a needle to a 10 mL syringe, and draw up the contents of a scintillation vial.
    c. Invert the syringe and remove the needle.
    d. Grip the sides of the filter container, and screw the syringe onto the filter.
    e. Filter into an open 15 mL tube.
9. Prepare the UV lamp and warm it up if you're doing a photo encapsulation.
10. Place sterile, autoclaved molds into petri dishes (one mold per dish).
11. Filter sterilize your prepolymer mixtures. **Tip:** For a gel less than 1 mL, use a 3 mL syringe, then after pulling up the gel, pull up additional air. The air helps with sterile filtering.
12. Transfer the correct amount of gel to a separate 15 mL tube.
13. Place your sterile spatulas.
14. Prepare and label your 12-well plates.

Important note: At minimum, steps 4-11 **must** be completed before the actual encapsulation itself.

Cell side

15. Rinse your flasks twice with PBS, and trypsinize your flasks as normal.
16. While you count your cells, spin down the cells in the centrifuge. **Caution:** Before you spin down the cells in this step, make sure steps 4-11 are done.
17. Aspirate the media off the cells, then resuspend the pellet in sterile media, typically at a concentration of $50x10^6$ cells/mL.

- Amount of media to resuspend in µL = # of cells/desired concentration x 1000
- e.g., with 10,000,000 cells total, then 10e6 / 50e6 x 1000 = resuspend my cell pellet in 200 µL of media.

Crosslinking/encapsulation

18. Add cell solution according to your calculations and quickly mix with the pipette (do **not** vortex). If the cell solution has a concentration of $50x10^6$ cells/mL and you used the standard gel calculator, this will give a final solution of $10x10^6$ cells/mL.
19. If doing a thermal encapsulation, add APS according to your calculations and mix with pipette. Then, add TEMED according to your calculations and mix with pipette.
20. If doing a photo encapsulation, add sterile D2959 to your solution and mix with pipette.
21. Deposit the appropriate amount of the resulting solution in your molds. The standard is 30 µL of gel in a 1.0-mm Teflon mold well.

22. Cover petri dish and place it in the incubator for 10 min for thermal polymerization; leave under lamp for photo polymerization.
23. Aliquot 2 mL media into each well of a 12-well plate, depending on how many gels you have.
24. Remove from the heat and carefully move the gels into the 12-well plate using a sterile spatula. Put the 12-well plate into the incubator.
25. Repeat steps 17-26 as necessary with other polymer solutions.
26. Recommended: Change media one hour after encapsulation.

C.6. Tensile Culture System

Introduction

The tensile culture system allows you to culture 24 hydrogel constructs at a time. Separate platforms exist for purely static culture and dynamic tensile culture. Each construct is connected to two porous polyethylene "endblocks," which are then pulled on by metal rakes connected to a linear actuator. A dedicated computer system, with a large control box and laptop with a serial port, is used to control the actuator movement and must be placed by the incubators for constant control.

Components

- Static strain and dynamic strain platforms
  - Static strain – adjust the distance of the rake by rotating the screw itself.
  - Dynamic strain – control via computer and STARTUP protocol sequence.
  - For cell culture, place dynamic strain platform on the bottom level of upper right incubator. The static system can go above it.

- Computer control modules
  - Laptop has a Dell power cord and a serial cable that connects to the control box.
  - Control box has a power cord and two cables that are connected to the dynamic strain platform.
  - Place both of these above the upper right incubator.
- Acrylic platform covers and isolators
  - All these pieces can be sprayed with ethanol, but don't autoclave them.
  - Static platform cover; no holes. Requires both trays to be installed to close properly.
  - Dynamic platform cover; one hole for the actuator and cables.
  - Dynamic platform temporary cover; two holes on both sides for the actuator as well as the second rake. Use when you're done with the first rake and you're working on the second one.
  - Tray isolator (2); place on trays when you want to keep them sterile.
  - Partial tray isolator; place on the portion of the tray under the rake when you want to work on the rake itself.
- Construct wells or trays
  - All autoclavable, etc.
  - Static well trays (2); mostly opaque; rakes do not lock in as well as the trays are a little lower.
  - Dynamic well trays (2); white wells.
- Rakes and mounts

- Keep at least two rakes attached to their mounts. Check holes are centered and aligned before you screw anything down.

❖ Screws

- Check whether the screws are stripped – both ways – before you use them in culture.
- Autoclave a few at a time in a sterile package.
- Long Allen hexagonal screws; used to screw in trays to their respective platforms, as well as rakes to their respective mounts.
- Short Allen hexagonal screws; used to screw in mount/rake assembly to the actuator.

Setup

1. Set up the hood.
2. Place dynamic system in the hood; the control box and computer go above the incubators.
3. Hook up all cables, then turn all systems on.
4. Make sure all indicators are indicating ready
    a. LinMot module has solid green READY light (blinks twice when system is not initiated)
    b. Reinshaw linear encoder is green (indicates sensor is properly obtaining a value) and detects reference point (turns red briefly)
5. Make sure to lubricate all parts (rail and linear motor) before each run
6. Open the Motion Perfect 2 software.

7. Open the terminal window (click terminal icon) and select terminal 0.

Note: Do **not** screw rake into place before running the setup program. It involves the retraction of the linear motor all the way to the retract position which could break the tray, the rake, the motor or all three.

Calibration

1. Run STARTUP_1
2. Use the following parameters: *choose system 1*

Note: Offset value should be adjusted to optimize the rest position of the rake before each run.

- *Offset is ~4.2 for a 15.4mm gel (50:50, OPF-3k, 0.018M thermal, 75 wt%)*

Assembly

You'll need one or two grippy tweezers, and one of those long tweezers with a curve at the end.

1. Screw each tray down, placing a tray cover on top.
2. Remove the tray cover of the inner tensile tray (closest to the motor) and add 2 mL media into each well.
3. Place a hydrogel into each well. Once hydrogels have been placed in each well, move them onto the plastic peg of each well. Align them properly, then add ~1 mL after they are in place.
4. Place rake into place by carefully pressing each of the rods into the endblock holes. Screw down lightly to the motor actuator.
5. If you want to check alignment and movement, run a quick INTERMITTENT program with 10 or 20 cycles, so you can see

6. Cover the current setup with the temporary cover, then add media and hydrogels to the outer tensile tray.
7. Cover the inner portion of the outer tensile tray with the partial tray cover.
8. Place rake into place by carefully pressing each of the rods into the endblock holes.
9. Screw rake onto the holding plate mount. (4 screws)
10. Ensure that all trays are aligned and centered; small misalignments can translate into serious problems. If you need to check alignment and movement, run another INTERMITTENT program with 10 or 20 cycles.

Running

1. Run INTERMITTENT
2. Choose system 1
3. Choose amplitude
    a. Gels will be stretched 2x amplitude. For example, an amplitude of 3 stretches gels from 0 to 6 mm.
4. Choose frequency
5. Choose mode: intermittent, continuous, or number of cycles
    a. Intermittent
    b. Continuous
    c. Number of cycles

When feeding, remove approximately 2 mL and replace with another 2 mL fresh media.

Notes:

- *Make sure to keep enough PBS or any media buffer filled in each of the wells of the system during each run. Failure to do so will result in drying out and premature breakage of the hydrogels.*
- *Program always starts and ends at offset set by startup.*
    a. *An offset of 4.35 corresponds to 0% strain on a gel 15.61 mm long with 9.5 mm endblocks.*

Important Commands:

TO STOP IMMEDIATELY – vr(1) = 0 then **ENTER.**

TO STOP SERVO only – servo1 = 0.

TO restart servo – servo1 = 1.

TIP: If in the case that the run command is stopped or the servo is stopped, the system can be reset by running a short cycle through INTERMITTENT.

Some commands

- mo(#): Relative move. Moves rake by #. Positive numbers indicate compression. Negative numbers indicate tension.
- ma(#): Absolute move. Moves rake to # on absolute scale. Positive numbers indicate compression. Negative numbers indicate tension.
- Defpos(#): Define position. Defines current position as # on absolute scale.

C.7: Confocal Microscopy

Notes

- **You must be trained to use the confocal microscopes.** Email steve.woodard@ibb.gatech.edu for the next training session.
- There are three scopes that you can use:
    - LSM 510 UV, in room 1328. This is what we call "the old scope."
    - LSM 510 NLO, in room 1326. This is what we call "the multi-photon" confocal microscope.
    - LSM 510 VIS, in room 1326. This is currently the preferred scope.
- Make sure to reserve a spot on the confocal microscope up to one week in advance at http://www.ibb.gatech.edu. You will need to make an account there if you haven't already.
- These instructions are for the LSM 510 VIS.

Materials Needed

- Bring a box containing gloves and your samples.
- When working with gels, bring additional equipment:
    - Attofluor cell chamber and round glass coverslips
    - PBS squirt bottle ("PBSi", also known as PBS + ions)
    - Spatulas and tweezers as necessary, plus kimwipes for any spills.

Setting Up

1. Turn on the two switches to the left of the microscope – turn these on if needed, plus the computer.
2. At the login screen, hit Enter to login (Administrator/[blank password]).
3. Click on ZEN 2008, in the middle of the screen, and click Start System.

4. Adjust the workspace zoom using the slider on the upper right side of the screen. Use an existing preset or make your own, clicking the “open folder” or “save” icons to save or apply changes.
5. Turn the first two lasers on (488 must go to “standby” first, 543 is simply on/off). No need for 633.
6. Below the laser controls, open the Temenoff Lab setting. This is specially configured for Live/Dead imaging.
7. At the top of the second column, note the current objective being used.
    a. On the LSM 510 VIS, there are 10x, 20x and 40x air objectives. 10x is the most commonly used. 20x and 40x objectives give better magnification, but have less light exposure (and thus produce less bright images as a result).
    b. Two objectives, 40x and 63x objectives are oil-based.
        i. Select the objective using the software and place one drop of oil on the objective.
        ii. Mount your sample and raise the objective until it just touches and oil spreads out.
        iii. When you are done, wipe off the oil with lens paper, **not kimwipes**.
8. Note other settings for averaging images (usually 1, with more for 20x/40x objectives), the resolution of your images (preferred is 1024x1024), and make sure scan speed is set to “Max” (9).
9. Note your physical controls. To the right of the microscope is an X-Y controller. Below your monitor is a touchscreen with a coarse and fine control for controlling Z direction.

Preparing Samples

1. Prepare a sample for viewing.
    a. If you've got a plate, just place the plate on top and you are all set.
    b. To prepare for viewing a gel, place a glass cover slip on the bottom piece of the cell chamber. Screw both pieces together and squirt some PBSi into the chamber to keep the gel hydrated. Then load your sample into the circular grooves on the microscope platform.
2. Control your imaging using the Channels area in the 2nd column.
    a. Pinhole size refers to how much light is let through. Higher pinholes let through more light but will increase the amount of light captured in the Z-direction (that is, above and below your image). A preferred pinhole size is 1 AU (Airy unit, showing the lowest Z distance that will be captured). You can increase this if necessary.
    b. Detector Gain amplifies light received by the detector. Higher gain, brighter images, but also more noise. You should settle for a max of around 800 on both channels; sometimes you may even go below 700.
    c. Digital Offset eliminates light below a certain threshold. Use this to eliminate stray bright pixels.
3. Click Fast on the upper left hand of the screen to begin continuously scanning.
4. How to make images clear
    a. Something important is that imaging is **highly subjective** and depends on what you are looking for. Microscopy experts don't like saturating images, but our lab

usually tends towards that. Use your experience and be consistent in how you image, and things'll turn out fine.

b. Set the offset and gain on each channel to near maximum. Lots of noise should fill the screen.

c. To the left of the image, choose Split to separate the red and green signals.

d. Scan to where you can find cells. This can be done by moving up and down (using the focus knob on the side) or by xy translation. Look at where the laser hits the gel to determine where you are. For Z location, check the Z Stack section (lower right, 2nd column) for your height.

e. Below the image, there are colors indicating what is being shown. Click the colors below the "Merged" button to change the display to Range Indicator mode. Red mean oversaturation, blue means undersaturation, and black/gray is somewhere in between.

f. For each channel, you can use the Detector Gain and Offset controls to change how things look. You want just a tiny amount of red, and any spots NOT of interest should be totally blue. Eliminate as much noise as possible without losing areas of interest.

g. Exit Range Indicator mode and see how your images look. You may want to retweak as necessary.

h. Your calibration should be good for the rest of your wells/gels.

Taking Pictures

1. Taking single pictures

a. Use Fast to assist as you scan for areas of interest. When you find one, click Single in the upper left, then save the current image.
b. Images should be saved in D:\[your name] in .lsm format.

2. Taking Z stacks
   a. The Z Stack section is below Channels. Check the box to the right of the title to activate it (without it, the Start button in the upper left will be grayed out).
   b. Use Fast to select your bottom image (if imaging whole gel, start with a completely black image) and click Set First.
   c. Use Fast to select your top image and click Set Last, then click Stop.
   d. Make sure Keep Interval is selected. This will keep the z slice size constant, even if you later decide to change the # of slices or the upper and lower limits in your stack. Typically the slice size in our lab is set to 10 µm.
   e. Click Start. A scan will automatically begin. To view the images as they are being generated, click Gallery to the left of the image.
   f. Don't forget to save your Z stack (also in .lsm format).

Saving Data

Note: Do not expect your data to be backed up. It usually is, but there's no guarantee. We make it easy for you to save your data to the Temenoff lab drive.

1. Click Start > Run: \\zoe.bme.gatech.edu\temenoff-lab
2. When it asks for a username and password, give it your BME credentials.
3. The Temenoff lab server should now be mounted. Copy your images over as appropriate.

Cleaning Up

1. Lasers
    a. Shut down the Argon laser (or put it on Standby if you know someone else will use it).
    b. Shut down the HeNe laser (or leave it on).
2. If you need to shut down the system, give the lasers a few minutes to finish cooling (you should hear a noise stop in 2-3 minutes). Shut down the computer first, then flip both switches (the ones to the left of the scope) off.
3. If working with gels, rinse out the cell chamber and throw away the glass cover slip in biohazard glass trash. Wash the cell chamber with soap and distilled water and leave the individual pieces on the rack in the cell culture room to dry. Do not use ethanol; it dries out the rubber O-ring.

Working with Pictures

1. The free LSM 510 Image Browser (downloadable from Zeiss) can be used to view images. Pretty much the only reason you'd really need to use it, other than viewing pictures and exporting them to various formats, is the Projection feature.
    a. Select your Z stack and open it.
    b. Select Projection. Rotate around the Y axis, and choose the most projection images (64/panorama) to generate to ensure a smooth 3D projection.
    c. The created projection can be slowed and manipulated, as well as stored along with the database.
    d. This can also be exported to a movie file.

2. You can also use the image browser to create your own databases with custom images. Use the Copy and Paste functions in the toolbar.
3. You can also use the Zeiss ZEN LE software (essentially, ZEN without the microscope controls).
4. You can also use ImageJ, especially if you're not on Windows.

Confocal microscope settings

You can use the FITC/CY3 as an initial setting.

Below the imaging buttons, check Z-Stack.

Turn on the Argon and HeNe543 lasers. (Argon must go to standby first, and after a while you can set it to On. This is very important - don't forget to turn it off of Standby.)

Imaging Setup

Mode	Switch track every
Channel Mode	Frame

First channel name: Fluorescein 488-517 (FITC)

Second channel name: Rhodamine 543-600

Select the fluorescein channel.

Light path: To the left of laser, select HFT 488/543.

Above HFT 488/543, select NFT 545.

To the right of NFT 545, select BP 505-530, and check Ch2. Select green for Ch2.

Above NFT 545, select Plate.

Next on the path, select LP 560. Check Ch1 and select Red.

Select the rhodamine channel and perform the exact same steps.

Acquisition mode:

Objective	Scan mode	Frame size	Line step	Speed	Averaging
10x	Frame	Click X*Y 1024 x 1024	1	Click Max 9	1

Averaging isn't important unless you want to fiddle around with how it averages images.

Useful for poor visibility.

Channels: Fluorescein

Laser power	Pinhole	Gain	Digital offset	Digital gain
3.0	1 AU	1100-1200 set; 700-750 operating	> -0.10 set; -0.30 operating	1.00 operating

Channels: Rhodamine

Laser power	Pinhole	Gain	Digital offset	Digital gain
35.0	1 AU	1100-1200 set; 800 operating	> -0.10 set; -0.30 operating	1.00 operating

Z Stack: Rhodamine

Interval	Keep
10 microns	Interval

Use "Set First" and "Set Last" to specify the beginning and end of a stack.

Once all of this has been set up, click the Save icon near the Configuration name near the upper left corner, and save it under your own custom preferences.

C.8: PicoGreen Assay

Pico Green Preparation v1.3

Purpose: The Pico Green assay quantifies the amount of DNA present which is an indirect measure of the number of cells.

Materials:

12 well plates

Sterile PBS

Spatulas, sterilized

Tweezers, sterilized

96 well plates

For Gels

1. Remove media.
2. Add 2ml iPBS.
3. Remove iPBS.
4. Add 3-4ml iPBS
5. Place in incubator for at least 30 min. Leave in incubator until gels are no longer the color of the media and have become clear.
6. Transfer the gels between pieces of weigh paper to remove excess water and weigh the gels. Then put the gels in 1.5 ml eppendorf tubes.
7. Homogenize the gels with a pellet grinder in the tubes. Be careful not to loose any of the gel.
8. When the gel is well ground add ddH_2O to the tube depending on the size of the gel (750 µl for those cast in the caps). Some of the ddH_2O can be used to wash

the pellet grinder tip into the tube and to wash the side of the tube. This will maximize the amount of gel that is available for the bioassay.

9. Let sit at room temperature for 30 min.
10. Store at -20 °C if needed.

Lysing the cells

11. Freeze the cells at -80 °C for a minimum of 1 hour.
12. Thaw at room temperature for 30 minutes.
13. Sonicate for 30 min. to lyse the cells.

    Note: The sonicator will heat up after each usage. Ice should be added to the water in order to cool the sonicator down. If this is not done the DNA in the sample could break down.

    Safety note: The sonicator is meant to lyse the cells. Do not put fingers into the water bath while the sonicator is on or cells in your fingers will be lysed.

14. Repeat steps 11-13 two additional times.
15. If the samples are being stored before the assay is done freeze them at -80°C .

For Plated Cells in a well plate

1. Aspirate liquid from the wells of the plate
2. Add 2 ml PBS to rinse.
3. Repeat steps 1-2.
4. Add 1 ml distilled, deionized water (ddH_2O).

5. Let sit at room temperature for 30 min.
6. Store at -20 °C if needed.

Lysing the cells

7. Freeze the cells at -80 °C for a minimum of 1 hour.
8. Thaw at room temperature for 30 minutes.
9. Sonicate for 30 min. to lyse the cells.

   Note: The sonicator will heat up after each usage. Ice should be added to the water in order to cool the sonicator down. If this is not done the DNA in the sample could break down.

   Safety note: The sonicator is meant to lyse the cells. Do not put fingers into the water bath while the sonicator is on or cells in your fingers will be lysed.

10. Repeat steps 7-9 two additional times.

Making the plates

Standards

11. Make sure to thaw out samples and PicoGreen reagents for about 20 minutes before doing the assay.
12. Make up buffer solution and PicoGreen according to the PicoGreen calculator. Vortex both solutions to make sure they are mixed thoroughly.

    Note: When creating the buffer solution make sure to take the volume in the DNA standards into account. Also, cover the PicoGreen solution in aluminum foil to protect it from light.

13. Make up DNA standards according to the table below.

Conc. (ug/ml)	DNA (ul)	Buffer Solution
5	25	475
3	15	485
1	5	495
0.5	50 of 5 ug/ml	450
0.3	50 of 3 ug/ml	450
0.1	50 of 1 ug/ml	450
0.05	50 of 0.5 ug/ml	450
0.03	50 of 0.3 ug/ml	450
0.01	50 of 0.1 ug/ml	450
0	0	1000

14. Add 43 µl of your sample solutions into the appropriate wells of a 96 well plate. Make sure to change tips between samples.
15. Add 107 µl of the buffer solution into the wells.
16. Add 150 of the PicoGreen Solution to the wells.
17. Read in a plate reader: ex 485, em 528.

C.9. RT-PCR

Real-Time, Reverse Transcription Polymerase Chain Reaction (RT-PCR) Protocol

RNA Extraction

Extract RNA using Qiagen RNeasy Mini Kit

(Consult the RNeasy kit manual for more specific protocols depending on your cell/tissue source)

Materials

Molecular BioProducts RNase Away Spray (VWR 17810-491; 475 ml)

Aerosol Filter Pipette Tips for Rainin LTS, 20 µl (VWR 83009-688; pack of 960)

Aerosol Filter Pipette Tips for Rainin LTS, 200 µl (VWR 82003-196; pack of 960)

Aerosol Filter Pipette Tips for Rainin LTS, 1000 µl (VWR 82003-198; pack of 576)

QIAshredder (Qiagen 79654 or 79656; 50 or 250 runs)

RNeasy Mini Kit (Qiagen 74104 or 74106; 50 or 250 runs)

Optional Alternative: RNeasy Protect Mini Kit (Qiagen 74124 or 74126; 50 or 250 runs)

EMD 2-Mercaptoethanol (VWR EM-6010; 100 ml)

RNAse-free DNase Set (Qiagen 79254; 50 runs)

Protocol

For plated cells

I. Trypsinize cells and centrifuge (10 min, 1000 rpm).

II. Aspirate supernatant, resuspend pellet in media, and centrifuge (10 min, 1000 rpm).

III. Aspirate supernatant, rinse pellet with PBS, and centrifuge again (10 min, 1000 rpm), aspirate PBS.

For gels

I. Soak gels in PBS for ~ 1h to remove media.

II. Transfer the gel to an RNase free, DNase free microcentrifuge tube.

III. Break the gel into small pieces using a pellet grinder.

1. Lyse cell pellet or cells in gel in **350 µl Buffer RLT with β-mercaptoethanol** (add 10 µl BME per 1 ml Buffer RLT).
2. Put solution in **purple QIAshredder column** and centrifuge **(2 min, 14000 rpm)**.
3. Discard filter and add **350 µl 70% ethanol** to eluted substance.

4. Transfer suspension to **pink RNeasy column** and centrifuge **(15 sec, 14000 rpm)**.
5. Discard eluted substance and put filter back on. (Do NOT mix Buffer RLT or RW1 with bleach when discarding. Contact with acids forms highly reactive guanidine salts and liberates very toxic gas)
6. Add **350 µl Buffer RW1** to column and centrifuge **(15 sec, 14000 rpm)**.
7. Discard eluted substance and put filter back on.
8. Add **10 µl DNase I** (lyophilized DNase I is resuspended in 550 µl RNase-free water) to **70 µl Buffer RDD** for each sample.
9. Add **80 µl of DNase/RDD solution** directly onto RNeasy membrane and incubate at **room temperature for 15 min**.
10. Add **350 µl Buffer RW1** to column and centrifuge **(15 sec, 14000 rpm)**.
11. Discard eluted substance and put filter back on.
12. Add **500 µl Buffer RPE** (add 44 ml of 96-100% ethanol to starting 11 ml of Buffer RPE concentrate before first time use) to column and centrifuge **(15 sec, 14000 rpm)**.
13. Discard eluted substance and put filter back on.
14. Add **500 µl Buffer RPE** to column and centrifuge **(2 min, 14000 rpm)**.
15. Discard eluted substance and transfer column to new 2 ml collection tube.
16. Centrifuge **(1 min, 14000 rpm)**.
17. Discard 2 ml collection tube, and transfer column to new 1.5 ml collection tube with cap.
18. Add **30-50 µl RNase-free water** and centrifuge **(1 min, 14000 rpm)**.

19. The water elutes the RNA into the collection tube – cap the tube and store RNA at -80˚C.

Quantify and check purity of RNA

Materials

MP Biomedicals RNase, DNase-free water (VWR IC821739; 500 ml)

Corning UV Transparent 96-well plate (Fisher 07-200-623; pack of 25)

Protocol

1. In a UV-transparent 96-well plate, add 2 µl of extracted RNA and 98 µl RNase-free water to 3 wells (dilution factor = 50).
2. In 3 more wells, add 100 µl RNase-free water.
3. Take absorbance readings at 260 nm and 280 nm light.
4. Quantity of RNA can be calculated using the following equations:
    - Corrected A_{260} = average sample A_{260} – average blank A_{260}
    - Concentation in µg/ml = (corrected A_{260}) * (44 µg/ml) * (dilution factor)

      (using above protocol, dilution factor = 50)
    - Total mass in µg = (µg/ml concentration value) * (µl volume) / 1000

      (volume of RNA extraction sample; using above extraction protocol, volume = 30-50 µl)
    - Volume in µl needed for 1 µg RNA = (1 µg RNA) * 1000 / (µg/ml concentration value)

      (1 ng to 5 µg RNA can be used for Reverse Transcription)
    - Volume of water in µl needed = 10 µl total volume – RNA volume determined above

5. Purity of RNA can be calculated using the following equation:
    - Purity = A_{260} / A_{280}
    - This value should be between 1.5 and 1.9.

Reverse Transcription

Reverse Transcription with SuperScript III Reverse Transcriptase

Materials

Oligo(dT)$_{15}$ Primer (Promega C1101; 20 µg)

PCR Nucleotide Mix, 10 mM (Promega C1141; 200 µl)

SuperScript III Reverse Transcriptase (Invitrogen 18080-093 or 18080-044; 2000 or 10000 units)

Invitrogen RNaseOUT RNase Inhibitor, 40 units/ml (Invitrogen 10777-019; 5000 units)

Protocol

1. Add the following components to a nuclease-free PCR tube:
    - **1 ng to 5 µg total RNA: 10 µl**
    - **Oligo(dT)$_{15}$ (500 µg/ml): 1 µl**
    - **dNTP Mix (10 mM each): 1 µl**
    - **RNase, DNase-free water: to 12 µl final volume**
2. Heat mixture to 65˚C for 5 min and chill on ice for at least 1 min. Collect the contents of the tube by brief centrifugation and add:
    - **5X First-Strand Buffer (250 mM Tris-HCl, 375 mM KCl, 15 mM $MgCl_2$)**: **4 µl**
    - **0.1 M DTT**: **1 µl**

- **RNaseOUT (40 units/µl)**: **1 µl**

3. Mix contents of the tube gently. Incubate at 42˚C for 2 min.
4. Add **1 µl (200 units) of SuperScript III RT** and mix by pipetting gently up and down.
5. Incubate at 50˚C for 30-60 min.
6. Inactivate the reaction by heating at 70˚C for 15 min.
7. Store cDNA at -20˚C.
8. Amplification of PCR targets (>1 kb) may require the removal of RNA complementary to the cDNA. To remove RNA complementary to the cDNA, add 1 µl (2 units) of *E. coli* RNase H and incubate at 37˚C for 20 min.

Primer Preparation

Reconstitute primers (100 µM)

Materials

Custom Primers/Oligonucleotides, desalted (Invitrogen; 25 nmol)

Protocol

1. Find the total nmoles from the information sheet that came with the primer.
2. The volume of DNase-free water needed to create a 100 µM stock can be calculated using the following equation:
    - Volume of DNase-free water in µl = (nmoles of primer) *1000 / (100 µM)

Make 10 µM aliquots

Protocol

1. Briefly spin the primers and add the needed amount of water for a 10-fold dilution.

2. Make a 10-fold dilution (1 part primer: 9 parts DNase-free water) to obtain a 10 μM aliquot.

Polymerase Chain Reaction

Run PCR

Materials

SYBR Green Master Mix (Applied Biosystems 4309155; 5 ml)

Applied Biosystems StepOnePlus Real-Time PCR System and Materials

- MicroAmp Fast 96-Well Reaction Plates, 0.1 ml (Applied Biosystems 4346906; 20 plates)
- MicroAmp Optical Adhesive Films (Applied Biosystems 4360954; 25 films)

OR

- MicroAmp Fast 8-Tube Strips, 0.1 ml (Applied Biosystems 4358293; 125 strips)
- MicroAmp Optical 8-Cap Strips (Applied Biosystems 4323032; 300 strips)
- MicroAmp 96-Well Trays for Veriflex Blocks (Applied Biosystems 4379983; 10 trays)

Protocol

1. Thaw the following components on ice:
    - SYBR Green mix
    - 10 μM forward primer of interest
    - 10 μM reverse primer of interest
    - Sample cDNA

2. To make **Master Mix**, count the number of wells needed for each primer, add 2, and multiply this number by the following to obtain enough Master Mix for all wells of the primer:
    - **12.5 µl SYBR Green mix**
    - **10.5 µl DNase-free water**
    - **0.5 µl 10 µM forward primer**
    - **0.5 µl 10 µM reverse primer**
3. Load PCR wells:
    - Load **24 µl of Master Mix** into each well for that primer (target sequence of interest).
    - Add **1 µl of sample cDNA** into the well with Master Mix and mix by pipetting up and down.

      (change pipette tips between each well)
4. After all wells are loaded, cover with optical tape or caps, and put entire plate on ice until ready to run PCR.
5. Load plate into StepOnePlus system:
    - Load plate into machine (A1 in upper-left, H12 in lower-right).
    - Open "StepOne Software v2.0" program.
    - Click "Advanced Setup" button.
    - Under "Experiment Properties," enter an Experiment Name, select "StepOnePlus Instrument (96 Wells)" for the instrument, select "Quantitation – Comparative C_T ($\Delta\Delta C_T$)" for the experiment, select "SYBR Green Reagents"

for the reagent (melt curve is optional), and select “Standard” for the ramp speed.

- Under “Plate Setup,” add your targets and samples under “Define Targets and Samples,” changing the Reporter to “SYBR” and the Quencher to “None.” Under “Assign Targets and Samples,” assign the appropriate targets and samples to each well, selecting your control sample as the reference sample, GAPDH as the endogenous control, and “ROX” as the “dye to use as a passive reference.”
- Under “Run Method,” change the reaction volume to 25 µl and set the method to the following:
    - Hold at 95˚C for 10 min (100% ramp).
    - Cycle 40 times at 95˚C for 15 sec and 60˚C for 1 min, collecting data at 60˚C.
    - Optional melt curve: 95˚C for 15 sec, 60˚C for 1 min, and +0.3˚C ramp, ending at 95˚C for 15 sec and collecting data during the +0.3˚C ramp.
- Save the file.

  (Templates can be saved to reduce setup time.)
- Select “Start Run.”
- After the run, click “Analyze” (settings can be modified under “Analysis Settings”) and resave the file.
- Export results to Excel by clicking “Export…” and export “Results” as “One File” with “.xls” file type.

C.10: PCR Analysis

Most of this tutorial is taken shamefully from:

Ruijter JM, Ramakers C, Hoogaars WMH, Karlen Y, Bakker O, van den Hoff MJB, and Moorman AFM. Amplification efficiency: linking baseline and bias in the analysis of quantitative PCR data. Nucleic Acids Res. 2009 Apr;37(6):e45.

Introduction

Let's review the basics of PCR amplification and detection. We start with a few basic equations:

$$N_c = N_0 E^c \qquad E = \frac{N_{c+1}}{N_c} \qquad N_0 = \frac{N_t}{E^{C_t}}$$

where $\boldsymbol{N}$ = concentration of amplicon, $\boldsymbol{E}$ is the efficiency of the PCR reaction (where 1 means no amplification, and 2 is 100% amplification), and $\boldsymbol{C}$ is a cycle threshold of interest. If you want to compare a gene's amplification to its target gene,

$$\frac{N_{0,\text{collagen I}}}{N_{0,\text{GAPDH}}} = \frac{\frac{N_{t,\text{collagen I}}}{E_{\text{collagen I}}^{C_{t,\text{collagen I}}}}}{\frac{N_{t,\text{GAPDH}}}{E_{\text{GAPDH}}^{C_{t,\text{GAPDH}}}}} \approx \frac{E_{\text{GAPDH}}^{C_{t,\text{GAPDH}}}}{E_{\text{collagen I}}^{C_{t,\text{collagen I}}}}$$

assuming the concentrations of the two genes are the same (given, say, a fluorescence threshold). If you then make the next assumption that the efficiencies are the same (say, 100%), then

$$E_{\text{common}}^{C_{t,\text{GAPDH}} - C_{t,\text{collagen I}}} = E_{\text{common}}^{-\left(C_{t,\text{collagen I}} - C_{t,\text{GAPDH}}\right)} \approx 2^{-\Delta C_t}$$

To compare to day 1, we write

$$\frac{N_{0,\text{collagen I, day 7}}}{N_{0,\text{collagen I, day 1}}} = \frac{E_{\text{common}}^{-\left(C_{t,\text{collagen I, day 7}} - C_{t,\text{GAPDH, day 7}}\right)}}{E_{\text{common}}^{-\left(C_{t,\text{collagen I, day 1}} - C_{t,\text{GAPDH, day 1}}\right)}} \approx \frac{2^{-\Delta C_{t,\text{day 7}}}}{2^{-\Delta C_{t,\text{day 1}}}} = 2^{-\left(\Delta C_{t,\text{day 7}} - \Delta C_{t,\text{day 1}}\right)}$$

$$= 2^{-\Delta\Delta C_t}$$

These calculations are contingent on a few assumptions:

- Baseline fluorescence is something that can be eliminated.
- Efficiency is common (and perhaps, also, that it's 100%) among different genes, primer sets, etc.
- Cycle to cycle efficiency does not vary throughout amplification.

Typical PCR analysis errors

If there *is* baseline fluorescence in your sample, you will introduce error into your estimation of *efficiency*:

$$N_c^* = \text{baseline} + N_0 E^c \qquad\qquad E^* = \frac{\text{baseline} + N_{c+1}}{\text{baseline} + N_c}$$

and if you also fail to account for differences in amplification efficiency, you also introduce error:

$$\text{error} = \frac{E_{\text{GAPDH}}^{C_{t,\text{GAPDH}}}}{E_{\text{collagen I}}^{C_{t,\text{collagen I}}}} \div \frac{E_{\text{common}}^{C_{t,\text{GAPDH}}}}{E_{\text{common}}^{C_{t,\text{collagen I}}}} = \left(\frac{E_{\text{GAPDH}}}{E_{\text{common}}}\right)^{C_{t,\text{GAPDH}}} \left(\frac{E_{\text{collagen I}}}{E_{\text{common}}}\right)^{-C_{t,\text{collagen I}}}$$

$$= \left(\frac{E_{\text{gene}}}{E_{\text{common}}}\right)^{C_{t,\text{GAPDH}} + C_{t,\text{collagen I}}}$$

which for even a 5% difference in efficiency can be $1.05^{20+20} = 1.05^{40} = 7.03$ times different.

What LinRegPCR does

- Estimates individual well baseline by reconstructing the log-linear portion of the amplification curve:
  - Discards any samples where low amplification is detected.
  - Calculates the second derivative maximum (SDM) to find the plateau.
  - Subtracts baseline, then fits both the upper and bottom portions of log-linear region.
  - When the lower and upper sections' slopes match, the baseline has been found.
- Calculates individual PCR efficiencies for every well
  - Calculates mean efficiency and starting amount (N_0) for a given amplicon.
  - Mean efficiencies are adequate for calculating fold regulation values
    - Differences are more a result of statistical error than true differences in efficiency.
    - What about running multiple plates for the same gene?
    - Individual efficiencies can vary significantly

How to use LinRegPCR

1) Process your data in StepOne first.
   a) Do a quick quality control check on your samples and remove samples that didn't amplify well, that have a high standard deviation, etc.
   b) **Disable** the auto baseline feature in StepOne for each target.
   c) Export the data to Excel – check *Sample Setup* and *Amplification Data*.
2) Open the spreadsheet and then open LinRegPCR.

Note: LinRegPCR will not work correctly unless Excel is opened beforehand.

3) In LinRegPCR:
    a) Read in your data.
        i) Check the drop-down boxes to make sure Amplification Data is selected.
        ii) Select **Step-One Plus (ABI)** and **DNA binding dye** (SYBR Green).
        iii) Select columns A through D, rows 8 through 3848 (that is, a 40-cycle run. A 50-cycle run would go to row 4808.)
        iv) Make sure ss cDNA is checked, and select No for "Data are baseline-corrected."
    b) Click the red button labeled **determine baselines**.
    c) Check each sample to examine efficiencies and tweak if necessary.
    d) If necessary, use the Amplicon Groups tab to set amplicon groups. The boxes there can help you auto-select amplicon groups quickly for each gene.
    e) Set the log(fluorescence) value on the left.
        i) Note: Make sure to keep this consistent between all plates with the same gene.
        ii) Note: In StepOne, the threshold fluorescence is usually less than 1, which is why the log(fluorescence) value in LinRegPCR is negative.
    f) Save this data to Excel.
4) Back in Excel:
    a) Use the sample setup tab to help re-label your samples and rearrange your data to your liking. You may want to pick up some Excel-fu to summarize and put all of your wells together, do any extra quality control, etc.

i) Note: Remember to use geometric means when averaging data. (Taking the geometric mean is the same as taking the arithmetic mean of the cycle thresholds.)

b) To calculate fold regulation, use the starting concentration of your gene, or N_0. The value of N_0 has already been calculated by LinRegPCR using the mean efficiency for the amplicon group.

i) If many of your wells did not use the mean efficiency to be calculated, it may be a good idea to calculate a new N_0 based on each individual well's PCR efficiency.

ii) You can do this using the equation $N_0^* = \frac{\text{fluorescence threshold value}}{\text{Eff}^{Cq}}$.

c) Calculate a manual ΔΔ method; that is, divide a sample's gene's N_0 by the sample's GAPDH N_0 value, then divide by the geometric mean of your day 1 sample.

d) Perform statistical analysis on the divided-by-GAPDH values.

C.11: Immunohistochemistry

Rules to remember:

- Do not let your sample dry out. This will encourage non-specific binding (and staining) from anything floating around in the air, etc. If you need to stop, make sure samples are wet or otherwise sitting in PBS.
- Store samples at -80°C prior to staining to maintain maximum antigenicity.
- Rinsing with PBS can be done using a slide rack. Place slides into the stain rack, then gently lower into the stain holder with PBS. After two minutes, raise and

lower the rack gently, then remove the rack completely. Do this twice, discarding PBS between washes. You'll need ~1000-1200 mL PBS for 12 slides if you use the histology room's stain holders.

Day 1

1) Fixation
    a) Warm up slides at room temperature for 30-60 minutes.
    b) Lightly fix in ice cold acetone for 10 minutes. Place a stain holder containing acetone into an ice bucket, then lower the slide rack inside.
    c) Let slides air dry for 30 minutes, then do a PBS wash. Change acetone between slide racks if you're doing more than 12 slides at a time.
2) Preparation (while slides dry)
    a) 1% BSA solution (Get BSA frozen from histology room; make 1 g BSA / 100 mL PBS; store at 4°C)
    b) Serum from species of secondary Ab (goat, horse, or rabbit; get from histology room)
    c) Make a humidified chamber using a 150 mm petri dish with a wet paper towel in the bottom, plus 4-5 small petri dishes with water inside. Each chamber can hold 4 or 5 slides.
3) Peroxidase Blocking
    a) Use a slide rack/stain holder to immerse slides in 0.3% peroxide/methanol solution (1 mL 30% H_2O_2 in 100 mL methanol; store in foil < 1 week at 4°C) for

10 minutes at room temperature. You can reuse the peroxide/methanol solution between racks.

b) At this point, samples should be completely free of OCT and other trash. Circle each sample with a PAP pen to isolate future liquids to the sample, then PBS wash.

4) Serum Blocking

a) Normal Serum Block Solution (60 µL/sample, mix in 10 mL and store at 4°C):

i) 1% BSA solution in PBS (stabilizer) – 9.7 mL

ii) 2% serum (blocking) – 200 µL

iii) 0.1% Triton X-100 (penetration enhancer) – 100 µL

b) Incubate sections for 20 min in blocking solution – serum should be same species as secondary antibody. Tap the slide on a kimwipe to remove the solution. Don't do a PBS wash afterwards.

5) Primary Antibody

a) Prepare the working dilution of the primary antibody in 1% BSA. If using an antibody for the first time, you'll need to run a series of dilutions to determine the optimal working concentration). With our antibodies, 1:10, 1:100, 1:500, 1:1000 is a good start.

b) Use a 10 µL pipette to carefully apply 8 µL primary antibody to each sample.

c) Incubate sections in a humid chamber at 4°C overnight. Parafilm each chamber to prevent evaporation.

Day 2

6) Secondary Antibody
    a) Remove slides from the humidified chamber and PBS wash.
    b) Incubate sections in 1:20 goat biotin conjugated secondary antibody in PBS for 30 minutes at room temperature, then PBS wash.
7) Signal Amplification
    a) Solution: Vectastain ABC Elite Standard kit
        i) 5 mL PBS + 2 drops of solution A + 2 drops of solution B, added into the provided bottle.
        ii) Allow solution to sit for 30 min before use.
    b) Drop solution onto slides. Incubate for 30 min, then PBS wash.
8) Chromagen/Substrate Stain
    a) Immediately after rinsing, make the peroxidase substrate solution using 1 mL substrate buffer and 20 μL chromogen. There should be no delay between making the solution and adding it to your slides.
    b) Allow color to develop for 5-10 minutes (you will need to experiment with this time).
    c) Immediately rinse with PBS twice. All DAB waste should be added into a separate waste container and brought to the histology room for disposal.
9) Cover slip
    a) The slide should be wet from the PBS wash you just did. Place a drop of FluoroGel with Tris buffer on each of your samples within a PAP pen circle. FluoroGel should mix with the water already on the slide.

b) Place additional FluoroGel (can use two drops; may use more if desired) outside of the PAP pen circles.

c) Tilt the bottom edge of the cover slip against the bottom edge of the slide. Tilt the slide as necessary so the cover slip catches a consistent edge of liquid along the bottom, then gently lower the top edge so the liquid rides over the PAP pen circles and catches the entire surface of the slide.

d) Allow slides to dry overnight. You can view them on a microscope sooner than that (a few hours after coverslipping), but sometimes liquid will leak from a slide as it dries. Clean liquid that has leaked onto the outside with wet kimwipes.

REFERENCES

1. Martin RB, Burr DB, Sharkey NA, editors. Skeletal tissue mechanics. New York: Springer; 1998.

2. Pennisi E. Tending tender tendons. Science. 2002 Mar 08;Sect. 1011.

3. Lu HH, Jiang J. Interface tissue engineering and the formulation of multiple-tissue systems. Advances in biochemical engineering/biotechnology. 2006 Feb 01;102:91-111.

4. Lu HH, Subramony SD, Boushell MK, Zhang X. Tissue Engineering Strategies for the Regeneration of Orthopedic Interfaces. Annals of Biomedical Engineering. 2010 May 27.

5. Spalazzi J, Dagher E, Doty S, Guo X, Rodeo S, Lu H. In vivo evaluation of a multiphased scaffold designed for orthopaedic interface tissue engineering and soft tissue-to-bone integration. Journal of Biomedical Materials Research Part A. 2008 May 28.

6. Phillips J, Burns K, Le Doux J, Guldberg R, García A. Engineering graded tissue interfaces. Proc Natl Acad Sci. 2008 Aug 21.

7. Ma J, Goble K, Smietana M, Kostrominova T, Larkin L, Arruda EM. Morphological and functional characteristics of three-dimensional engineered bone-ligament-bone constructs following implantation. Journal of Biomechanical Engineering. 2009 Oct;131(10):101017.

8. Ma J, Smietana MJ, Kostrominova TY, Wojtys E, Larkin LM, Arruda E. Three-Dimensional Engineered Bone-Ligament-Bone Constructs for Anterior Cruciate Ligament Replacement. Tissue Engineering Part A. 2011 Sep 09.

9. Altman GH, Horan RL, Martin I, Farhadi J, Stark PRH, Volloch V, et al. Cell differentiation by mechanical stress. FASEB J. 2002 Mar 01;16(2):270-2.

10. Lutolf MP, Hubbell JA. Synthetic biomaterials as instructive extracellular microenvironments for morphogenesis in tissue engineering. Nature Biotechnology. 2005 Feb 01;23(1):47-55.

11. Pedowitz RA, O'Connor JJ, Akeson WH, editors. Daniel's Knee Injuries: Ligament and Cartilage Structure, Function, Injury and Repair. 2 ed. Philadelphia: Lippincott, Williams and Wilkins; 2003.

12. Benjamin M, Ralphs JR. The cell and developmental biology of tendons and ligaments. International review of cytology. 2000 Feb 01;196:85-130.

13. Goh JC, Ouyang HW, Teoh SH, Chan CK, Lee EH. Tissue-engineering approach to the repair and regeneration of tendons and ligaments. Tissue Eng. 2003 Jan 1;9 Suppl 1:S31-44.

14. Wang JH-C. Mechanobiology of tendon. Journal of Biomechanics. 2006 Feb 01;39(9):1563-82.

15. Yoon JH, Halper J. Tendon proteoglycans: biochemistry and function. Journal of musculoskeletal & neuronal interactions. 2005 Apr 01;5(1):22-34.

16. Chiquet-Ehrismann R, Chiquet M. Tenascins: regulation and putative functions during pathological stress. The Journal of pathology. [Review]. 2003 Jul;200(4):488-99.

17. Vunjak-Novakovic G, Altman G, Horan R, Kaplan DL. Tissue engineering of ligaments. Annual review of biomedical engineering. 2004 Feb 01;6:131-56.

18. Yang PJ, Temenoff JS. Engineering orthopedic tissue interfaces. Tissue Engineering Part B: Reviews. [Review]. 2009 Jul;15(2):127-41.

19. Woo SL, Buckwalter JA. AAOS/NIH/ORS workshop. Injury and repair of the musculoskeletal soft tissues. Savannah, Georgia, June 18-20, 1987. J Orthop Res. 1988 Feb 01;6(6):907-31.

20. Benjamin M, Ralphs JR. Fibrocartilage in tendons and ligaments--an adaptation to compressive load. Journal of anatomy. 1998 Nov 01;193 (Pt 4):481-94.

21. Woo SL-Y, Abramowitch SD, Kilger R, Liang R. Biomechanics of knee ligaments: injury, healing, and repair. Journal of Biomechanics. 2006 Feb 01;39(1):1-20.

22. Moffat KL, Sun W-HS, Pena PE, Chahine NO, Doty SB, Ateshian GA, et al. Characterization of the structure-function relationship at the ligament-to-bone interface. Proc Natl Acad Sci. 2008 Jul 10;105(23):7947-52.

23. Benjamin M, Kumai T, Milz S, Boszczyk BM, Boszczyk AA, Ralphs JR. The skeletal attachment of tendons--tendon "entheses". Comp Biochem Physiol, Part A Mol Integr Physiol. 2002 Dec 1;133(4):931-45.

24. Williams JG. Achilles tendon lesions in sport. Sports Medicine. [Review]. 1986 Mar;3(2):114-35.

25. Lim J, Temenoff J. Tendon and Ligament Tissue Engineering: Restoring Tendon/Ligament and Its Interfaces. Fundamentals of Tissue Engineering and Regenerative Medicine. 2009:255-69.

26. Lin TWTW, Cardenas L, Soslowsky LJLJ. Biomechanics of tendon injury and repair. Journal of Biomechanics. 2004 Jul 01;37(6):865-77.

27. Sharma P, Maffulli N. Biology of tendon injury: healing, modeling and remodeling. Journal of musculoskeletal & neuronal interactions. [Review]. 2006 Apr;6(2):181-90.

28. Sharma P, Maffulli N. Tendon injury and tendinopathy: healing and repair. The Journal of bone and joint surgery American volume. [Review]. 2005 Feb;87(1):187-202.

29. Laurencin CT, Freeman JW. Ligament tissue engineering: an evolutionary materials science approach. Biomaterials. 2005 Dec 01;26(36):7530-6.

30. Marder RA, Raskind JR, Carroll M. Prospective evaluation of arthroscopically assisted anterior cruciate ligament reconstruction. Patellar tendon versus semitendinosus and gracilis tendons. The American Journal of Sports Medicine. 1991 Feb 01;19(5):478-84.

31. Aglietti P, Buzzi R, Zaccherotti G, de Biase P. Patellar tendon versus doubled semitendinosus and gracilis tendons for anterior cruciate ligament reconstruction. The American Journal of Sports Medicine. 1994 Feb 01;22(2):211-7.

32. Brown CH, Steiner ME, Carson EW. The use of hamstring tendons for anterior cruciate ligament reconstruction. Technique and results. Clinics in sports medicine. 1993 Oct 01;12(4):723-56.

33. Jansson KA, Linko E, Sandelin J, Harilainen A. A prospective randomized study of patellar versus hamstring tendon autografts for anterior cruciate ligament reconstruction. The American Journal of Sports Medicine. 2003 Feb 01;31(1):12-8.

34. Beynnon BD, Johnson RJ, Abate JA, Fleming BC, Nichols CE. Treatment of anterior cruciate ligament injuries, part I. The American Journal of Sports Medicine. 2005 Oct 01;33(10):1579-602.

35. Webster KE, Feller JA, Hameister KA. Bone tunnel enlargement following anterior cruciate ligament reconstruction: a randomised comparison of hamstring and patellar tendon grafts with 2-year follow-up. Knee survery, sports traumatology, arthroscopy. 2001 Feb 01;9(2):86-91.

36. Kousa P, Järvinen TLN, Vihavainen M, Kannus P, Järvinen M. The fixation strength of six hamstring tendon graft fixation devices in anterior cruciate ligament reconstruction. Part I: femoral site. The American Journal of Sports Medicine. 2003 Feb 01;31(2):174-81.

37. Kessler M, Behrend H, Henz S, Stutz G, Rukavina A, Kuster M. Function, osteoarthritis and activity after ACL-rupture: 11 years follow-up results of conservative versus reconstructive treatment. Knee surgery, sports traumatology, arthroscopy : official journal of the ESSKA. 2008 Mar 22.

38. Rodeo SA, Arnoczky SP, Torzilli PA, Hidaka C, Warren RF. Tendon-healing in a bone tunnel. A biomechanical and histological study in the dog. The Journal of bone and joint surgery American volume. 1993 Dec 01;75(12):1795-803.

39. Grana WA, Egle DM, Mahnken R, Goodhart CW. An analysis of autograft fixation after anterior cruciate ligament reconstruction in a rabbit model. The American Journal of Sports Medicine. 1994 Feb 01;22(3):344-51.

40. Brand J, Weiler A, Caborn DN, Brown CH, Johnson DL. Graft fixation in cruciate ligament reconstruction. The American Journal of Sports Medicine. 2000 Feb 01;28(5):761-74.

41. Kurosaka M, Yoshiya S, Andrish JT. A biomechanical comparison of different surgical techniques of graft fixation in anterior cruciate ligament reconstruction. The American Journal of Sports Medicine. [Comparative Study]. 1987 May;15(3):225-9.

42. Robertson DB, Daniel DM, Biden E. Soft tissue fixation to bone. The American Journal of Sports Medicine. 1986 Aug;14(5):398-403.

43. St Pierre P, Olson EJ, Elliott JJ, O'Hair KC, McKinney LA, Ryan J. Tendon-healing to cortical bone compared with healing to a cancellous trough. A biomechanical and histological evaluation in goats. The Journal of bone and joint surgery American volume. [Comparative Study]. 1995 Dec;77(12):1858-66.

44. Jackson DW, Grood ES, Arnoczky SP, Butler DL, Simon TM. Cruciate reconstruction using freeze dried anterior cruciate ligament allograft and a ligament augmentation device (LAD). An experimental study in a goat model. The American Journal of Sports Medicine. 1987 Oct;15(6):528-38.

45. Berg EE. Autograft bone-patella tendon-bone plug comminution with loss of ligament fixation and stability. Arthroscopy. [Case Report]. 1996 May;12(2):232-5.

46. Zantop T, Weimann A, Schmidtko R, Herbort M, Raschke MJ, Petersen W. Graft laceration and pullout strength of soft-tissue anterior cruciate ligament reconstruction: in vitro study comparing titanium, poly-d,l-lactide, and poly-d,l-lactide-tricalcium phosphate screws. Arthroscopy. [Comparative Study]. 2006 Nov;22(11):1204-10.

47. Lu HH, Subramony SD, Boushell MK, Zhang X. Tissue engineering strategies for the regeneration of orthopedic interfaces. Annals of Biomedical Engineering. [Review]. 2010 Jul;38(6):2142-54.

48. Hashimoto Y, Yoshida G, Toyoda H, Takaoka K. Generation of tendon-to-bone interface "enthesis" with use of recombinant BMP-2 in a rabbit model. J Orthop Res. 2007 Nov;25(11):1415-24.

49. Gulotta LV, Kovacevic D, Packer JD, Deng XH, Rodeo SA. Bone Marrow-Derived Mesenchymal Stem Cells Transduced With Scleraxis Improve Rotator Cuff Healing in a Rat Model. The American Journal of Sports Medicine. 2011 Mar 18.

50. Kovacevic D, Fox AJ, Bedi A, Ying L, Deng X-H, Warren RF, et al. Calcium-phosphate matrix with or without TGF-β3 improves tendon-bone healing after rotator cuff repair. The American Journal of Sports Medicine. 2011 May;39(4):811-9.

51. Brophy RH, Gill CS, Lyman S, Barnes RP, Rodeo SA, Warren RF. Effect of shoulder stabilization on career length in national football league athletes. The American Journal of Sports Medicine. 2011 May;39(4):704-9.

52. Gulotta LV, Kovacevic D, Montgomery S, Ehteshami JR, Packer JD, Rodeo SA. Stem cells genetically modified with the developmental gene MT1-MMP improve regeneration of the supraspinatus tendon-to-bone insertion site. The American Journal of Sports Medicine. 2010 Jul;38(7):1429-37.

53. Sundar S, Pendegrass CJ, Blunn GW. Tendon bone healing can be enhanced by demineralized bone matrix: a functional and histological study. Journal of biomedical materials research Part B, Applied biomaterials. 2009 Feb;88(1):115-22.

54. Yokoya S, Mochizuki Y, Nagata Y, Deie M, Ochi M. Tendon-bone insertion repair and regeneration using polyglycolic acid sheet in the rabbit rotator cuff injury model. The American Journal of Sports Medicine. [Comparative Study]. 2008 Jul;36(7):1298-309.

55. Snook GA. A short history of the anterior cruciate ligament and the treatment of tears. Clinical Orthopaedics and Related Research. [Historical Article]. 1983(172):11-3.

56. Smith BA, Livesay GA, Woo SL. Biology and biomechanics of the anterior cruciate ligament. Clinics in sports medicine. [Review]. 1993 Oct;12(4):637-70.

57. Ge Z, Goh JCH, Lee EH. Selection of cell source for ligament tissue engineering. Cell transplantation. 2005 Feb 01;14(8):573-83.

58. Molloy T, Wang Y, Murrell G. The roles of growth factors in tendon and ligament healing. Sports Medicine. 2003 Feb 01;33(5):381-94.

59. Nöth U, Schupp K, Heymer A, Kall S, Jakob F, Schütze N, et al. Anterior cruciate ligament constructs fabricated from human mesenchymal stem cells in a collagen type I hydrogel. Cytotherapy. 2005 Feb 01;7(5):447-55.

60. Awad HA, Boivin GP, Dressler MR, Smith FNL, Young RG, Butler DL. Repair of patellar tendon injuries using a cell-collagen composite. J Orthop Res. 2003 Jun 01;21(3):420-31.

61. Butler DL, Awad HA. Perspectives on cell and collagen composites for tendon repair. Clinical Orthopaedics and Related Research. 1999 Oct 01(367 Suppl):S324-32.

62. Cornwell KG, Lei P, Andreadis ST, Pins GD. Crosslinking of discrete self-assembled collagen threads: Effects on mechanical strength and cell-matrix interactions. Journal of Biomedical Materials Research Part A. 2007 Mar 01;80(2):362-71.

63. Meaney Murray M, Rice K, Wright RJ, Spector M. The effect of selected growth factors on human anterior cruciate ligament cell interactions with a three-dimensional collagen-GAG scaffold. J Orthop Res. 2003 Apr 01;21(2):238-44.

64. Torres DS, Freyman TM, Yannas IV, Spector M. Tendon cell contraction of collagen-GAG matrices in vitro: effect of cross-linking. Biomaterials. 2000 Aug 01;21(15):1607-19.

65. Thomopoulos S, Das R, Birman V, Smith L, Ku K, Elson E, et al. Fibrocartilage tissue engineering: The role of the stress environment on cell morphology and matrix expression. Tissue Engineering Part A. 2010 Nov 23.

66. Gentleman E, Livesay GA, Dee KC, Nauman EA. Development of ligament-like structural organization and properties in cell-seeded collagen scaffolds in vitro. Annals of Biomedical Engineering. 2006 Jun 01;34(5):726-36.

67. Altman GH, Diaz F, Jakuba C, Calabro T, Horan RL, Chen J, et al. Silk-based biomaterials. Biomaterials. 2003 Mar 01;24(3):401-16.

68. Altman GH, Horan RL, Lu HH, Moreau J, Martin I, Richmond JC, et al. Silk matrix for tissue engineered anterior cruciate ligaments. Biomaterials. 2002 Oct 01;23(20):4131-41.

69. Cooper JA, Bailey LO, Carter JN, Castiglioni CE, Kofron MD, Ko FK, et al. Evaluation of the anterior cruciate ligament, medial collateral ligament, achilles tendon and patellar tendon as cell sources for tissue-engineered ligament. Biomaterials. 2006 Jun 01;27(13):2747-54.

70. Lu HH, Cooper JA, Manuel S, Freeman JW, Attawia MA, Ko FK, et al. Anterior cruciate ligament regeneration using braided biodegradable scaffolds: in vitro optimization studies. Biomaterials. 2005 Aug 01;26(23):4805-16.

71. Ouyang HW, Toh SL, Goh J, Tay TE, Moe K. Assembly of bone marrow stromal cell sheets with knitted poly (L-lactide) scaffold for engineering ligament analogs. Journal of biomedical materials research Part B, Applied biomaterials. 2005 Nov 01;75(2):264-71.

72. Cooper JA, Lu HH, Ko FK, Freeman JW, Laurencin CT. Fiber-based tissue-engineered scaffold for ligament replacement: design considerations and in vitro evaluation. Biomaterials. 2005 Jun 01;26(13):1523-32.

73. Qin T-W, Yang Z-M, Wu Z-Z, Xie H-Q, Qin J, Cai S-X. Adhesion strength of human tenocytes to extracellular matrix component-modified poly(DL-lactide-co-glycolide) substrates. Biomaterials. 2005 Nov 01;26(33):6635-42.

74. Cooper JA, Sahota JS, Gorum WJ, Carter J, Doty SB, Laurencin CT. Biomimetic tissue-engineered anterior cruciate ligament replacement. Proc Natl Acad Sci. 2007 Mar 27;104(9):3049-54.

75. Lu HH, El-Amin SF, Scott KD, Laurencin CT. Three-dimensional, bioactive, biodegradable, polymer-bioactive glass composite scaffolds with improved mechanical properties support collagen synthesis and mineralization of human osteoblast-like cells in vitro. Journal of Biomedical Materials Research Part A. 2003 Apr 01;64(3):465-74.

76. Spalazzi JP, Dagher E, Doty SB, Guo XE, Rodeo SA, Lu HH. In vivo evaluation of a tri-phasic composite scaffold for anterior cruciate ligament-to-bone integration. Conference proceedings : Annual International Conference of the IEEE Engineering in Medicine and Biology Society IEEE Engineering in Medicine and Biology Society Conference. 2006 Feb 01;1:525-8.

77. Spalazzi J, Vyner M, Jacobs M, Moffat K, Lu H. Mechanoactive Scaffold Induces Tendon Remodeling and Expression of Fibrocartilage Markers. Clinical Orthopaedics and Related Research®. 2008 Jun 30.

78. Spalazzi JP, Doty SB, Moffat KL, Levine WN, Lu HH. Development of controlled matrix heterogeneity on a triphasic scaffold for orthopedic interface tissue engineering. Tissue engineering. 2006 Dec 01;12(12):3497-508.

79. Shahab-Osterloh S, Witte F, Hoffmann A, Winkel A, Laggies S, Neumann B, et al. Mesenchymal stem cell-dependent formation of heterotopic tendon-bone insertions (osteotendinous junctions). Stem Cells. 2010 Sep 01;28(9):1590-601.

80. Paxton JZ, Donnelly K, Keatch RP, Baar K. Engineering the bone-ligament interface using polyethylene glycol diacrylate incorporated with hydroxyapatite. Tissue Engineering Part A. 2009 Jul;15(6):1201-9.

81. Paxton JZ, Grover LM, Baar K. Engineering an In Vitro Model of a Functional Ligament from Bone to Bone. Tissue Engineering Part A. 2010 Aug 28.

82. Wang X, Grogan SP, Rieser F, Winkelmann V, Maquet V, Berge ML, et al. Tissue engineering of biphasic cartilage constructs using various biodegradable scaffolds: an in vitro study. Biomaterials. 2004 Aug 01;25(17):3681-8.

83. Hung CT, Lima EG, Mauck RL, Takai E, Taki E, LeRoux MA, et al. Anatomically shaped osteochondral constructs for articular cartilage repair. Journal of Biomechanics. 2003 Dec 01;36(12):1853-64.

84. Solchaga LA, Gao J, Dennis JE, Awadallah A, Lundberg M, Caplan AI, et al. Treatment of osteochondral defects with autologous bone marrow in a hyaluronan-based delivery vehicle. Tissue engineering. 2002 May 01;8(2):333-47.

85. Tuli R, Nandi S, Li W-J, Tuli S, Huang X, Manner PA, et al. Human mesenchymal progenitor cell-based tissue engineering of a single-unit osteochondral construct. Tissue engineering. 2004 Feb 01;10(7-8):1169-79.

86. Alhadlaq A, Elisseeff JH, Hong L, Williams CG, Caplan AI, Sharma B, et al. Adult stem cell driven genesis of human-shaped articular condyle. Annals of Biomedical Engineering. 2004 Jul 01;32(7):911-23.

87. Alhadlaq A, Mao JJ. Tissue-engineered osteochondral constructs in the shape of an articular condyle. The Journal of bone and joint surgery American volume. 2005 Jun;87(5):936-44.

88. Holland TA, Bodde EWH, Baggett LS, Tabata Y, Mikos AG, Jansen JA. Osteochondral repair in the rabbit model utilizing bilayered, degradable oligo(poly(ethylene glycol) fumarate) hydrogel scaffolds. Journal of Biomedical Materials Research Part A. 2005 Oct 01;75(1):156-67.

89. Doroski DM, Levenston ME, Temenoff JS. Cyclic tensile culture promotes fibroblastic differentiation of marrow stromal cells encapsulated in poly(ethylene glycol)-based hydrogels. Tissue Engineering Part A. 2010 Nov;16(11):3457-66.

90. Drury JL, Mooney DJ. Hydrogels for tissue engineering: scaffold design variables and applications. Biomaterials. [Review]. 2003 Nov;24(24):4337-51.

91. Hoffman AS. Hydrogels for biomedical applications. Advanced drug delivery reviews. [Review]. 2002 Feb 17;54(1):3-12.

92. Nicodemus GD, Bryant SJ. Cell encapsulation in biodegradable hydrogels for tissue engineering applications. Tissue Engineering Part B: Reviews. 2008 Jul 01;14(2):149-65.

93. Tibbitt MW, Anseth KS. Hydrogels as extracellular matrix mimics for 3D cell culture. Biotechnology and Bioengineering. [Review]. 2009 Jul 01;103(4):655-63.

94. Lee KY, Mooney DJ. Hydrogels for tissue engineering. Chemical reviews. [Review]. 2001 Jul;101(7):1869-79.

95. Rice MA, Anseth KS. Controlling cartilaginous matrix evolution in hydrogels with degradation triggered by exogenous addition of an enzyme. Tissue engineering. 2007 May 01;13(4):683-91.

96. Salinas CN, Cole BB, Kasko AM, Anseth KS. Chondrogenic differentiation potential of human mesenchymal stem cells photoencapsulated within poly(ethylene glycol)-arginine-glycine-aspartic acid-serine thiol-methacrylate mixed-mode networks. Tissue engineering. 2007 Jun 01;13(5):1025-34.

97. Park H, Guo X, Temenoff JS, Tabata Y, Caplan AI, Kasper FK, et al. Effect of swelling ratio of injectable hydrogel composites on chondrogenic differentiation of encapsulated rabbit marrow mesenchymal stem cells in vitro. Biomacromolecules. 2009 Apr 09;10(3):541-6.

98. Lutolf MP, Weber FE, Schmoekel HG, Schense JC, Kohler T, Müller R, et al. Repair of bone defects using synthetic mimetics of collagenous extracellular matrices. Nature Biotechnology. 2003 Jun 01;21(5):513-8.

99. Shin H, Quinten Ruhé P, Mikos AG, Jansen JA. In vivo bone and soft tissue response to injectable, biodegradable oligo(poly(ethylene glycol) fumarate) hydrogels. Biomaterials. 2003 Aug 01;24(19):3201-11.

100. Burdick JA, Anseth KS. Photoencapsulation of osteoblasts in injectable RGD-modified PEG hydrogels for bone tissue engineering. Biomaterials. 2002 Nov 01;23(22):4315-23.

101. Harris JM. Poly(Ethylene Glycol) Chemistry: Biotechnical and Biomedical Applications. New York: Plenum Press; 1992.

102. Jo S, Shin H, Shung A, Fisher J, Mikos A. Synthesis and characterization of oligo(poly(ethylene glycol) fumarate) macromer. Macromolecules. 2001 Feb 01;34(9):2839-44.

103. Shin H, Temenoff JS, Mikos AG. In vitro cytotoxicity of unsaturated oligo[poly(ethylene glycol) fumarate] macromers and their cross-linked hydrogels. Biomacromolecules. 2003 May;4(3):552-60.

104. Temenoff JS, Athanasiou KA, LeBaron RG, Mikos AG. Effect of poly(ethylene glycol) molecular weight on tensile and swelling properties of oligo(poly(ethylene glycol) fumarate) hydrogels for cartilage tissue engineering. Journal of Biomedical Materials Research Part A. 2002 Apr 05;59(3):429-37.

105. Temenoff JS, Park H, Jabbari E, Conway DE, Sheffield TL, Ambrose CG, et al. Thermally cross-linked oligo(poly(ethylene glycol) fumarate) hydrogels support osteogenic differentiation of encapsulated marrow stromal cells in vitro. Biomacromolecules. 2004;5(1):5-10.

106. Temenoff JS, Park H, Jabbari E, Sheffield TL, LeBaron RG, Ambrose CG, et al. In vitro osteogenic differentiation of marrow stromal cells encapsulated in biodegradable hydrogels. Journal of Biomedical Materials Research Part A. [In Vitro]. 2004 Aug 01;70(2):235-44.

107. Park H, Temenoff JS, Holland TA, Tabata Y, Mikos AG. Delivery of TGF-beta1 and chondrocytes via injectable, biodegradable hydrogels for cartilage tissue engineering applications. Biomaterials. [Evaluation Study]. 2005 Dec;26(34):7095-103.

108. Qiu Y, Lim JJ, Scott L, Adams RC, Bui HT, Temenoff JS. PEG-based hydrogels with tunable degradation characteristics to control delivery of marrow stromal cells for tendon overuse injuries. Acta Biomaterialia. 2011 Apr;7(3):959-66.

109. Brink KS, Yang PJ, Temenoff JS. Degradative properties and cytocompatibility of a mixed-mode hydrogel containing oligo[poly(ethylene glycol)fumarate] and poly(ethylene glycol)dithiol. Acta Biomaterialia. 2009 Mar;5(2):570-9.

110. Nguyen KT, West JL. Photopolymerizable hydrogels for tissue engineering applications. Biomaterials. 2002 Nov 01;23(22):4307-14.

111. Nuttelman CR, Tripodi MC, Anseth KS. In vitro osteogenic differentiation of human mesenchymal stem cells photoencapsulated in PEG hydrogels. Journal of Biomedical Materials Research Part A. 2004 Apr 15;68(4):773-82.

112. Ifkovits JL, Burdick JA. Review: photopolymerizable and degradable biomaterials for tissue engineering applications. Tissue engineering. [Review]. 2007 Oct;13(10):2369-85.

113. Hersel U, Dahmen C, Kessler H. RGD modified polymers: biomaterials for stimulated cell adhesion and beyond. Biomaterials. 2003 Nov 01;24(24):4385-415.

114. Shin H, Jo S, Mikos AG. Modulation of marrow stromal osteoblast adhesion on biomimetic oligo[poly(ethylene glycol) fumarate] hydrogels modified with Arg-Gly-Asp peptides and a poly(ethyleneglycol) spacer. Journal of Biomedical Materials Research Part A. 2002 Aug 01;61(2):169-79.

115. Villanueva I, Weigel CA, Bryant SJ. Cell-matrix interactions and dynamic mechanical loading influence chondrocyte gene expression and bioactivity in PEG-RGD hydrogels. Acta Biomaterialia. 2009 Oct;5(8):2832-46.

116. Connelly JT, García AJ, Levenston ME. Interactions between integrin ligand density and cytoskeletal integrity regulate BMSC chondrogenesis. Journal of Cellular Physiology. 2008 Oct;217(1):145-54.

117. Salinas CN, Anseth KS. The enhancement of chondrogenic differentiation of human mesenchymal stem cells by enzymatically regulated RGD functionalities. Biomaterials. 2008 Jun 01;29(15):2370-7.

118. Connelly JT, García AJ, Levenston ME. Inhibition of in vitro chondrogenesis in RGD-modified three-dimensional alginate gels. Biomaterials. 2007 Mar;28(6):1071-83.

119. Salinas CN, Anseth KS. The influence of the RGD peptide motif and its contextual presentation in PEG gels on human mesenchymal stem cell viability. Journal of Tissue Engineering and Regenerative Medicine. 2008 Jul 01;2(5):296-304.

120. Benoit DSW, Tripodi MC, Blanchette JO, Langer SJ, Leinwand LA, Anseth KS. Integrin-linked kinase production prevents anoikis in human mesenchymal stem cells. Journal of Biomedical Materials Research Part A. 2007 Jun 01;81(2):259-68.

121. Friedland JC, Lee MH, Boettiger D. Mechanically activated integrin switch controls alpha5beta1 function. Science. 2009 Feb 30;323(5914):642-4.

122. García AJ, Schwarzbauer JE, Boettiger D. Distinct activation states of alpha5beta1 integrin show differential binding to RGD and synergy domains of fibronectin. Biochemistry. 2002 Jul 23;41(29):9063-9.

123. Hsiong SX, Huebsch N, Fischbach C, Kong HJ, Mooney DJ. Integrin-adhesion ligand bond formation of preosteoblasts and stem cells in three-dimensional RGD presenting matrices. Biomacromolecules. 2008 Jul 01;9(7):1843-51.

124. Mao Y, Schwarzbauer JE. Accessibility to the fibronectin synergy site in a 3D matrix regulates engagement of alpha5beta1 versus alphavbeta3 integrin receptors. Cell communication & adhesion. 2006 Aug;13(5-6):267-77.

125. Chiquet M, Gelman L, Lutz R, Maier S. From mechanotransduction to extracellular matrix gene expression in fibroblasts. Biochimica et biophysica acta. 2009 Jun 01;1793(5):911-20.

126. Geiger B, Spatz JP, Bershadsky AD. Environmental sensing through focal adhesions. Nature Reviews Molecular Cell Biology. [Review]. 2009 Feb;10(1):21-33.

127. Rizzi SC, Ehrbar M, Halstenberg S, Raeber GP, Schmoekel HG, Hagenmüller H, et al. Recombinant protein-co-PEG networks as cell-adhesive and proteolytically degradable hydrogel matrixes. Part II: biofunctional characteristics. Biomacromolecules. 2006 Nov 01;7(11):3019-29.

128. Clark RAF, Ghosh K, Tonnesen MG. Tissue engineering for cutaneous wounds. The Journal of investigative dermatology. [Review]. 2007 Jun;127(5):1018-29.

129. Pratt AB, Weber FE, Schmoekel HG, Müller R, Hubbell JA. Synthetic extracellular matrices for in situ tissue engineering. Biotechnology and Bioengineering. [Comparative Study]. 2004 May 05;86(1):27-36.

130. Visse R, Nagase H. Matrix metalloproteinases and tissue inhibitors of metalloproteinases: structure, function, and biochemistry. Circulation research. [Review]. 2003 Jun 02;92(8):827-39.

131. Murphy G, Nagase H. Progress in matrix metalloproteinase research. Molecular aspects of medicine. [Review]. 2008 Oct;29(5):290-308.

132. Nagase H, Visse R, Murphy G. Structure and function of matrix metalloproteinases and TIMPs. Cardiovascular research. [Review]. 2006 Mar 15;69(3):562-73.

133. West J, Hubbell J. Polymeric biomaterials with degradation sites for proteases involved in cell migration. Macromolecules. 1999 Feb 01;32(1):241-4.

134. Gobin AS, West JL. Cell migration through defined, synthetic ECM analogs. FASEB J. 2002 Jun 01;16(7):751-3.

135. Mann BK, Gobin AS, Tsai AT, Schmedlen RH, West JL. Smooth muscle cell growth in photopolymerized hydrogels with cell adhesive and proteolytically degradable domains: synthetic ECM analogs for tissue engineering. Biomaterials. 2001 Nov 01;22(22):3045-51.

136. Nagase H, Fields GB. Human matrix metalloproteinase specificity studies using collagen sequence-based synthetic peptides. Biopolymers. [Review]. 1996;40(4):399-416.

137. Lee S-H, Miller JS, Moon JJ, West JL. Proteolytically degradable hydrogels with a fluorogenic substrate for studies of cellular proteolytic activity and migration. Biotechnology progress. 2005 Feb 01;21(6):1736-41.

138. Saik JE, Gould DJ, Watkins EM, Dickinson ME, West JL. Covalently immobilized platelet-derived growth factor-BB promotes angiogenesis in biomimetic poly(ethylene glycol) hydrogels. Acta Biomaterialia. 2010 Aug 27.

139. Turk BE, Huang LL, Piro ET, Cantley LC. Determination of protease cleavage site motifs using mixture-based oriented peptide libraries. Nature Biotechnology. 2001 Jul;19(7):661-7.

140. Patterson J, Hubbell JA. Enhanced proteolytic degradation of molecularly engineered PEG hydrogels in response to MMP-1 and MMP-2. Biomaterials. [Evaluation Study]. 2010 Oct;31(30):7836-45.

141. Patterson J, Hubbell JA. SPARC-derived protease substrates to enhance the plasmin sensitivity of molecularly engineered PEG hydrogels. Biomaterials. 2011 Mar;32(5):1301-10.

142. Lutolf MP, Lauer-Fields JL, Schmoekel HG, Metters AT, Weber FE, Fields GB, et al. Synthetic matrix metalloproteinase-sensitive hydrogels for the conduction of tissue regeneration: engineering cell-invasion characteristics. Proc Natl Acad Sci. 2003 May 29;100(9):5413-8.

143. Mauney J, Olsen BR, Volloch V. Matrix remodeling as stem cell recruitment event: A novel in vitro model for homing of human bone marrow stromal cells to the site of injury shows crucial role of extracellular collagen matrix. Matrix Biology. 2010 Sep 07.

144. Ponte AL, Marais E, Gallay N, Langonné A, Delorme B, Hérault O, et al. The In Vitro Migration Capacity of Human Bone Marrow Mesenchymal Stem Cells: Comparison of Chemokine and Growth Factor Chemotactic Activities. Stem Cells. 2007 Jul;25(7):1737-45.

145. Nakamizo A, Marini F, Amano T, Khan A, Studeny M, Gumin J, et al. Human bone marrow-derived mesenchymal stem cells in the treatment of gliomas. Cancer Research. 2005 May 15;65(8):3307-18.

146. Klopp AH, Spaeth EL, Dembinski JL, Woodward WA, Munshi A, Meyn RE, et al. Tumor irradiation increases the recruitment of circulating mesenchymal stem cells into the tumor microenvironment. Cancer Research. 2007 Dec 15;67(24):11687-95.

147. Tottey S, Corselli M, Jeffries EM, Londono R, Peault B, Badylak SF. Extracellular Matrix Degradation Products and Low-oxygen Conditions Enhance the Regenerative Potential of Perivascular Stem Cells. Tissue Engineering Part A. 2010 Sep 06.

148. Trkov S, Eng G, Di Liddo R, Parnigotto PP, Vunjak-Novakovic G. Micropatterned three-dimensional hydrogel system to study human endothelial-mesenchymal stem cell interactions. Journal of Tissue Engineering and Regenerative Medicine. 2010 Apr 01;4(3):205-15.

149. Kreja L, Brenner RE, Tautzenberger A, Liedert A, Friemert B, Ehrnthaller C, et al. Non-resorbing osteoclasts induce migration and osteogenic differentiation of mesenchymal stem cells. Journal of cellular biochemistry. 2010 Mar 01;109(2):347-55.

150. Fischer-Valuck BW, Barrilleaux BL, Phinney DG, Russell KC, Prockop DJ, O'Connor KC. Migratory response of mesenchymal stem cells to macrophage migration inhibitory factor and its antagonist as a function of colony-forming efficiency. Biotechnology Letters. 2010 Feb 01;32(1):19-27.

151. Smith AN, Willis E, Chan VT, Muffley LA, Isik FF, Gibran NS, et al. Mesenchymal stem cells induce dermal fibroblast responses to injury. Experimental Cell Research. 2010 Feb 01;316(1):48-54.

152. Tang Y, Wu X, Lei W, Pang L, Wan C, Shi Z, et al. TGF-beta1-induced migration of bone mesenchymal stem cells couples bone resorption with formation. Nature Medicine. 2009 Jul 01;15(7):757-65.

153. Mishima Y, Lotz M. Chemotaxis of human articular chondrocytes and mesenchymal stem cells. J Orthop Res. 2008 Oct 01;26(10):1407-12.

154. Nemir S, Hayenga HN, West JL. PEGDA hydrogels with patterned elasticity: Novel tools for the study of cell response to substrate rigidity. Biotechnology and Bioengineering. 2010 Mar 15;105(3):636-44.

155. Hadjipanayi E, Mudera V, Brown RA. Guiding cell migration in 3D: a collagen matrix with graded directional stiffness. Cell motility and the cytoskeleton. 2009 Apr;66(3):121-8.

156. Lo CM, Wang HB, Dembo M, Wang YL. Cell movement is guided by the rigidity of the substrate. Biophysical journal. 2000 Jul 01;79(1):144-52.

157. DeLong SA, Moon JJ, West JL. Covalently immobilized gradients of bFGF on hydrogel scaffolds for directed cell migration. Biomaterials. 2005 Jul 01;26(16):3227-34.

158. Miron-Mendoza M, Seemann J, Grinnell F. The differential regulation of cell motile activity through matrix stiffness and porosity in three dimensional collagen matrices. Biomaterials. 2010 Sep 01;31(25):6425-35.

159. Ehrbar M, Sala A, Lienemann P, Ranga A, Mosiewicz K, Bittermann A, et al. Elucidating the Role of Matrix Stiffness in 3D Cell Migration and Remodeling. Biophysical journal. 2011 Feb 19;100(2):284-93.

160. Brooks PC, Strömblad S, Sanders LC, von Schalscha TL, Aimes RT, Stetler-Stevenson WG, et al. Localization of matrix metalloproteinase MMP-2 to the surface of invasive cells by interaction with integrin alpha v beta 3. Cell. 1996 Jun 31;85(5):683-93.

161. Karadag A, Fisher LW. Bone sialoprotein enhances migration of bone marrow stromal cells through matrices by bridging MMP-2 to alpha(v)beta3-integrin. Journal of bone and mineral research. 2006 Oct;21(10):1627-36.

162. Lei Y, Gojgini S, Lam J, Segura T. The spreading, migration and proliferation of mouse mesenchymal stem cells cultured inside hyaluronic acid hydrogels. Biomaterials. 2010 Oct 07.

163. Harunaga JS, Yamada KM. Cell-matrix adhesions in 3D. Matrix Biology. 2011 Jul 23.

164. Zaman MH, Kamm RD, Matsudaira P, Lauffenburger DA. Computational model for cell migration in three-dimensional matrices. Biophysical journal. 2005 Aug 01;89(2):1389-97.

165. Zaman MH, Trapani LM, Sieminski AL, Siemeski A, Mackellar D, Gong H, et al. Migration of tumor cells in 3D matrices is governed by matrix stiffness along with cell-matrix adhesion and proteolysis. Proc Natl Acad Sci. 2006 Jul 18;103(29):10889-94.

166. Lutolf MP, Hubbell JA. Synthesis and physicochemical characterization of end-linked poly(ethylene glycol)-co-peptide hydrogels formed by Michael-type addition. Biomacromolecules. 2003 Feb 01;4(3):713-22.

167. Raeber GP, Lutolf MP, Hubbell JA. Molecularly engineered PEG hydrogels: a novel model system for proteolytically mediated cell migration. Biophysical journal. 2005 Aug 01;89(2):1374-88.

168. Harjanto D, Zaman MH. Computational Study of Proteolysis-Driven Single Cell Migration in a Three-Dimensional Matrix. Annals of Biomedical Engineering. 2010 Mar 27.

169. Bott K, Upton Z, Schrobback K, Ehrbar M, Hubbell JA, Lutolf MP, et al. The effect of matrix characteristics on fibroblast proliferation in 3D gels. Biomaterials. 2010 Aug 02.

170. Chen CS, Mrksich M, Huang S, Whitesides GM, Ingber DE. Geometric control of cell life and death. Science. 1997 Jun 30;276(5317):1425-8.

171. McBeath R, Pirone DM, Nelson CM, Bhadriraju K, Chen CS. Cell shape, cytoskeletal tension, and RhoA regulate stem cell lineage commitment. Developmental Cell. 2004 May 01;6(4):483-95.

172. Kilian KA, Bugarija B, Lahn BT, Mrksich M. Geometric cues for directing the differentiation of mesenchymal stem cells. Proc Natl Acad Sci. 2010 Apr 16;107(11):4872-7.

173. Engler AJ, Sen S, Sweeney HL, Discher DE. Matrix elasticity directs stem cell lineage specification. Cell. 2006 Aug 25;126(4):677-89.

174. Chatterjee K, Lin-Gibson S, Wallace WE, Parekh SH, Lee YJ, Cicerone MT, et al. The effect of 3D hydrogel scaffold modulus on osteoblast differentiation and mineralization revealed by combinatorial screening. Biomaterials. 2010 Jul 01;31(19):5051-62.

175. Jagodzinski M, Drescher M, Zeichen J, Hankemeier S, Krettek C, Bosch U, et al. Effects of cyclic longitudinal mechanical strain and dexamethasone on osteogenic differentiation of human bone marrow stromal cells. European cells & materials. 2004 May 16;7:35-41; discussion

176. Huang C-YC, Hagar KL, Frost LE, Sun Y, Cheung HS. Effects of cyclic compressive loading on chondrogenesis of rabbit bone-marrow derived mesenchymal stem cells. Stem Cells. 2004 Feb 01;22(3):313-23.

177. Guilak F, Alexopoulos LG, Upton ML, Youn I, Choi JB, Cao L, et al. The pericellular matrix as a transducer of biomechanical and biochemical signals in articular cartilage. Annals of the New York Academy of Sciences. 2006 May 01;1068:498-512.

178. Connelly JT, Vanderploeg EJ, Mouw JK, Wilson CG, Levenston ME. Tensile loading modulates bone marrow stromal cell differentiation and the development of engineered fibrocartilage constructs. Tissue Engineering Part A. 2010 Jul;16(6):1913-23.

179. Park JS, Chu JSF, Cheng C, Chen F, Chen D, Li S. Differential effects of equiaxial and uniaxial strain on mesenchymal stem cells. Biotechnology and Bioengineering. 2004 Nov 05;88(3):359-68.

180. Wille JJ, Elson EL, Okamoto RJ. Cellular and matrix mechanics of bioartificial tissues during continuous cyclic stretch. Annals of Biomedical Engineering. 2006 Nov;34(11):1678-90.

181. Kuo CK, Tuan RS. Mechanoactive tenogenic differentiation of human mesenchymal stem cells. Tissue Engineering Part A. 2008 Oct 01;14(10):1615-27.

182. Yang G, Crawford RC, Wang JH-C. Proliferation and collagen production of human patellar tendon fibroblasts in response to cyclic uniaxial stretching in serum-free conditions. Journal of Biomechanics. 2004 Oct 01;37(10):1543-50.

183. Connelly JT. Regulatory mechanisms in the chondrogenesis of mesenchymal progenitors: The roles of cyclic tensile loading and cell-matrix interactions. Atlanta, GA: Georgia Institute of Technology; 2007.

184. Katsumi A, Naoe T, Matsushita T, Kaibuchi K, Schwartz MA. Integrin activation and matrix binding mediate cellular responses to mechanical stretch. The Journal of biological chemistry. 2005 May 29;280(17):16546-9.

185. Tetsunaga T, Furumatsu T, Abe N, Nishida K, Naruse K, Ozaki T. Mechanical stretch stimulates integrin alphaVbeta3-mediated collagen expression in human anterior cruciate ligament cells. Journal of Biomechanics. 2009 Sep 18;42(13):2097-103.

186. Guilak F, Cohen DM, Estes BT, Gimble JM, Liedtke W, Chen CS. Control of stem cell fate by physical interactions with the extracellular matrix. Cell stem cell. [Review]. 2009 Jul 02;5(1):17-26.

187. Hoffman BD, Grashoff C, Schwartz MA. Dynamic molecular processes mediate cellular mechanotransduction. Nature. [Review]. 2011 Jul 21;475(7356):316-23.

188. Xu B, Song G, Ju Y, Li X, Song Y, Watanabe S. RhoA/ROCK, cytoskeletal dynamics and focal adhesion kinase are required for mechanical stretch-induced tenogenic differentiation of human mesenchymal stem cells. Journal of Cellular Physiology. 2011 Sep 06.

189. Wang I-NE, Shan J, Choi R, Oh S, Kepler CK, Chen FH, et al. Role of osteoblast-fibroblast interactions in the formation of the ligament-to-bone interface. J Orthop Res. 2007 Dec 01;25(12):1609-20.

190. Hammoudi TM, Lu H, Temenoff JS. Long-term spatially defined coculture within three-dimensional photopatterned hydrogels. Tissue Engineering Part C: Methods. 2010 Dec;16(6):1621-8.

191. Sharma B, Williams CG, Kim TK, Sun D, Malik A, Khan M, et al. Designing zonal organization into tissue-engineered cartilage. Tissue engineering. 2007 Mar 01;13(2):405-14.

192. Rothenberg AR, Ouyang L, Elisseeff JH. Mesenchymal Stem Cell Stimulation of Tissue Growth Depends on Differentiation State. Stem cells and development. 2010 Nov 03.

193. Nguyen LH, Kudva AK, Guckert NL, Linse KD, Roy K. Unique biomaterial compositions direct bone marrow stem cells into specific chondrocytic phenotypes corresponding to the various zones of articular cartilage. Biomaterials. 2011 Mar;32(5):1327-38.

194. Nguyen LH, Kudva AK, Saxena NS, Roy K. Engineering articular cartilage with spatially-varying matrix composition and mechanical properties from a single stem cell population using a multi-layered hydrogel. Biomaterials. 2011 Oct;32(29):6946-52.

195. Kloxin AM, Kloxin CJ, Bowman CN, Anseth KS. Mechanical Properties of Cellularly Responsive Hydrogels and Their Experimental Determination. Advanced materials (Deerfield Beach, Fla). 2010 Jun 14.

196. Stabenfeldt SE, Munglani G, Garc X00ed A AXeSJ, Laplaca MC. Biomimetic Microenvironment Modulates Neural Stem Cell Survival, Migration, and Differentiation. Tissue Engineering Part A. 2010 Oct 08.

197. Luo Y, Shoichet MS. A photolabile hydrogel for guided three-dimensional cell growth and migration. Nature materials. 2004 May 01;3(4):249-53.

198. Phelps EA, Landázuri N, Thulé PM, Taylor WR, García AJ. Bioartificial matrices for therapeutic vascularization. Proc Natl Acad Sci. 2010 Mar 23;107(8):3323-8.

199. Miller JS, Shen CJ, Legant WR, Baranski JD, Blakely BL, Chen CS. Bioactive hydrogels made from step-growth derived PEG-peptide macromers. Biomaterials. 2010 Mar 05.

200. Lee S-H, Moon JJ, Miller JS, West JL. Poly(ethylene glycol) hydrogels conjugated with a collagenase-sensitive fluorogenic substrate to visualize collagenase activity during three-dimensional cell migration. Biomaterials. 2007 Jul 01;28(20):3163-70.

201. Lee S-H, Moon JJ, West JL. Three-dimensional micropatterning of bioactive hydrogels via two-photon laser scanning photolithography for guided 3D cell migration. Biomaterials. 2008 Jul 01;29(20):2962-8.

202. Moon JJ, Hahn MS, Kim I, Nsiah BA, West JL. Micropatterning of poly(ethylene glycol) diacrylate hydrogels with biomolecules to regulate and guide endothelial morphogenesis. Tissue Engineering Part A. 2009 Apr 01;15(3):579-85.

203. Cruise GM, Scharp DS, Hubbell JA. Characterization of permeability and network structure of interfacially photopolymerized poly(ethylene glycol) diacrylate hydrogels. Biomaterials. 1998 Jul 01;19(14):1287-94.

204. Lin C-C, Anseth KS. PEG hydrogels for the controlled release of biomolecules in regenerative medicine. Pharmaceutical research. [Review]. 2009 Apr;26(3):631-43.

205. Decaestecker C, Debeir O, Van Ham P, Kiss R. Can anti-migratory drugs be screened in vitro? A review of 2D and 3D assays for the quantitative analysis of cell migration. Medicinal research reviews. [Review]. 2007 Apr;27(2):149-76.

206. Tayalia P, Mendonca CR, Baldacchini T, Mooney DJ, Mazur E. 3D Cell-Migration Studies using Two-Photon Engineered Polymer Scaffolds. Advanced materials. 2008 Dec 02;20(23):4494-8.

207. Gobin AS, West JL. Effects of epidermal growth factor on fibroblast migration through biomimetic hydrogels. Biotechnology progress. 2003 Feb 01;19(6):1781-5.

208. Fisher KE, Pop A, Koh W, Anthis NJ, Saunders WB, Davis GE. Tumor cell invasion of collagen matrices requires coordinate lipid agonist-induced G-protein and membrane-type matrix metalloproteinase-1-dependent signaling. Molecular cancer. 2006;5:69.

209. Partridge JJ, Madsen MA, Ardi VC, Papagiannakopoulos T, Kupriyanova TA, Quigley JP, et al. Functional analysis of matrix metalloproteinases and tissue inhibitors of metalloproteinases differentially expressed by variants of human HT-1080 fibrosarcoma exhibiting high and low levels of intravasation and metastasis. The Journal of biological chemistry. 2007 Dec 07;282(49):35964-77.

210. Watkins AW, Southard SL, Anseth KS. Characterizing multilaminated hydrogels with spatially varying network structure and solute loading using confocal laser scanning microscopy. Acta Biomaterialia. 2007 Jul 01;3(4):439-48.

211. Petrie RJ, Doyle AD, Yamada KM. Random versus directionally persistent cell migration. Nature Reviews Molecular Cell Biology. [Comparative Study]. 2009 Aug;10(8):538-49.

212. Arnoczky SP, Tian T, Lavagnino M, Gardner K, Schuler P, Morse P. Activation of stress-activated protein kinases (SAPK) in tendon cells following cyclic strain: the effects of strain frequency, strain magnitude, and cytosolic calcium. J Orthop Res. 2002 Sep;20(5):947-52.

213. Hsieh AH, Tsai CM, Ma QJ, Lin T, Banes AJ, Villarreal FJ, et al. Time-dependent increases in type-III collagen gene expression in medical collateral ligament fibroblasts under cyclic strains. J Orthop Res. 2000 Apr;18(2):220-7.

214. Guilak F, Mow VC. The mechanical environment of the chondrocyte: a biphasic finite element model of cell-matrix interactions in articular cartilage. Journal of biomechanics. 2000 Dec 1;33(12):1663-73.

215. Alexopoulos LG, Setton LA, Guilak F. The biomechanical role of the chondrocyte pericellular matrix in articular cartilage. Acta Biomaterialia. 2005 Jun 01;1(3):317-25.

216. Peña E, Calvo B, Martínez MA, Doblaré M. A three-dimensional finite element analysis of the combined behavior of ligaments and menisci in the healthy human knee joint. Journal of Biomechanics. 2006 Feb 01;39(9):1686-701.

217. Lavagnino M, Arnoczky SP, Kepich E, Caballero O, Haut RC. A finite element model predicts the mechanotransduction response of tendon cells to cyclic tensile loading. Biomechanics and modeling in mechanobiology. 2008 Oct 01;7(5):405-16.

218. Connelly JT, Vanderploeg EJ, Levenston ME. The influence of cyclic tension amplitude on chondrocyte matrix synthesis: experimental and finite element analyses. Biorheology. 2004 Feb 01;41(3-4):377-87.

219. Liu Tsang V, Chen AA, Cho LM, Jadin KD, Sah RL, DeLong S, et al. Fabrication of 3D hepatic tissues by additive photopatterning of cellular hydrogels. FASEB J. 2007 Apr;21(3):790-801.

220. Mouw JK, Connelly JT, Wilson CG, Michael KE, Levenston ME. Dynamic compression regulates the expression and synthesis of chondrocyte-specific matrix molecules in bone marrow stromal cells. Stem Cells. 2007 Apr;25(3):655-63.

221. Ignatius A, Blessing H, Liedert A, Schmidt C, Neidlinger-Wilke C, Kaspar D, et al. Tissue engineering of bone: effects of mechanical strain on osteoblastic cells in type I collagen matrices. Biomaterials. [Comparative Study]. 2005 Feb;26(3):311-8.

222. Buschmann MD, Gluzband YA, Grodzinsky AJ, Hunziker EB. Mechanical compression modulates matrix biosynthesis in chondrocyte/agarose culture. Journal of Cell Science. 1995 May;108 (Pt 4):1497-508.

223. Pedron S, Peinado C, Bosch P, Benton JA, Anseth KS. Microfluidic approaches for the fabrication of gradient crosslinked networks based on poly(ethylene glycol) and hyperbranched polymers for manipulation of cell interactions. Journal of Biomedical Materials Research Part A. 2010 Nov 09;96A(1):196-203.

224. Patel RV, Mao JJ. Microstructural and elastic properties of the extracellular matrices of the superficial zone of neonatal articular cartilage by atomic force microscopy. Frontiers in bioscience. 2003 Feb 01;8:a18-25.

225. Bowen W, Lovitt R, Wright C. Application of atomic force microscopy to the study of micromechanical properties of biological materials. Biotechnology Letters. 2000 Feb 01;22(11):893-903.

226. Spalazzi JP, Gallina J, Fung-Kee-Fung SD, Konofagou EE, Lu HH. Elastographic imaging of strain distribution in the anterior cruciate ligament and at the ligament-bone insertions. J Orthop Res. 2006 Oct 01;24(10):2001-10.

227. Kloxin AM, Benton JA, Anseth KS. In situ elasticity modulation with dynamic substrates to direct cell phenotype. Biomaterials. 2010 Feb 01;31(1):1-8.

228. Anseth KS, Bowman CN, Brannon-Peppas L. Mechanical properties of hydrogels and their experimental determination. Biomaterials. [Review]. 1996 Sep;17(17):1647-57.

229. Raeber GP, Mayer J, Hubbell JA. Part I: A novel in-vitro system for simultaneous mechanical stimulation and time-lapse microscopy in 3D. Biomechanics and modeling in mechanobiology. 2008 Jul 01;7(3):203-14.

230. Op Den Buijs J, Ritman EL, Dragomir-Daescu D. Validation of a Fluid-Structure Interaction Model of Solute Transport in Pores of Cyclically Deformed Tissue Scaffolds. Tissue Engineering Part C: Methods. 2010 Apr 16.

231. Upton ML, Guilak F, Laursen TA, Setton LA. Finite element modeling predictions of region-specific cell-matrix mechanics in the meniscus. Biomechanics and modeling in mechanobiology. 2006 Jul 01;5(2-3):140-9.

232. Butler DL, Juncosa-Melvin N, Boivin GP, Galloway MT, Shearn JT, Gooch C, et al. Functional tissue engineering for tendon repair: A multidisciplinary strategy using mesenchymal stem cells, bioscaffolds, and mechanical stimulation. J Orthop Res. [Review]. 2008 Feb;26(1):1-9.

233. Bayer ML, Yeung C-YC, Kadler KE, Qvortrup K, Baar K, Svensson RB, et al. The initiation of embryonic-like collagen fibrillogenesis by adult human tendon fibroblasts when cultured under tension. Biomaterials. 2010 Jul 01;31(18):4889-97.

234. Lu Z, Doulabi BZ, Huang C, Bank RA, Helder MN. Collagen type II enhances chondrogenesis in adipose tissue-derived stem cells by affecting cell shape. Tissue Engineering Part A. [Comparative Study]. 2010 Feb;16(1):81-90.

235. Woods A, Wang G, Beier F. RhoA/ROCK signaling regulates Sox9 expression and actin organization during chondrogenesis. The Journal of biological chemistry. 2005 Apr 25;280(12):11626-34.

236. Shao H-J, Lee Y-T, Chen C-S, Wang J-H, Young T-H. Modulation of gene expression and collagen production of anterior cruciate ligament cells through cell shape changes on polycaprolactone/chitosan blends. Biomaterials. 2010 Jul;31(17):4695-705.

237. Mannello F, Tonti GAM, Bagnara GP, Papa S. Role and function of matrix metalloproteinases in the differentiation and biological characterization of mesenchymal stem cells. Stem Cells. [Review]. 2006 Apr;24(3):475-81.

238. Moon JJ, Saik JE, Poché RA, Leslie-Barbick JE, Lee S-H, Smith AA, et al. Biomimetic hydrogels with pro-angiogenic properties. Biomaterials. 2010 Jun 01;31(14):3840-7.

239. Ruijter JM, Ramakers C, Hoogaars WMH, Karlen Y, Bakker O, van den Hoff MJB, et al. Amplification efficiency: linking baseline and bias in the analysis of quantitative PCR data. Nucleic acids research. [Evaluation Study]. 2009 May;37(6):e45.

240. Vandesompele J, De Preter K, Pattyn F, Poppe B, Van Roy N, De Paepe A, et al. Accurate normalization of real-time quantitative RT-PCR data by geometric averaging of multiple internal control genes. Genome biology. 2002 Jul 18;3(7):RESEARCH0034.

241. Schweitzer R, Chyung JH, Murtaugh LC, Brent AE, Rosen V, Olson EN, et al. Analysis of the tendon cell fate using Scleraxis, a specific marker for tendons and ligaments. Development. 2001 Oct 01;128(19):3855-66.

242. Walker JL, Zhai N, Zhang L, Bleaken BM, Wolff I, Gerhart J, et al. Unique precursors for the mesenchymal cells involved in injury response and fibrosis. Proc Natl Acad Sci. 2010 Aug 03;107(31):13730-5.

243. Box GEP, Cox DRT-. An Analysis of Transformations. Journal of the Royal Statistical Society Series B. 1964 Feb 01;26(2):211-52.

244. Raeber GP, Lutolf MP, Hubbell JA. Part II: Fibroblasts preferentially migrate in the direction of principal strain. Biomechanics and modeling in mechanobiology. 2008 Jul 01;7(3):215-25.

245. Scott A, Danielson P, Abraham T, Fong G, Sampaio AV, Underhill TM. Mechanical force modulates scleraxis expression in bioartificial tendons. Journal of musculoskeletal & neuronal interactions. 2011 Jul;11(2):124-32.

246. Hecker L, Jagirdar R, Jin T, Thannickal VJ. Reversible differentiation of myofibroblasts by MyoD. Experimental Cell Research. 2011 Aug 01;317(13):1914-21.

247. Walker GA, Guerrero IA, Leinwand LA. Myofibroblasts: molecular crossdressers. Current topics in developmental biology. [Review]. 2001;51:91-107.

248. Gabbiani G. The myofibroblast in wound healing and fibrocontractive diseases. The Journal of pathology. 2003;200(4):500-3.

249. Szczodry M, Zhang J, Lim C, Davitt HL, Yeager T, Fu FH, et al. Treadmill running exercise results in the presence of numerous myofibroblasts in mouse patellar tendons. J Orthop Res. 2009 Oct 01;27(10):1373-8.

250. Zhang J, Wang JH-C. Platelet-Rich Plasma Releasate Promotes Differentiation of Tendon Stem Cells Into Active Tenocytes. The American Journal of Sports Medicine. 2010 Aug 27.

251. Järvinen M, Józsa L, Kannus P, Järvinen TL, Kvist M, Leadbetter W. Histopathological findings in chronic tendon disorders. Scandinavian journal of medicine & science in sports. 1997 May;7(2):86-95.

252. Heo S-J, Nerurkar NL, Baker BM, Shin J-W, Elliott DM, Mauck RL. Fiber Stretch and Reorientation Modulates Mesenchymal Stem Cell Morphology and Fibrous Gene Expression on Oriented Nanofibrous Microenvironments. Annals of Biomedical Engineering. 2011 Jul 29.

253. Hankemeier S, Keus M, Zeichen J, Jagodzinski M, Barkhausen T, Bosch U, et al. Modulation of proliferation and differentiation of human bone marrow stromal cells by

fibroblast growth factor 2: potential implications for tissue engineering of tendons and ligaments. Tissue engineering. 2005 Feb 01;11(1-2):41-9.

254. Fan H, Liu H, Wong EJW, Toh SL, Goh JCH. In vivo study of anterior cruciate ligament regeneration using mesenchymal stem cells and silk scaffold. Biomaterials. 2008 Aug 01;29(23):3324-37.

255. Chiquet-Ehrismann R, Tannheimer M, Koch M, Brunner A, Spring J, Martin D, et al. Tenascin-C expression by fibroblasts is elevated in stressed collagen gels. The Journal of cell biology. 1994 Dec;127(6 Pt 2):2093-101.

256. Maier S, Lutz R, Gelman L, Sarasa-Renedo A, Schenk S, Grashoff C, et al. Tenascin-C induction by cyclic strain requires integrin-linked kinase. Biochimica et biophysica acta. 2008 Jul 01;1783(6):1150-62.

257. Palmer GD, Chao Ph PH, Raia F, Mauck RL, Valhmu WB, Hung CT. Time-dependent aggrecan gene expression of articular chondrocytes in response to hyperosmotic loading. Osteoarthritis and Cartilage. 2001 Nov;9(8):761-70.

258. Chiquet M, Sarasa-Renedo A, Tunç-Civelek V. Induction of tenascin-C by cyclic tensile strain versus growth factors: distinct contributions by Rho/ROCK and MAPK signaling pathways. Biochimica et biophysica acta. 2004 Sep 17;1693(3):193-204.

259. Paxton JZ, Hagerty P, Andrick JJ, Baar K. Optimizing an intermittent stretch paradigm using ERK1/2 phosphorylation results in increased collagen synthesis in engineered ligaments. Tissue Engineering Part A. 2011 Sep 08.

260. Rubin J, Murphy TC, Fan X, Goldschmidt M, Taylor WR. Activation of extracellular signal-regulated kinase is involved in mechanical strain inhibition of RANKL expression in bone stromal cells. Journal of bone and mineral research. 2002 Aug;17(8):1452-60.

261. Papakrivopoulou J, Lindahl GE, Bishop JE, Laurent GJ. Differential roles of extracellular signal-regulated kinase 1/2 and p38MAPK in mechanical load-induced procollagen alpha1(I) gene expression in cardiac fibroblasts. Cardiovascular research. 2004 Apr 01;61(4):736-44.

262. Sumanasinghe RD, Bernacki SH, Loboa EG. Osteogenic differentiation of human mesenchymal stem cells in collagen matrices: effect of uniaxial cyclic tensile strain on bone morphogenetic protein (BMP-2) mRNA expression. Tissue engineering. 2006 Dec;12(12):3459-65.

263. You L, Cowin SC, Schaffler MB, Weinbaum S. A model for strain amplification in the actin cytoskeleton of osteocytes due to fluid drag on pericellular matrix. Journal of Biomechanics. 2001 Nov;34(11):1375-86.

264. Ehrlich PJ, Lanyon LE. Mechanical strain and bone cell function: a review. Osteoporosis international. [In Vitro]. 2002 Sep;13(9):688-700.

265. Quinn TM, Grodzinsky AJ, Buschmann MD, Kim YJ, Hunziker EB. Mechanical compression alters proteoglycan deposition and matrix deformation around individual cells in cartilage explants. Journal of Cell Science. 1998 Apr;111 (Pt 5):573-83.

266. Han Y, Cowin SC, Schaffler MB, Weinbaum S. Mechanotransduction and strain amplification in osteocyte cell processes. Proc Natl Acad Sci. 2004 Nov 23;101(47):16689-94.

267. Darling EM, Wilusz RE, Bolognesi MP, Zauscher S, Guilak F. Spatial mapping of the biomechanical properties of the pericellular matrix of articular cartilage measured in situ via atomic force microscopy. Biophysical journal. 2010 Jul 16;98(12):2848-56.

268. Bryant SJ, Anseth KS. Hydrogel properties influence ECM production by chondrocytes photoencapsulated in poly(ethylene glycol) hydrogels. Journal of Biomedical Materials Research Part A. 2002 Feb;59(1):63-72.

269. Alexopoulos LG, Haider MA, Vail TP, Guilak F. Alterations in the mechanical properties of the human chondrocyte pericellular matrix with osteoarthritis. Journal of Biomechanical Engineering. [Comparative Study]. 2003 Jul;125(3):323-33.

270. Cao L, Guilak F, Setton LA. Three-dimensional finite element modeling of pericellular matrix and cell mechanics in the nucleus pulposus of the intervertebral disk based on in situ morphology. Biomechanics and modeling in mechanobiology. 2011 Mar;10(1):1-10.

271. Chen JL, Yin Z, Shen WL, Chen X-K, Heng BC, Zou X-H, et al. Efficacy of hESC-MSCs in knitted silk-collagen scaffold for tendon tissue engineering and their roles. Biomaterials. 2010 Dec;31(36):9438-51.

272. Zhang L, Tran N, Chen H-Q, Kahn CJF, Marchal S, Groubatch F, et al. Time-related changes in expression of collagen types I and III and of tenascin-C in rat bone mesenchymal stem cells under co-culture with ligament fibroblasts or uniaxial stretching. Cell and tissue research. 2008 May;332(1):101-9.

273. Petrigliano FA, English CS, Barba D, Esmende S, Wu BM, McAllister DR. The effects of local bFGF release and uniaxial strain on cellular adaptation and gene expression in a 3D environment: implications for ligament tissue engineering. Tissue engineering. 2007 Nov 01;13(11):2721-31.

274. Canal T, Peppas NA. Correlation between mesh size and equilibrium degree of swelling of polymeric networks. Journal of Biomedical Materials Research Part A. 1989 Oct;23(10):1183-93.

275. Rydholm AE, Bowman CN, Anseth KS. Degradable thiol-acrylate photopolymers: polymerization and degradation behavior of an in situ forming biomaterial. Biomaterials. 2005 Aug 01;26(22):4495-506.